ABSTRACT

Measurement of Jets and Jet Quenching at RHIC[1]

Michael L. Miller
Yale University
May 2004

We provide here the first study of jets in p+p collisions at RHIC using topological jet reconstruction of charged particles. By analyzing angular correlations of large transverse momentum di-hadron pairs, we also provide the first ever direct observation of jets in heavy ion collisions. Jet fragmentation to charged hadrons is then studied in Au+Au collisions as a function of impact parameter. The small-angle correlations observed in p+p collisions and at all centralities of Au+Au collisions are characteristic of hard-scattering processes already observed in elementary collisions. A strong back-to-back correlation exists for p+p and peripheral Au+Au collisions. In contrast, the back-to-back correlations are reduced considerably in the most central Au+Au collisions, indicating substantial interaction as the hard-scattered partons or their fragmentation products traverse the medium. These data are consistent with perturbative calculations incorporating partonic energy loss in dense QCD matter. To describe the data, these calculations require an initial energy density of $\sim$20 GeV/fm^3, more than 100 times the density of cold nuclear matter. This is suggestive of the formation of a novel, deconfined state of quark-gluon matter.

[1]Relativistic Heavy Ion Collider

Measurement of Jets and Jet Quenching at RHIC

A Dissertation
Presented to the Faculty of the Graduate School
of
Yale University
in Candidacy for the Degree of
Doctor of Philosophy

By
Michael L. Miller

Dissertation Director: John Harris

May 2004

Acknowledgements

First and foremost, to my wife Amelie. The last five years have truly been a wild ride – 10 apartments in 4 states, 200,000 air miles, and one too many car trips across South Dakota. You pulled me through the lows of qualifying exams, and you were there to cheer (and humble me!) in my moments in the spotlight. I am forever indebted to you for your love, dedication, and support. To my family, who provide the stability and encouragement that make all I do possible, and for always reminding me that a good name is worth more than great riches. Special thanks to those who continue to shape my development: Gary Westfall, Scott Pratt, and Wolfgang Bauer for the science, the lunches, the golf, and the general acceptance as a peer; Steve Johnson, whose contributions as a friend, supervisor, and peer are too numerous to list; Toby Burnett, for giving me a job when I arrived penniless in Seattle, for teaching me real c++, and for your continued generosity over 5 years, without which I would never have finished school with a wife; John Harris, Dave Hardtke, and Thomas Ullrich for your perpetual guidance, and for providing the resources and opportunities to grow within the field; to all the members of the Yale group, especially Helen, Jon, Matt, and Manuel for the many lessons, the debates, and all of the fun times. Last but not least, I am forever grateful to my father. You are the foremost scholar I know. Your values, your passion for discovery, and the joy with which you practice and teach science will forever be my shining example.

Contents

List of Figures

Chapter 1

Introduction

Particle physics is driven by the quest to understand the universe's fundamental particles and interactions. History has led to the classification of four fundamental interactions: the strong, weak, electromagnetic, and gravitational forces. The quest to develop theories of increasing elegance, simplicity, and predictive power now drives the determined struggle to unify these four forces at some large energy scale not seen since the earliest times of the universe's existence. Through rapid evolution of new theoretical and experimental techniques, the Standard Model of particle physics emerged by the end of the 20^{th} century. We now understand each force to be mediated by an exchange particle, and the relative "strength" of the force to be determined by a characteristic "coupling." The coming of age of quantum field theories led to SM[1,2] tests of exquisite precision. The drive for unification led the community to ever increasing energies, and dogged determination yielded the successful unification of the electrodynamic and weak forces. The next step along the path to a fundamental theory is less certain. Perhaps the deep exploration of the TeV range to begin soon at CERN will throw the doors open on the SM. Perhaps there will be no surprises, and we are indeed on the verge of a "great desert", as some have predicted. Regardless, there is much work to be done.

During the development of the SM, there were many intuitive surprises along the way. Perhaps one of the greatest arose from the strong force. The structure of the ubiquitous protons and neutrons (or more generally hadrons) is understood in terms of elementary particles (*quarks*) that interact so strongly that they can only be directly observed in "color-neutral" groups of two and three (and perhaps now five[3]).

[1]Standard Model

[2]All acronyms are collected in Appendix F.

[3]There is substantial new evidence for observation of a "penta-quark" state [1].

To further complicate the matter, the exchange particles (*gluons*) interact strongly with each other. The essential situation is that we know the Lagrangian, but we are often incapable of using it to make calculations. For example, while it has been more than thirty years since the discovery of quarks, the dynamics of quark *confinement* is still not fundamentally understood. Indeed, one state-of-the art theory relies on a phenomenological model of breaking strings. However, the challenges associated with the strong interaction hint at the richness of the underlying theory. A thorough understanding of the strong force can only help in the evolution of particle physics.

Such unresolved puzzles have pushed the community to develop new paradigms for investigation and exploration of the strong interaction. We present here an analysis of the strong interaction that uses high-energy hadron collisions of various levels of complexity to study the very nature of quark confinement. We use well established SM phenomena to test for the creation of a deconfined medium of quarks and gluons in the extreme conditions immediately following the collision of two ultra relativistic Gold ions. The mere *observation* of a deconfined state, while the subject of intense experimental effort, is by no means the ultimate goal[4]. Instead, by studying the properties of bulk quark-gluon matter, one hopes to push understanding into new regimes, those previously intractable with the standard perturbative treatment. Indeed, significant fundamental advances may be possible. The topic is much broader than just the question of confinement. New and previously unobserved characteristics of the strong interaction may be manifested in dense quark-gluon media, with predictions ranging from the modifications of hadronic masses[2] to the observation of CP symmetry violation in the strong interaction[3].

In a central RHIC Au+Au collision at energy $\sqrt{s_{\rm NN}}$= 200 GeV we clearly create nuclear matter at extreme energy densities. At mid-rapidity, more than 1000 particles emerge from a volume with a characteristic radius of $\sim$5 fm. The goal is to probe this strongly interacting matter, so we do what comes naturally to particle physicists: we send "something" in to scatter off of this high-density matter. Unfortunately, we lack the $\sim$1 fm wavelength laser that would be so ideal for this task. We instead follow the suggestion of Bjorken and use hard-scattered partons, created in the earliest

[4]It is perhaps intuitive that at some high temperature even hadrons eventually melt.

stages of the very same collision, as our probe of the medium[5]. This requires both a thorough calibration of our probe and an understanding of the dynamics of our probe interacting with the medium. In Secs. 1.1 and 1.2 we perform a short review of the theoretical concepts required to calibrate our probe, and in Sec. 1.3 we introduce the theory of partonic scattering in dense QCD media. Sec. 1.4 briefly introduces the experimental strategy of this analysis, and Sec. 1.5 outlines the structure of this thesis.

1.1 Quantum Chromodynamics

The SM of particle physics consists of two basic components: the spontaneously broken $SU(2) \times U(1)$ electroweak theory, and the unbroken $SU(3)$ color gauge theory, known as QCD[6] – the theory of strong interactions. The richness of the strong interaction is perhaps best described by the two following phenomena, which are at first glance intuitively contradictory.

confinement The quark model describes the vast experimental spectrum of over 1000 hadrons. However, all experimental attempts to isolate a single free quark have failed, yielding experimental final states that are dominated by production of familiar mesons and baryons. Evidently, the interaction between quarks is *strong*.

asymptotic freedom However, the strong interactions at high-energies, which are investigated so precisely by accelerator experiments, are quite successfully described by a model (the parton model) in which quarks do not interact at all.

That a single theory can describe these two extreme scenarios in a unified treatment is one of the fundamental successes of QCD. The formulation of QCD grew from the introduction of the new quantum number of *color* and the simultaneous development of unitary, renormalizable quantum gauge theories. It was quickly realized that

[5]Hence the commonly used phrase "Jet Tomography."
[6]Quantum Chromodynamics

an energy-dependent coupling was needed to rectify the apparent conflict of long-range confinement with the short-range success of the parton model. The concept of asymptotic freedom, "which is satisfied almost uniquely by quantum chromodynamics, brilliantly filled these demands ."[4]

Over time, it has become clear that asymptotic freedom is a perturbative concept, and that confinement is not [4]. pQCD[7] describes a large set of high-energy, large momentum transfer processes with outstanding accuracy. In fact, comparison of Fermilab jet data and pQCD predictions at better than the 1% level is a sensitive test for physics beyond the SM [4] [5]. Ref. [4] states, "However, the very successes of a purely perturbative approach challenge us to bridge the gap between perturbative and non-perturbative aspects of the theory. Every experiment in strong interactions tests QCD from some fixed 'short' distance to its very longest distance scales, over which the value of the strong coupling may change radically." As pQCD has matured, significant efforts have developed to explore the transition between the perturbative and non-perturbative regimes. Both theoretically and experimentally, this has resulted in new methods of investigation, sometimes drastically different than the traditional paradigms of elementary particle physics.

The growth of Relativistic Heavy Ion physics represents such a change in philosophy. In 1975, T.D. Lee wrote, "In high-energy physics we have concentrated on experiments in which we distribute a higher and higher amount of energy into a region with smaller and smaller dimensions. In order to study the question of 'vacuum', we must turn to a different direction; we should investigate some 'bulk' phenomena by distributing high-energy over a relatively large volume." This means more than just abandoning the exquisitely controlled environment provided by e^+e^- and $p + \bar{p}$ collisions. Instead, an expanded horizon is provided by a global study of the strong interaction over e^+e^-, e+A, $p + \bar{p}$, p+A, and ultimately AA collisions. This has resulted in new dedicated experimental facilities such as RHIC as well as exploration of new regions in the rich theory of QCD including QCD coherence, QCD in nuclei, QCD collectivity, and color transparency, to name a few. Both experimentally and theoretically, these studies make extensive use of concepts from different realms of

[7]Perturbative Quantum Chromodynamics

physics, including thermodynamics, statistical mechanics, many-body physics, fluid dynamics, and perturbative field theory.

At this point in heavy ion theses, one often finds an introduction to the QGP[8] phase transition. Indeed, lattice QCD calculations do predict the onset of deconfinement beyond a critical temperature T_c [6]. However, the extraction of thermodynamic quantities (e.g., temperature[9], energy density, and chemical potential) from a heavy ion collision is complex and, to date, extremely model dependent. While statistical mechanical models are successful in describing the relative yields of a wide variety of particle species [8], most rely on the rather strong assumption that one creates *equilibrated* quark-gluon matter in RHIC collisions. Conclusive experimental proof of equilibration would be a fundamental discovery in the field. It is, however, a great challenge to prove that a $\sim$5 fm^3 volume of matter which exists for $\sim$10 fm/c is equilibrated.

This thesis is therefore structured to reflect the author's bias that strongly interacting matter can be meaningfully studied without total abandonment of the perturbative methods of QCD. Using large momentum transfer QCD processes in RHIC collisions as a probe, we can explore the physics of soft processes, but we begin from a well defined starting point.

1.2 Perturbative Quantum Chromodynamics

In this thesis we make extensive use of pQCD concepts. Ref. [4] gives a list of QCD review texts. Here we briefly review the concepts of renormalization, infrared and collinear safety, factorization, and evolution.

[8]Quark Gluon Plasma

[9]To share one highly regarded opinion, we quote Dokshitzer [7]: "I would refrain from using the word "temperature" in the discussion of the famous exponential fit to hadron abundances, $N \sim e^{-m/T}$, or $e^{-m_\perp/T}$, if that matters ... at least in this clear case [e^+e^- $\rightarrow$hadrons] the Hagedorn "temperature" is a universal property of the *vacuum*, of the parton$\rightarrow$hadron transition, rather than a thermal characteristic of a particle ensemble."

1.2.1 Renormalization and the Running Coupling

The "strength" of the strong interaction is defined by the QCD coupling constant α_s. The scale dependence of α_s stems from renormalization in pQCD. Fig. 1.1a shows a lowest order Feynman diagram for the annihilation process $q + \overline{q} \rightarrow q + \overline{q}$. Each

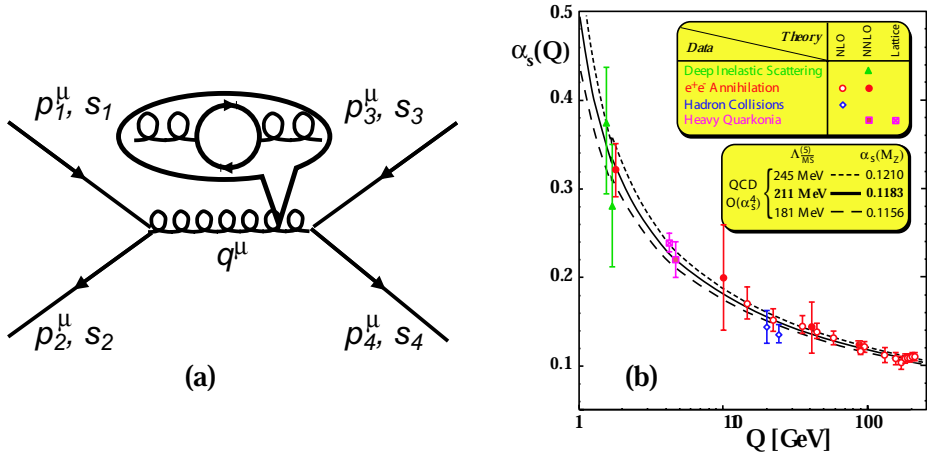

Figure 1.1: (a) Feynman diagram for $q + \overline{q} \rightarrow q + \overline{q}$ annihilation. Time flows from left to right. Momentum conservation implies $(p_1^\mu + p_2^\mu)^2 = q^2 = -Q^2 = (p_3^\mu + p_4^\mu)^2$. Each vertex contributes a factor of $\sqrt{\alpha_s}$ to the matrix element. (b) $\alpha_s(Q)$ vs. Q [9]

vertex contributes a factor of $\sqrt{\alpha_s}$ to the hard perturbative matrix element. When probed at smaller distance scales, however, one can resolve, e.g., a brief fluctuation of a gluon into a fermion-antifermion pair, as illustrated by the "balloon" in Fig. 1.1a. Such higher order diagrams give non-negligible contributions to the calculation. In fact, the insertion of just one loop in the propagator ($g \rightarrow q + \overline{q} \rightarrow g$) creates a divergence in the calculation. Sensitivity to such a small scale phenomenon can essentially be removed by redefining the scale of the problem ("zooming out"). A renormalization scheme systematically introduces an arbitrary cutoff[10] to render the calculation finite, resulting in the introduction of a renormalization scale μ. We of course require $\mu \frac{d\sigma(p,\mu)}{d\mu} = 0$, which states that a measurable quantity $\sigma(p, \mu)$ not

[10]The actual procedure is far more delicate than we present here. Indeed, renormalization via a "cutoff" is likened to "Savage butchery" by theorist J. Osborne. Renormalization schemes do, however, introduce a new scale, so the arguments presented still hold.

depend on μ. This leads to the RGE[11], a differential equation that defines the scale dependence of quantity $\sigma(p, \mu)$. The contribution of divergent portions of a diagram are essentially incorporated into the vertex factor α_s. To lowest order, α_s is given by

$$\alpha_s(\mu^2) = \frac{\alpha_s(\mu_0^2)}{1 + \beta_1/4\pi\alpha_s(\mu_0^2)\log(\mu^2/\mu_0^2)},\ \beta_1 = \frac{11N_c - 2n_f}{3} \tag{1.1}$$

where N_c is the number of colors, n_f is the number of quark flavors, and $\alpha_s(\mu_0)$ is a boundary condition of the differential equation. Because α_s appears to depend on both $\alpha_s(\mu_0^2)$ and μ_0^2, this is often rewritten as

$$\alpha_s(\mu^2) = \frac{4\pi}{\beta_1 \log(\mu^2/\Lambda^2)},\ \Lambda = \mu_0 e^{-2\pi/(\beta_1 \alpha_s(\mu_0^2))} \tag{1.2}$$

where Λ is the famous "scale constant" in QCD. Fig. 1.1b shows the running of α_s with scale. The sharp rise at low-Q and the asymptotic trend to zero at large Q clearly satisfy both the strong coupling at small momentum scales (confinement region) and the weak coupling at large momentum scales (asymptotically free region).

1.2.2 Parton Distribution Functions, Fragmentation Functions, QCD Factorization, and QCD Evolution

To date, pQCD cannot predict from first principles the momentum distribution of quarks and gluons contained in a hadron. However, the predictive power of pQCD is that it doesn't have to. *Given* these distributions at one scale, pQCD can predict with high accuracy the nature of these distributions at vastly different scales. We describe this process below.

Consider a massless relativistic hadron of momentum $p^\mu_{hadron} = (p_z, 0, 0, p_z)$ that is composed of valence quarks, gluons, and sea quark-antiquark pairs, all of which we refer to as "partons". A given parton has a fraction of the hadron momentum $x_{Bjorken} = x \equiv \frac{p_{parton}}{p_{hadron}}$, where $0 < x < 1$. We define the PDF[12] $f_{i/h}(x_i)dx$ to be the probability to find a parton of momentum fraction x_i in hadron h. Thus, the PDF encapsulates the non-perturbative physics of confinement. Using DIS[13] of leptons

[11] Renormalization Group Equations
[12] Parton Distribution Function
[13] Deep Inelastic Scattering

hard scattering on hadrons, these distributions can be *measured* as a function of x and momentum transfer q^2 in experiments where both x and q^2 are kinematically constrained. Not surprisingly, there are subtleties in defining the PDFs. These complications arise primarily in establishing the boundary between the non-perturbative PDF matrix elements and the perturbatively calculable hard-scattering matrix elements. For instance, at small distance scales one can resolve vacuum fluctuations (e.g., a short lived quark-antiquark pair) in both the hard-scattering propagator and within the hadron itself. *Factorization* is a systematic way of separating the region between the PDF and the hard-scattering, thus establishing a clear boundary between the perturbative and non-perturbative regions. One introduces a second arbitrary scale (μ_F) that has the following approximate meaning:

- A parton off-shell by *less than* μ_F^2 is incorporated into the non-perturbative matrix element $f_{i/h}$.
- A parton off shell by *more than* μ_F^2 is incorporated into the hard-scattering matrix element of the calculation.

A remarkable consequence of factorization is that measuring PDFs for one scale μ allows their prediction for any other scale μ', as long as both μ and μ' are large enough that both $\alpha_s(\mu)$ and $\alpha_s(\mu')$ are small. This result, the *evolution* of structure functions, is a tremendous increase in the predictive power of pQCD. Thus, measuring $f_{i/h}(x, Q_0^2)$ allows the evolution to any Q^2. This process allows one to indirectly test the accuracy of QCD in the perturbative regime. This was one of *the* major focuses of the QCD program at HERA[14], where QCD evolution predictions were verified to superb precision.

The PDFs are best constrained by global theoretical analyses to data using scattering of electron, muon, neutrino, photon, and hadron beams on hadron targets over a wide kinematic range. Fig. 1.2 shows proton PDFs from the CTEQ[15] collaboration [10] at scales of $Q = 2$ and $Q = 100$ GeV. Note that the proton is dominated by gluon contributions for $x <\sim 10^{-1}$. In p+p collisions one generally is unable to

[14]Hadron Electron Ring Accelerator
[15]Coordinated Theoretical-Experimental Project on QCD

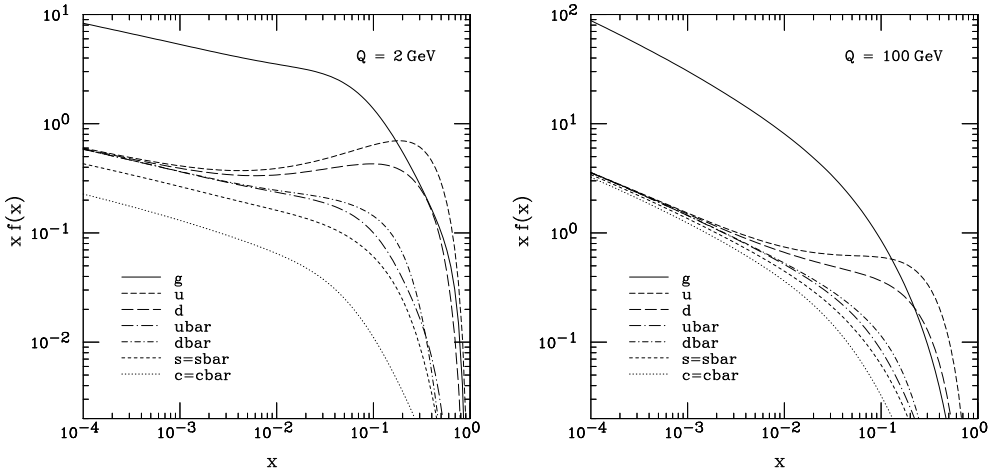

Figure 1.2: CTEQ6M parton distribution functions evaluated at (a) Q=2 GeV and (b) 100 GeV [10]. Note that the vertical axis scale in (b) is one decade higher.

measure the x values of the two hard scattered partons (this is in fact dependent on the reaction). However, a useful order of magnitude estimate is $x \simeq x_T = \frac{2p_\perp}{\sqrt{s}}$ (see App. A for a derivation). For rapidity y =0 at RHIC, we find $10^{-2} < x_T < 10^{-1}$ for $1 < p_\perp < 10$ GeV/c processes. From Fig. 1.2a we thus expect gluon dominance in the PDF. However, the region $p_\perp > 10$ GeV/c is sensitive to the interplay between gluon and valence quark distributions.

There is an additional nuclear modification to the PDFs called *shadowing*, which refers to the observation that proton and neutron PDFs are different when measured in a free nucleon and a nucleon bound in a nucleus. The shadowing effect is largest at small-x and depends on the mass number A of the nucleus, the radial location of the nucleon within the nucleus, and the scale (Q^2). Shadowing is measured at energy scales below RHIC [11] and is believed to be an important component in small-x RHIC phenomena. However, the magnitude of the shadowing effect is highly constrained by varying the collision energy, $\sqrt{s_{\rm NN}}$, and by using both d+Au and Au+Au collisions.

We have introduced the non-perturbative nature of quark confinement with a discussion of PDFs. A similar story exists not only in the distribution of partons in hadrons, but also in the inverted process of parton fragmentation – the dynamic process of a free parton showering into a focused cluster of final state energetic hadrons

(a jet). Here one essentially evaluates the distribution of hadrons *within* a parton. The FF[16] $D_p^h(z)$ has the interpretation of a probability density that some final state parton p hadronizes (fragments) into a mean number $D_p^h(z)dz$ of hadrons h per dz, where z is the fractional momentum that h receives from the parton ($z = \frac{p_{hadron}}{p_{parton}},\ 0 < z < 1$). FFs are essentially the reverse of PDFs, and the rules of factorization and evolution apply to both regimes. Fig. 1.3a shows measured fragmentation functions at the Z^0 pole from LEP[17] data. Fig. 1.3b shows the scale dependence of light quark FFs at

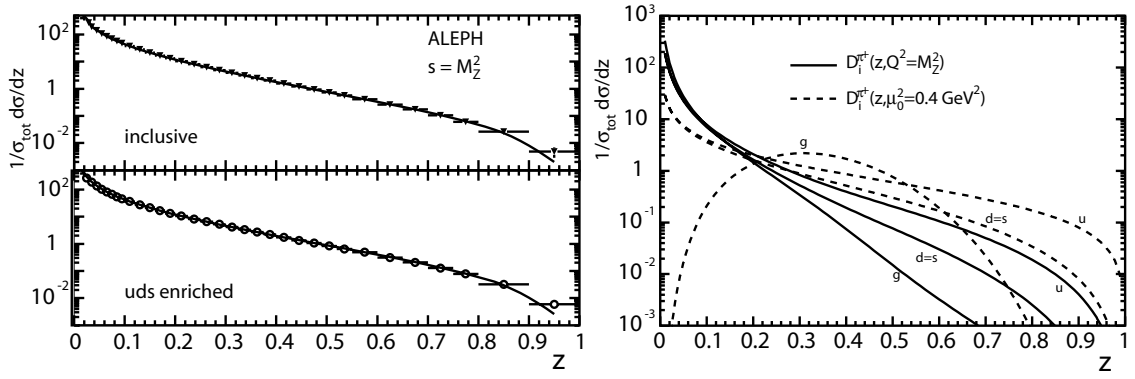

Figure 1.3: (a) ALEPH inclusive fragmentation functions from charged hadrons, measured at the Z^0 pole, and the corresponding fit results from Kretzer. (b) Input fragmentation function for light quarks and gluons (dashed lines) evolved to $Q^2 = M_z^2$. Figures taken from Ref. [12].

scales of $Q^2 = 0.4$ GeV^2 and $Q^2 = M_z^2$. Note that the FF for gluons is significantly different than FFs of quarks. We will revisit this difference later in the analysis.

We now have the essential components to write the factorizable pQCD cross section for various processes. For di-jet production in the hadron-hadron collision $A + B \rightarrow jet_1 + jet_2 + X$ we have

$$\frac{d\sigma}{dy} = \sum_{a,b} \int_0^1 dx_A \int_0^1 dx_B \ f_{a/A}(x_A, \mu_F)\ f_{b/B}(x_B, \mu_F) \frac{d\hat{\sigma}_{ab\rightarrow cd}(\mu, \mu_F)}{dy} \tag{1.3}$$

The meaning of this formula is now surprisingly intuitive: $f_{a/A}(x_A, \mu_F)\ dx_A$ gives the probability to find a parton a in hadron A; $f_{b/B}(x_B, \mu_F)dx_B$ gives the probability to

[16]Fragmentation Function
[17]Large Electron Positron Collider

find a parton b in hadron B; $d\hat{\sigma}_{ab\to cd}(\mu,\mu_F)/dy$ (which is calculated perturbatively) gives the cross section for these partons to produce the outgoing partons c and d, which fragment into jets of hadrons. This prediction is directly comparable to an experimental measurement *if* both jets are fully reconstructed. Suppose that one is interested in single particle production. The cross section for $A+B\to C+X$, where C is, e.g., a π^0 meson, includes an extra integration over the fragmentation function $D_{C/c}(z)$:

$$\frac{d\sigma}{dy}=\sum_{a,b}\int_0^1 dx_A\int_0^1 dx_B\int_0^1 dz_c\, f_{a/A}(x_A,\mu_F)\, f_{b/B}(x_B,\mu_F)\,\frac{D_{C/c}(z_c,\mu_F)}{z_c}\,\frac{d\hat{\sigma}_{ab\to cd}(\mu,\mu_F)}{dy}. \tag{1.4}$$

Fig 1.4 shows the relative contribution of qq, qg, and gg processes to the total di-jet cross section in p+p collisions at $\sqrt{s_{NN}}=200$ GeV from a leading order QCD calculation. The final curves result from the interplay of the PDFs and the hard-

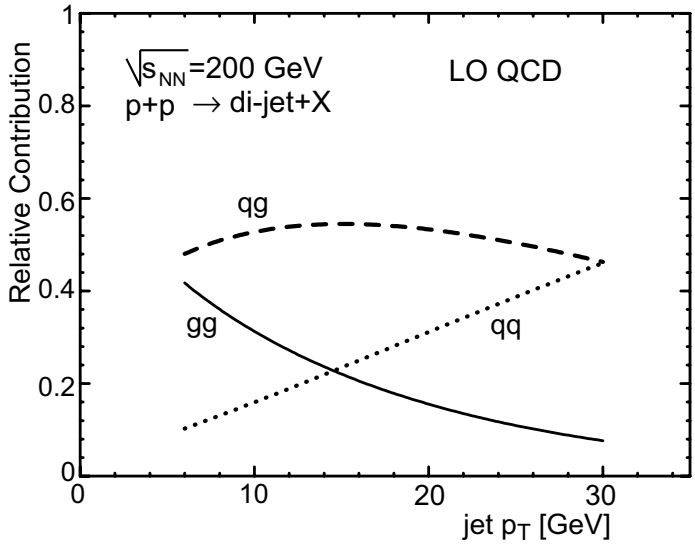

Figure 1.4: Relative contribution of qq, qg, and gg to di-jet cross section from LO pQCD calculation (Werner Vogelsang, private communications).

scattering scattering matrix element. For jet $p_\perp < 5$ GeV/c (low-x processes) we find gluon dominance. For $p_\perp > 30$ GeV/c, high-x scatterings of valence quarks dominate. The region $5 < p_\perp < 30$ GeV/c is dominated by qg processes.

For a *nucleus* induced collision, Eqs. 1.3 and 1.4 are modified by an additional factor. In the extreme factorization limit, the yield of hard processes in a Au+Au collision should scale as the number of nucleon-nucleon interactions (N_{coll}) in a given Au+Au interaction[19]. N_{coll} is a quantity that cannot be measured and must thus be calculated. App. E describes the specifics of the model calculations and its limits. Here we simply note that N_{coll} varies from 2 in the limit of an ultra-peripheral Au+Au collision to ∼1200 in a central Au+Au collision and follows the approximate scaling $N_{coll} \approx A^{4/3}$. Clearly, N_{coll} scaling cannot hold exactly, as nuclear shadowing of the PDFs has already been observed. Realistically, it is the *deviation from* N_{coll} scaling of hard cross sections that is used to probe nuclear modifications to both the PDFs and the FFs.

1.2.3 Collinear and Infrared Safety

The final step in our lightning review of QCD involves the concept of collinear and infrared safety. A CIS[20] quantity is one that can be perturbatively calculated without obtaining infinity. Consider the perturbative expansion of some observable σ given by:

$$\sigma\left(\frac{p_i \cdot p_j}{\mu^2}, \frac{m_i^2}{\mu^2}, g(\mu)\right) = \sum_{n=0}^{\infty} a_n \left(\frac{p_i \cdot p_j}{\mu^2}, \frac{m_i^2}{\mu^2}\right) \alpha_s^n(\mu) \tag{1.5}$$

where p_i denote external momenta and m_i the internal quark masses. It is quite common that the expansion coefficients a_n are large, *regardless of the value of* $\alpha_s(\mu)$. That is, they are not even defined (IR[21] divergent) in a renormalized theory. In fact, due to the vanishing gluon mass, nearly *all* pQCD cross sections are IR divergent. Hope, however, stemmed from the identification and calculation of a significant class of quantities which are collinear and infrared safe. The essence of CIS quantities is

[19]This essentially assumes that the yield from hard parton-parton interactions scales with the number of possible parton-parton interactions.

[20]Collinear and Infrared Safe

[21]Infrared

that they do not depend on long-distance behavior. For a CIS quantity the requirement

$$\mu\frac{d\sigma(p,\mu)}{d\mu} = 0 \quad \text{has the solution} \quad \sigma\left(\frac{Q^2}{\mu^2}, 0, g(\mu)\right) = \sigma(1, 0, g(Q)) \tag{1.6}$$

in which all of the momentum dependence has been absorbed into the couplings $g(Q)$. When Q is large, the coupling decreases, and the perturbative result becomes increasingly better.

To understand what quantities are CIS safe and why, one can consider a perturbative calculation in which both quarks and gluons are massless. Sensitivity to long-distance effects will then be manifested as IR divergences in the calculation. It turns out that these divergences are all related to soft or collinear momentum configurations [4] [13].

- A massless on-shell particle of momentum p^μ can emit a massless particle of momentum $q^\mu = 0$ and remain on-shell. Integration over momenta q^μ near $q^\mu = 0$ produces *soft divergences* in cross sections.

- A massless on-shell particle of momentum p^μ can emit a particle of momentum $q^\mu = zp^\mu,\ 0 < z < 1$, and remain on-shell. Integration over momenta q^μ near to $q^\mu = zp^\mu$ produces *collinear divergences* in cross sections.

In the perturbative calculation of, e.g., the total cross section for e^+e^- annihilation, individual terms are actually infinite due to soft and collinear divergences, but, for reasons of unitarity, they are cancelled by balancing infinities at different orders. The identification of IR safe quantities is a critical part of QCD. In Sec. 4 we spend a large amount of effort defining jet clustering algorithms that are CIS. Suppose one measures a jet yield via a non-CIS algorithm. The corresponding pQCD calculation *must* use the same jet definition scheme. A non-CIS algorithm will yield a prediction that is not merely slightly off, but infinite. Specification of CIS safe jet algorithms is not a luxury, it is a requirement.

1.3 Parton Propagation in Dense QCD Media

An active area of QCD is the study of partons traversing dense QCD matter. In QED[22] the acceleration of a charged particle is accompanied by the emission of a bremsstrahlung photon, taking an energy ΔE away from the charged particle. The analog exists in QCD, where a quark or gluon scattering off a *color* charge will emit a bremsstrahlung gluon. The magnitude of the energy loss dE depends on the distance of propagation dx and can be large ($O(dE/dx) \sim 1 - 10$ GeV/fm). Although this field can be traced back over twenty years, it has only recently come into its own with the advent of RHIC, the first facility with sufficient conditions (high-energy heavy ion beams) to provide abundant parton-parton hard-scatterings *within* heavy ion collisions.

In 1982 Bjorken first proposed that a final state parton would suffer *collisional* energy loss via elastic scatterings in a deconfined quark-gluon plasma [14]. Depending on the spatial location of the parton-parton scattering within the medium, this energy loss was predicted to result in a large asymmetry in the transverse momenta of di-jets. In the extreme scenario of di-jet production on the surface of the medium, with one parton directed into the medium and the other parton directed outward into the vacuum, Bjorken predicted a near mono-jet signal, where the "vacuum" jet would be reconstructed, but the away-side jet would be essentially "quenched" (or extinguished, in Bjorken's words) via large energy loss while traversing the medium.

Revisions in Bjorken's initial calculation[23] later showed that collisional energy loss would result in relatively small values of $dE/dx < 0.5$ GeV/c. It was quickly realized that the multiple scattering of a fast parton in a QCD medium would induce gluon radiation, resulting in *radiative* energy loss that could be much larger than Bjorken's collisional energy loss, although precise calculations were in fact highly complicated. Additionally, a fast parton undergoing multiple scattering acquires additional momentum transverse to its original direction of travel and leads to what is called $p_\perp$ broadening. These two effects have led to a great effort to understand $p_\perp$ broadening and the non-abelian nature of radiative energy loss, as well as their effects on inclusive

[22] Quantum Electrodynamics
[23] an unpublished *erratum*

single particle and jet yields, di-hadron and di-jet yields, and modifications to parton fragmentation. Many advances have been made in recent years. Instead of following the historical development further, we will attempt to briefly summarize the present state of understanding[24].

Theoretically, the field has made major advances in establishing the importance of the following phenomena:

- Quantum interference effects in gluon formation and emission
- Finite size and expansion of the medium
- $p_\perp$ broadening: the accumulation of additional parton $p_\perp$ from multiple soft interactions in medium, both pre and post hard-scattering.
- Gluon re-scattering and feedback mechanisms (i.e., *absorption* of a radiated gluon by a fast parton)
- Induced gluon radiation in "cold nuclear" matter, i.e., $e + A \rightarrow jet + X$.

The BDMPS[25][17][15] results have concentrated primarily on the calculation of the energy and angular spectrum of radiated gluons. The importance of quantum interference effects have been shown to be not merely important, but critical. This goes under the name of the LPM[26] effect, which is briefly described in App. C. The BDMPS results show that calculation of dE/dx is sensitive to non-perturbative effects, thus yielding a method of exploring the non-perturbative regime. However, calculation of the induced gluon spectrum and the corresponding "quenching factor" that relates in-medium spectra to vacuum spectra are formally CIS quantities[18]. The finite size of the medium introduces a dependence of the energy loss on the length of the medium L[7]. The medium itself is indeed not static, but expanding rapidly with time ($v_{medium}^{expansion} \sim c/2$), further increasing the complication. Vitev *et al.* have made thorough calculations of initial and final state $p_\perp$ broadening effects, constrained to

[24]See Refs. [15] and [16] (and references therein) for a comprehensive review of the state of theoretical predictions and experimental results, respectively.

[25]Baier, Dokshitzer, Mueller, Peigné, and Schiff

[26]Landau, Pomeranchuk, and Migdal

p+p and d+Au from RHIC[19]. Wang *et al.* have calculated the contributions from feedback mechanisms and made comparisons to the much smaller values of dE/dx observed in cold nuclear matter at HERA[20]. Hirano, Nara, Gulassy, and Vitev have coupled partonic energy loss to hydrodynamic calculations to study the interplay of the collective size and dynamics of the source with the induced gluon radiation[21] [22].

Contrary to the situation a decade ago, the theoretical predictions are converging and a rather simple picture is emerging. The angular spectrum of radiated gluons is nearly collinear with the direction of the fast parton [27]. The parton ultimately will be associated with a jet of hadronic particles in the lab. The jet will contain contributions from both the fragmentation products of the parton and the fragmentation products of the bremsstrahlung gluons. These jets will be characterized by a higher than average multiplicity and a shift to softer fragmentation (lower $\langle z \rangle$). However, the total energy of the jet is expected to remain approximately unchanged due to the collinear nature of the gluon emission spectrum. Medium induced gluon radiation is thus characterized by an effective "softening" of the fragmentation function. The ultimate goal is to measure this modification of the FF and thus "extract" the magnitude of the energy loss. This is extremely challenging, though, given the relatively small values of jet $p_\perp$ ($p_\perp <\sim$ 15 GeV/c) accessible with current RHIC statistics and the large background $dN/d\eta \sim 1000$ [28]. However, the modification of the FF can be probed by searching for modifications in the high-$p_\perp$ inclusive particle spectra, and by using jet-like correlations of high-$p_\perp$ particles to probe changes in the jet structure.

Other phenomena also influence the production of high-$p_\perp$ hadrons, and a mix of theoretical analyses and experimental controls allow one to separate the influence of several of these effects. Perhaps the strongest experimental controls come from changing the collision system and varying the impact parameter of the collisions. Both offer control over the size and energy density of the medium. Formally, we consider the following time-ordered sequence of a hadron-hadron collision: hard parton-parton

[27] $\Theta \sim \left(\frac{\omega_0}{\omega}\right)^{3/4}$, $\omega_0 \sim 0.5$ GeV for a hot medium [7]

[28] The long-term outlook is optimistic. The partial commissioning of the STAR calorimeter and trigger systems have already extended the jet $p_\perp$ range to ∼40 GeV/c in the latest p+p data.

scatterings with $q^2 \gg 1$ fm/c are localized in space and time, and it is the multiple parton scatterings before and/or after the hard collision that are sensitive to the properties of nuclear matter. By studying high-$p_\perp$ particle production at increasing levels of complexity (p+p, d+Au, Au+Au) one can study QCD dynamics in vacuum, cold nuclear matter, and hot nuclear matter. The connection is perhaps best illustrated by Vitev when he writes [19], "So far the first two integral moments $\int z^n \; dz \; \rho(z)$ of the matter density in the interaction region can be deduced from experimental measurements since they are related to the broadening[29] and energy loss of a fast parton traversing nuclear matter." In the midrapidity region Vitev relates the first two moments to the broadening and energy loss, respectively, by:

$$\langle \Delta \mathbf{k}_T^2 \rangle \approx 2\xi \int dz \, \frac{\mu^2}{\lambda_{q,g}} = 2\xi \int dz \, \frac{3C_R \pi \alpha_s^2}{2} \rho^g(z) = \begin{cases} 2\xi \, \frac{3C_R \pi \alpha_s^2}{2} \, \rho^g \langle L \rangle \, , & \text{static} \\ 2\xi \, \frac{3C_R \pi \alpha_s^2}{2} \, \frac{1}{A_\perp} \frac{dN^g}{dy} \, \ln \frac{\langle L \rangle}{\tau_0} \, , & 1+1D \end{cases} \tag{1.7}$$

and

$$\begin{aligned} \langle \Delta E \rangle \approx \int dz \, \frac{C_R \alpha_s}{2} \frac{\mu^2}{\lambda_g} \, z \, \ln \frac{2E}{\mu^2 \langle L \rangle} \quad &= \quad \int dz \, \frac{9C_R \pi \alpha_s^3}{4} \rho^g(z) \, \ln \frac{2E}{\mu^2 \langle L \rangle} \\ &= \begin{cases} \frac{9C_R \pi \alpha_s^3}{8} \, \rho^g \langle L \rangle^2 \, \ln \frac{2E}{\mu^2 \langle L \rangle} \, , & \text{static} \\ \frac{9C_R \pi \alpha_s^3}{4} \, \frac{1}{A_\perp} \frac{dN^g}{dy} \langle L \rangle \, \ln \frac{2E}{\mu^2 \langle L \rangle} \, , & 1+1D \end{cases} \end{aligned} \tag{1.8}$$

Here $\xi \simeq \mathcal{O}(1)$, λ is the parton mean free path, C_R is the color charge of the parton (see App. B), $\mu^2 = \langle p_\perp^2 \rangle$ acquired per individual scattering, and ρ^g is the effective gluon density. In the 1+1D expansion scenario (expanding along the beam direction, often referred to as the Bjorken scenario), $\langle L \rangle$ is the mean distance of propagation, $A_\perp$ is the impact parameter-dependent transverse area of the interaction region, τ_0 is an initial equilibration time and dN^g/dy is the effective gluon rapidity density.

While these equations appear complicated, the essential physics contained in $\langle \Delta k_T^2 \rangle$ and $\langle \Delta E \rangle$ is rather straight-forward. Both quantities depend on:

[29] $p_\perp$ broadening effects are manifested in acoplanarity of di-jets and shifts in single particle $p_\perp$ distributions, as we shall discuss in Sec. 7

- the color charge C_R of the projectile and the gluon density of the medium $\rho^g(z)$
- the finite size of the medium which, when convoluted with the LPM suppression, transforms the $\sqrt{E}$ dependence of the infinite length LPM prediction to a logarithmic dependence and introduces a power-law dependence on the length L of the medium
- the expansion dynamics of the system (static vs. 1+1D)
- the quantities λ and μ, which are highly sensitive to non-perturbative physics

From this (non-exhaustive) list we draw the following conclusion. The theoretical and experimental study of propagation of high- energy partons through dense QCD matter pushes QCD into new directions, exploring the sensitive interplay between the perturbative and non-perturbative regimes. As well, the potential measurement of partonic energy loss is highly sensitive to the nature of the medium being traversed, namely its size, density, and collective motion.

1.4 Jet Tomography at RHIC

.

In this analysis we use hard parton-parton scattering, a physical process that is well described by pQCD, to search for the signatures of partonic energy loss. We will study jet production as a function of increasing collision complexity, beginning in p+p collision, progressing to peripheral Au+Au collisions, and finishing in extremely central Au+Au collisions. The early RHIC data *are* suggestive of the creation of strongly interacting matter, and this is perhaps best illustrated in the phenomena of elliptic flow and high-$p_\perp$ suppression, which are introduced below.

First, elliptic flow is related to the transition of initial state asymmetry in *position-space* into final state anisotropy in *momentum-space*. Fig 1.5 shows a "beam's-eye" view of a non-central Au+Au collision. The finite impact parameter yields a football shaped overlap region in the transverse plane. Multiple interactions within the matter

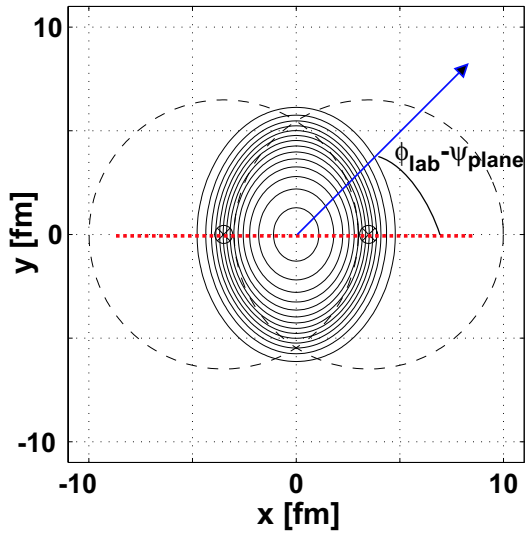

Figure 1.5: The asymmetric overlap region in a non-central heavy ion collision. The projection of the reaction plane onto the $x-y$ plane is represented by the red line at $y=0$. The blue arrow indicates a sample trajectory of a final state hadron.

can develop pressure gradients which are different in the in- and out-of plane directions. If the these interactions are of sufficient strength, this mechanism can generate an anisotropy in the final-state momentum distribution with respect to the reaction plane[30]. The size of the final state momentum anisotropy (which can be measured) should reflect the amount of initial-state spatial anisotropy, which is quantified by the eccentricity ϵ given by

$$\epsilon = \frac{\langle y^2 - x^2 \rangle}{\langle y^2 + x^2 \rangle}. \tag{1.9}$$

ϵ cannot be measured and must be deduced from Glauber calculations (see App. E); it is zero in a perfectly central collision ($b = 0$ fm) and increases with b, with the largest values in the most peripheral collisions.

Fig 1.6a shows the azimuthal distribution of particles with respect to the reaction plane, evaluated on a per-event basis. A clear harmonic structure is observed, with the largest effect in the most peripheral collisions (largest ϵ). The spectra are Fourier

[30]Reaction plane: the plane drawn through the centers of the two colliding nuclei and along the beam direction.

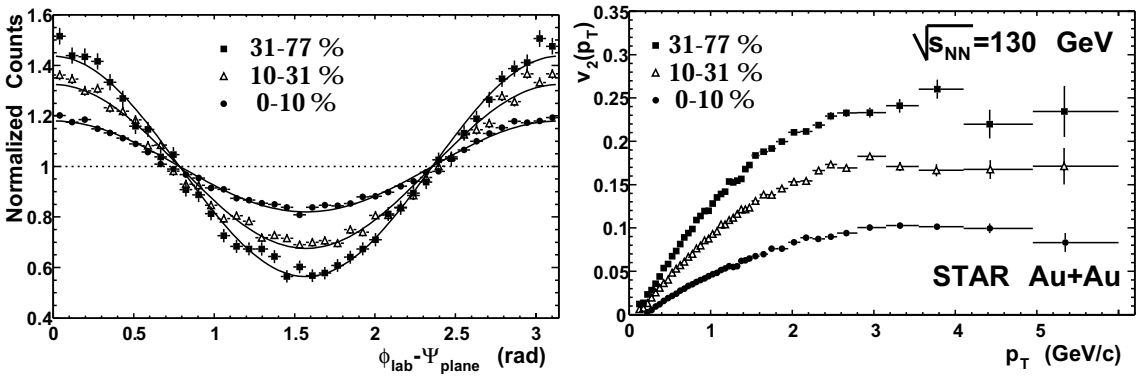

Figure 1.6: Left: The azimuthal distribution with respect to the event reaction plane for charged particles $2.0 < p_\perp < 6.0$ GeV/c from Au+Au collisions at $\sqrt{s_{\rm NN}}$= 130 GeV. The 0-10%, 10-31%, and 31-77% represent different classes of centrality where 0-10% is the most central. Right: The differential v_2 for three centrality intervals [23].

decomposed via:

$$\frac{d^3N}{p_\perp dp_\perp dy d\phi} = \frac{d^2n}{p_\perp dp_\perp dy}\left[1 + 2\sum_\alpha v_\alpha \cos(\alpha[\phi - \Psi_{RP}])\right]. \tag{1.10}$$

The harmonic coefficients, v_α, are anisotropy parameters, $p_\perp$, y, and ϕ are the respective transverse momentum, rapidity, and azimuthal angle for the particle, and Ψ_{RP} is the reaction plane angle. Due to the overlap shape, the second coefficient, v_2, is the largest and most studied parameter. For $\sqrt{s_{NN}} > \sim 4$ GeV, v_2 is positive and rises monotonically with center of mass energy. At the RHIC energy of $\sqrt{s_{NN}} = 200$ GeV, the cross section for jet production, which also creates azimuthal correlations in final-state momentum space, becomes significant. Such "non-flow" effects are estimated to contribute to, at most, a ∼5-20% overestimate of v_2 measurements [24]. New techniques are therefore being developed to aid in the subtle unfolding of these phenomena.

Fig 1.6 shows v_2 as a function of $p_\perp$ for three centrality classes. v_2 grows smoothly with $p_\perp$ and then plateaus for $p_\perp > \sim 2$ GeV/c, reaching a maximum of ∼25% for the 31-77% event class. The region $p_\perp < 2$ GeV/c is well described by hydrodynamic models[31], whose assumptions are most reasonable at low-$p_\perp$. The region $p_\perp > 2$

[31]We describe these calculations in more detail in Sec 7.

GeV/c was a complete surprise. Results for $\sqrt{s_{NN}} = 200$ GeV collisions are similar, with the peak value of v_2 being slightly larger. The mechanism generating finite v_2 at high-$p_\perp$ is yet unknown. One explanation stems from partonic energy loss. Due to finite eccentricity, a hard-scattered parton's escape distance L depends on the azimuthal angle ϕ. As the energy loss is a strong function of L, this mechanism can generate an anisotropic distribution of high-$p_\perp$ particles in the final state.

Second, suppression of high-$p_\perp$ single particles has been measured at RHIC via the comparison of single particle $p_\perp$ measurements in Au+Au and p+p collisions. To test deviations from N_{coll} scaling, one defines the ratio R_{AA} as

$$R_{AA}(p_\perp) = \frac{d^2N^{AuAu}/dp_\perp d\eta}{\langle N_{coll}\rangle/\sigma_{pp} \cdot d^2\sigma^{pp}/dp_\perp d\eta} \tag{1.11}$$

where the impact parameter dependent factor of $\langle N_{coll}\rangle/\sigma_{pp}$ accounts for the nuclear geometry. Thus deviations in R_{AA} from unity signify modification of the Au+Au spectrum with respect to scaled p+p; a suppression of high-$p_\perp$ particles in Au+Au is signified by $R_{AA} < 1$. Fig 1.7 shows R_{AA} of charged hadrons as measured in peripheral and central Au+Au collisions, as well as centrality integrated d+Au collisions. For

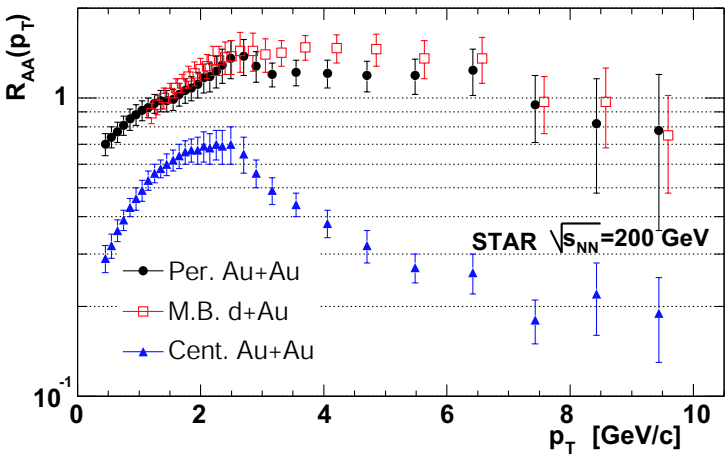

Figure 1.7: Charged hadron R_{AA} vs $p_\perp$ from Eq. 1.11 for minimum bias d+Au, peripheral Au+Au, and central Au+Au collisions. The d+Au points are displaced by +150 MeV/c for clarity. Systematic uncertainty from the N_{coll} are not shown [25].

peripheral Au+Au, R_{AA} is consistent with a value of ~1-1.2 for $p_\perp > 3$ GeV/c.

The central Au+Au data show a factor of ∼5 suppression below unity at high-$p_\perp$, in clear contrast. The d+Au data provide a crucial experimental control. As the peripheral Au+Au and d+Au data are consistent, it has been concluded [25] that the high-$p_\perp$ suppression at mid-rapidity in central Au+Au is not solely attributable to some remarkable property (shadowing of the PDFs or gluon saturation [26]) of the Au nucleus. The enhancement characterized by $R_{AA} > 1$ found in d+Au and peripheral Au+Au collisions is a well established phenomenon at lower energies. Commonly referred to as the "Cronin effect", it is generally thought to result from $p_\perp$ broadening effects in cold nuclear matter [27]. The suppression of high-$p_\perp$ particles characterized by $R_{AA} < 1$ is observed for the first time at RHIC. In Chapter 7 we show that perturbative calculations incorporating induced gluon radiation can reproduce this effect.

This analysis will address several issues. We will provide the first direct observation of jets and di-jets at RHIC, a critical first step in jet-tomography. In p+p collisions we will establish the signature of hard-scattering by studying production of charged particle jets using both direct jet identification and angular correlations of high-$p_\perp$ di-hadron pairs. This is a rather clean analysis, as shown in Fig. 1.8a. We

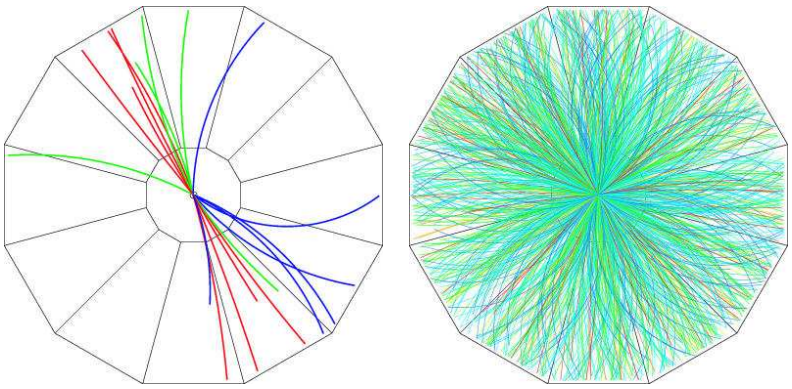

Figure 1.8: Display of reconstructed STAR jet events in a (a) p+p collision and (b) mid-central Au+Au collision at $\sqrt{s_{NN}} = 200$ GeV. The color scheme reflects the energy of the particles, and the beam direction is perpendicular to the page.

next extend the analysis into Au+Au collisions where jet reconstruction is perhaps only possible in peripheral collisions. However, the di-hadron analysis is robust even

in the dense environment of a central Au+Au collision such as that shown in Fig. 1.8b. The jet-like correlations of high-$p_\perp$ di-hadrons represent the first observation of jets in heavy ion collisions. Further, the angular correlations allow for the factorization of di-jet production into the "near" and "away" side components, and we will compare the cross-section for near-side production with that of away-side production in both p+p and Au+Au collisions. We will thus study the fate of back-to-back jets in central Au+Au collisions, searching for any hints of Bjorken's initial predictions of jet "extinction" in strongly interacting quark-gluon matter.

1.5 Outline

In Chapters 2 and 3 we introduce the experimental facilities and reconstruction software. The algorithms employed to perform jet reconstruction are presented in Chapter 4. Specifics of the data reduction are given in Chapter 5. Data analysis and results are shown in Chapter 6. In Chapter 7 we interpret the results through comparison to theory, draw conclusions, and provide an outlook of future research directions. A relation between the final state momentum and initial state parton kinematics is given in Appendix A. The QCD color charge factors for quarks and gluons are introduced in Appendix B, and Appendix C is a brief introduction to the LPM effect in QED and QCD. Appendices D and E describe the implementation of jet-finding software and Glauber model calculations. They are summarized here as a reference for fellow collaborators. Finally, Appendix F provides a glossary of acronyms used in this thesis.

Chapter 2

Experimental Facilities

2.1 Introduction

The experiments were performed at BNL[1]. BNL is a federally funded laboratory with a prolific history that includes four Nobel Prize awards in physics. The physics program at BNL now centers around RHIC which began operation in 1998. RHIC is a multipurpose colliding beam facility which uniquely provides the first colliding beams of both relativistic heavy ions and polarized protons. RHIC is complimented by four dedicated detectors, STAR[2], PHENIX[3], PHOBOS[4], and BRAHMS[5]. The STAR and PHENIX detectors are large, multi-purpose detectors that are part of an envisioned physics program that will likely stretch well into the next decade. In this chapter we describe the experimental facilities of RHIC and the STAR detector, where these thesis data were acquired.

2.2 RHIC

Currently, BNL, Fermilab and SLAC[6] house colliding beam facilities that are the centerpieces of the United States' high-energy nuclear and particle physics program. At BNL, the RHIC accelerator is delivering the highest energy nucleus-nucleus (AA) and polarized proton-proton (p+p) collisions in history, allowing for a vigorous scientific

[1]Brookhaven National Laboratory
[2]Solenoidal Tracker at RHIC
[3]Pioneering High Energy Nuclear Experiment
[4]The original experiment MARS (Modular Array for RHIC Spectroscopy) was not approved. A similar setup under the name of one of the moons of Mars was later approved.
[5]Broad Range Hadron Magnetic Spectrometers Experiment at RHIC
[6]Stanford Linear Accelerator Complex

program to explore the strong force by way of many complimentary measurements. RHIC was designed with the following driving criteria:

1. Simultaneously accelerate different species in each beam.

2. Access a wide range of collision energies from a minimum of $\sqrt{s_{\rm NN}}$= 20 GeV for Au+Au collisions to a maximum of $\sqrt{s_{\rm NN}}$= 500 GeV for p+p collisions.

3. Provide a high luminosity (L) beam, making the measurement of rare processes (small cross-sections) obtainable.

The only choice of particle accelerator that satisfies items (I) and (II) is a synchrotron with two independent beam-pipes. However, item (III) places strict requirements on the luminosity required of the collider. For a process with cross section σ_i the event rate (R_i) is given by $R_i = \sigma_i \cdot L$. The luminosity L is given by $L = fn\frac{N_1 N_2}{A}$ where N_1 and N_2 are the number of particles contained in a bunch, A is the cross-sectional area of the overlap between the two colliding beams of particles, f is the revolution frequency, and n is the number of bunches per beam. High luminosity can therefore be achieved by maximizing f, n and N, and decreasing the beam profile A. Design performance specifications for RHIC are illustrated in Fig. 2.1.

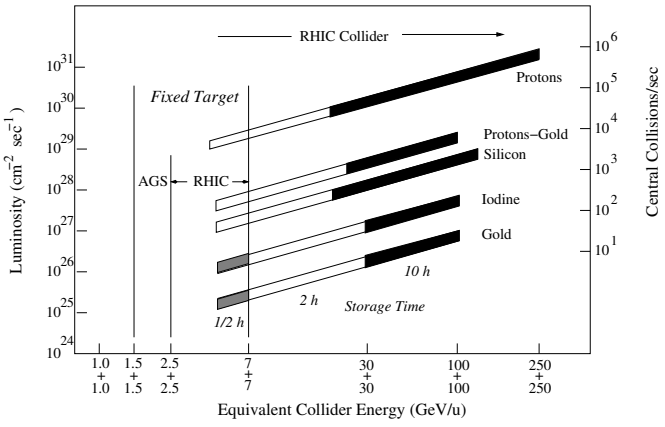

Figure 2.1: Design specifications for RHIC.

To achieve such design specifications requires a complex stage of accelerator components. As shown in Fig. 2.2, these include a Van de Graaff facility, a proton

linear accelerator, the Booster synchrotron, the AGS[7], and ultimately the RHIC synchrotron ring. All but the latter previously existed at BNL. For Au+Au operations, Au ions with charge Q=-1 are created using the Pulsed Sputter Ion Source. They are then accelerated through the Tandem Van de Graaff facility and a series of stripping foils, ultimately yielding Au ions of kinetic energy 1 MeV/nucleon and a net charge Q = +32. There are two identical Tandem Van de Graaff accelerators that can run exclusively (using one as a back up) or in parallel (to accelerate two different species simultaneously). The ions are then directed into the booster synchrotron via a 550 m transfer line. The booster accelerates the Au ions to an energy of 95 MeV/nucleon. The Au ions then leave the booster, are further stripped to Q = +77 and are transferred into the AGS, where they are accelerated to 8.86 GeV/nucleon and sorted into four final bunches. Finally, the ions are transferred from the AGS to RHIC and stripped to the bare charge state of Q = +79 during the transfer. For p+p operations, protons are injected from the 200 MeV Linac directly into the Booster synchrotron, followed by acceleration in the AGS and injection into RHIC.

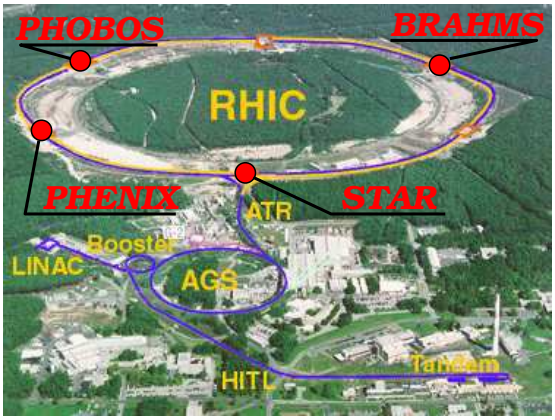

Figure 2.2: View of the RHIC accelerator complex at BNL from above. The RHIC rings are 3.8 km in circumference. See text for details.

RHIC consists of two 3.8 km concentric quasi-circular superconducting storage-accelerator rings that are called the blue and yellow rings, respectively. The rings

[7]Alternating Gradient Synchrotron

share a common horizontal plane inside the tunnel, with each ring having an independent set of bending and focusing magnets as well as radio frequency acceleration cavities. The rings consist of six arc sections and six interaction points, allowing for simultaneous collisions at six locations. The bending magnets are cryogenically cooled to $< 4.7^{\circ}$ K and yield a nominal magnetic field value of $\approx$3.8 T at the top of the ramp. The rings are focused for collision at the interaction regions by a common set of dipole magnets, the DX and D0 magnets, located at 10 m and 23 m, respectively. These common dipoles slightly reduce the independence of the blue and yellow rings. To date, RHIC has been run in Au+Au p+p, and d+Au configurations.

2.3 The STAR Detector

STAR was designed to study strongly interacting matter under extreme conditions. An emphasis was placed on describing the collisions via a broad set of measurements, in order to study both the soft (non-perturbative) and hard (perturbative) aspects of the physics at RHIC. In Au+Au collisions, the high track multiplicities allow for extraction of global observables such as centrality, "temperature", reaction plane, and mean transverse energy $\langle E_{\perp} \rangle$. A large acceptance design was thus chosen to maximize the information recorded per collision. Additionally, STAR is instrumented with a high level trigger system that allows real-time selection of rare processes such as high-$p_{\perp}$ jet, direct photon, and heavy quarkonia production. To meet these goals, STAR was designed primarily for hadron measurements over a large solid angle, featuring layered detector subsystems for high precision tracking, particle identification and electromagnetic calorimetery about mid-rapidity. At RHIC, STAR's large acceptance makes it uniquely suited for detection of hadron jets.

As shown in Fig. 2.3, STAR is built around a large acceptance ($0 \leq \phi \leq 2\pi,\ |\eta| < 1.4$) TPC[8] that provides high precision tracking of charged particles. Close to the beam pipe, the TPC is augmented by a silicon inner tracking system (SVT[9] and

[8]Time Projection Chamber
[9]Silicon Vertex Tracker

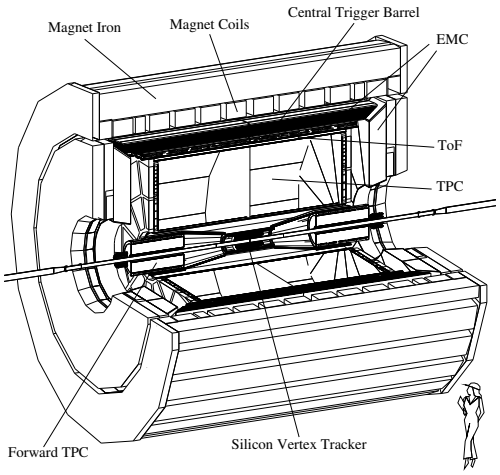

Figure 2.3: Cut-away view of the STAR detector.

SSD[10]) that yields four radial layers of high precision space points, improving the position resolution of the detector and allowing for secondary vertex reconstruction of short lived particles. Outside of the TPC is a highly segmented BEMC[11] which provides measurement of electromagnetically interacting particles, primarily photons and electrons. The $2.8 \leq |\eta| \leq 3.8$ region is instrumented with FTPC[12]s which also perform charged particle tracking. The entire apparatus is housed in a room temperature 0.5 T solenoidal magnet with a field parallel to the beam line, providing momentum measurements for the charged particles. Additionally, several detector subsystems are used for event selection purposes: the ZDC[13], BBC[14] and CTB[15].

The data collected for this analysis depend primarily on information from the TPC and the aforementioned trigger detectors. The other subsystems were still being commissioned at the time of the run. In the following sections we discuss the ZDC, CTB, the STAR magnet and finally the TPC.

[10]Silicon Strip Detector
[11]Barrel Electromagnetic Calorimeter
[12]Forward Time Projection Chamber
[13]Zero Degree Calorimeter
[14]Beam Beam Counter
[15]Central Trigger Barrel

2.3.1 Zero Degree Calorimeter

The most basic step in a collider experiment is to decide when to read out the data from the detector. This process is referred to as triggering, and schemes range from basic to complex depending on the topology of the collisions to be selected. At the most basic level, one wants to know only if a collision has occurred. Such a scheme is called a minimum bias (minbias) trigger. At the most complex level, one may want to ignore all events that do not satisfy the topology of, e.g., a top quark event. At RHIC a common minbias trigger scheme was developed for heavy ion running for BRAHMS, PHOBOS, PHENIX and STAR. The trigger is based on two ZDCs, one on each side of the interaction point. An inelastic heavy ion collision is accompanied by

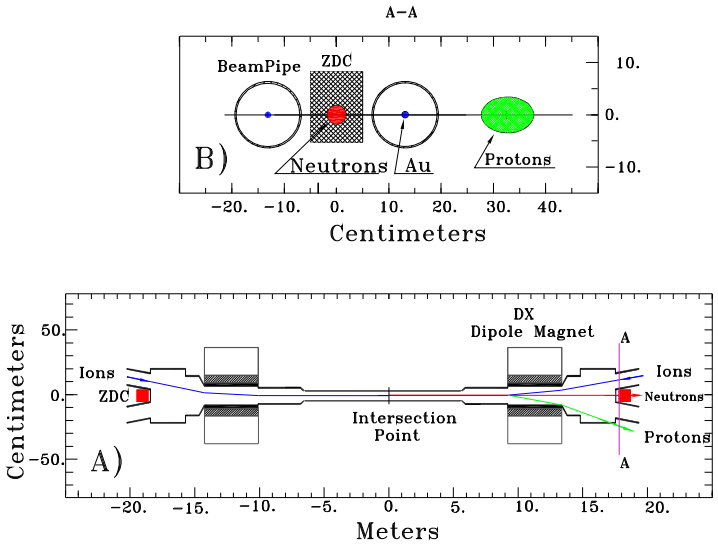

Figure 2.4: (A) Plan view of the collision region and (B) "beam's eye" view of the ZDC location indicating deflection of protons and charged fragments (with Z/A∼1) downstream of the DX dipole magnet [28].

the emission of beam remnant neutrons at high-energies and small angles ($\sim$ 2 mrad) with respect to the beam. The ZDC is a hadronic calorimeter that is designed to detect these neutrons. The ZDCs are centered at 0° approximately 18 m downstream of the interaction point and subtend 2.5 mrad. The ZDCs are located beyond the DX

magnets which bend the beams back into their respective orbits. The DX magnets additionally act to sweep away charged fragments, so only neutral fragments can reach the ZDC. Fig. 2.4 illustrates the location of the calorimeters.

The ZDCs employ layers of tungsten absorbers together with Cherenkov fibers for sampling. The light generated in the fibers is sent to a set of three PMT[16]s with the summed analog output of the PMTs used to generate the ZDC signal. The hadronic Au+Au minimum bias trigger used by STAR requires a coincidence between the two ZDCs, with each ZDC signal having a summed analog PMT output corresponding to $\sim 40\%$ of a single neutron signal. The readout electronics used at each of the experiments are identical in design. The signal from each ZDC is split in two, with one signal being sent to the RHIC control room for luminosity monitoring and the other used as input for the experiment's trigger.

2.3.2 Central Trigger Barrel

An additional design requirement of STAR was the ability to select events in real time based on mid-rapidity charged particle multiplicity. This is accomplished via a collection of scintillating tiles arranged in a cylindrical fashion around the radial exterior of the TPC (see Fig. 2.3). This collection of tiles is called the CTB[17]. As charged particles traverse a CTB tile, they generate scintillation light which is collected via a PMT and digitized. The corresponding voltage is proportional to the number of charged particles that traversed the slat. The detector is very fast (260 ns) and, in combination with the ZDC signal, allows for a powerful charged particle multiplicity trigger.

The CTB is comprised of 240 slats of plastic scintillator that cover $0 \leq \phi \leq 2\pi$, 4 m in length and $-1 \leq \eta \leq 1$. The slats are housed in aluminum trays, two slats per tray. Each slat has one radiator, one light guide, and one PMT. Fig. 2.5 shows a segment with two slats. The slats closest to the center contain tiles of 112.5 x 21 x 1cm. The slat away from the center is 130 x 21 x 1 cm. A single slat covers $\Delta\phi = \pi/30$ radians and $\Delta\eta = 0.5$. The PMT signals generated by the slats are

[16]Photo Multiplier Tube
[17]Central Trigger Barrel

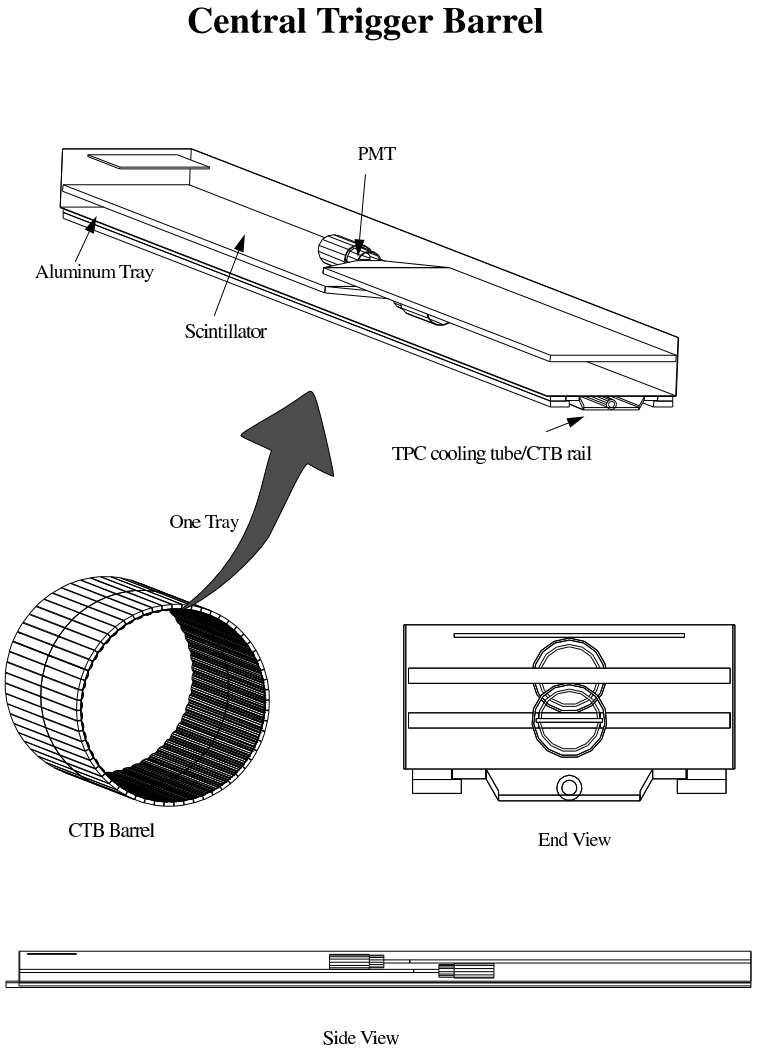

Figure 2.5: CTB cylinder and detail of tray and slat [29].

sent to digitizer boards, each having 16 inputs. Within each digitizer, the signals are sent to an integrator, an 8-bit ADC[18], and then to a discriminator. The output of the discriminators can be summed over the barrel and used in the trigger logic. The

[18]Analog to Digital Conversion

CTB calibration yields an average of 5 ADC counts for a minimum ionizing particle. The average occupancy in the CTB for central Au+Au collisions was 10 hits per slat. However, in p+p collisions an individual slat had on average a 5% chance of being hit in an event.

2.3.3 Beam Beam Counter

The ZDC and CTB are specifically designed for triggering in Au+Au collisions. The topology of p+p collisions is vastly different and thus requires a different trigger subsystem. Non-singly diffractive (NSD) inelastic interactions are characterized by the breakup of both incoming protons. The hard scattered partons are realized in the final state as particles near mid-rapidity, while the remnant partons produce two "beam-jets". The beam-jets are groups of high-energy hadrons that are focused in the high (near beam) rapidity region. A traditional trigger for NSD interactions is therefore a set of two scintillating disks that are sensitive to the beam jet region. STAR thus implements a two-disk BBC[19] system.

The BBC subsystem consists of two disk shaped scintillating detectors, with one placed at each endcap of the TPC (3.5 m from the interaction point). Fig. 2.6 shows a schematic drawing of one of the two BBC detectors. Each BBC disk is composed of scintillating tiles that are arranged in a hexagonal closest packing. For the first p+p run, only the small tiles in the inner region were instrumented with readout electronics, yielding an active region of $3.3 \leq |\eta| \leq 5.0$. The RHIC beam line passes through the center of the BBC (see Fig. 2.6) with a 1 cm annular clearance.

Eight PMTs were used for the 18 inner tiles. Each tile has a circular groove inscribed around the perimeter, into which a wave length shifting optical fiber is embedded. The scintillation light is collected in the fiber, sent to a PMT and digitized via an ADC[20]. The tiles are grouped to allow for radial and azimuthal segmentation of the readout. The grouping is: 1, 2-3, 4, 5-6, 7-9, 10-12, 13-15, and 16-18. The full segmentation of the BBC was not used in the p+p trigger logic. The trigger summed the output of all tiles on the BBC, and a coincidence of both BBC's firing above

[19]Beam Beam Counter
[20]Analog to Digital Conversion

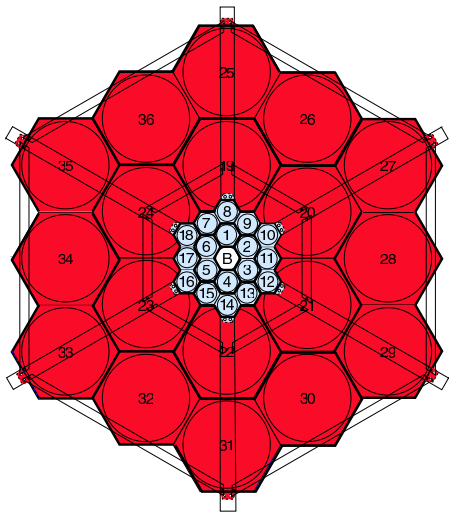

Figure 2.6: A beam's eye view of the BBC. The beam is perpendicular to the page and intersects the BBC in the non-instrumented region labelled 'B'. For scale, the inner region (tiles 1-18) lie within an approximate circle of radius ∼10 cm.

noise threshold was required within a time window of $\Delta t \equiv |t^{BBC}_{east} - t^{BBC}_{west}| < 17$ ns, which is determined by the time resolution of the detector. For future runs the BBC is being fully instrumented with electronics to maximize the potential acceptance and granularity.

2.3.4 STAR Magnet

Momentum measurements are performed at STAR by measuring the helical trajectories executed by charged particles in the presence of a magnetic field that is parallel to the beamline (z). The magnet design was driven by the following criteria. The magnet should provide:

- kinematic acceptance for low-$p_\perp$ particles
- good momentum resolution for high-$p_\perp$ particles
- a highly homogeneous field to minimize electron drift distortions

The first two items drove the choice of the field strength, and a conventional (non-superconducting) design was chosen for (short-term) budgetary concerns. The magnet [30] is cylindrical in design with a length of 6.85 m and has inner and outer diameters of 5.27 m and 7.32 m, respectively, as shown in Fig. 2.7. Two pole tips placed on

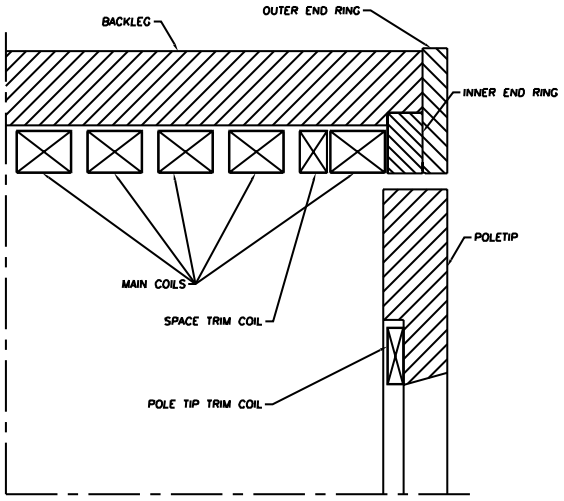

Figure 2.7: Section drawing of magnet steel and coil locations. Dimensions are given in the text [30].

either end complete the design, and along with the rest of the magnet steel act as a return path for the field flux. The magnet generates a field along the length of the cylinder having a maximum of $|B_z| = 0.5$ T. After installation the field was mapped and optimized using a field mapper from CERN[21]. Field maps were produced for both polarities at full and half fields. The full field map had a mean $B_z = 0.498$ T and ranged from 0.4950 to 0.5010 T.

Momentum measurements are accomplished by the determination of the radius of curvatures of particles traversing the magnetic field. High-$p_\perp$ resolution is dominated by the accuracy of the curvature measurement. Inhomogeneities in both the magnetic and electric drift fields affect this measurement of the curvature and thus provide an upper bound on the allowable field distortions [31], as discussed below. The drift velocity of electrons in STAR's tracking detector's gas volume can be obtained from

[21] l'Organisation Européenne pour la Recherche Nucléaire

the Langevin equation

$$\overrightarrow{v_D} = \frac{\mu}{1+(\omega\tau)^2}\left(\overrightarrow{E} + \omega\tau\frac{\overrightarrow{E}\times\overrightarrow{B}}{|\overrightarrow{B}|} + (\omega\tau)^2\frac{\overrightarrow{B}\left(\overrightarrow{E}\cdot\overrightarrow{B}\right)}{\overrightarrow{B}^2}\right), \tag{2.1}$$

where μ is the electron mobility, ω is the cyclotron frequency and τ is the mean drift time between two collisions in the gas. Here the B field is completely known from the field map. The E field (provided by the field cages of the TPC) could not be mapped and was calculated using electrostatic methods [30]. In the case of perfectly aligned $\overrightarrow{E}$ and $\overrightarrow{B}$ fields the drift velocity of electrons in the TPC gas will be simply $\overrightarrow{v}_D = \mu\overrightarrow{E}$. Field imperfections will impart non-zero drift velocities to the electrons in directions not aligned to the main $\overrightarrow{E}$ field component and can lead to errors in the tracking. Radial field distortions will result in drift velocities in the azimuthal direction

$$v_\phi = \frac{\mu E_z \omega\tau}{1+(\omega\tau)^2}\left(\frac{B_r}{B_z} - \frac{E_r}{E_z}\right). \tag{2.2}$$

The total azimuthal shift caused by these field distortions can be obtained by integrating over the time it takes the electrons to drift to the electronic readout located at the TPC's endcaps,

$$\Delta x_\phi = \int v_\phi dt = \frac{1}{v_z}\int_z v_\phi dz = \frac{\omega\tau}{1+(\omega\tau)^2}\int_z\left(\frac{B_r}{B_z} - \frac{E_r}{E_z}\right)dz \tag{2.3}$$

with a similar expression existing for the radial shift caused by field distortions. The magnetic field homogeneity requirements can now be expressed in terms of the radial and azimuthal components of the magnetic field

$$\begin{aligned} |\Im_r| &= \left|\int_{z'=210\text{ cm}}^{z}\left(\frac{B_r}{B_z}\right)dz'\right| \\ |\Im_\phi| &= \left|\int_{z'=210\text{ cm}}^{z}\left(\frac{B_\phi}{B_z}\right)dz'\right| \end{aligned} \tag{2.4}$$

As shown in Fig. 2.8, the maximum variation of the field integrals $|\Im_r|$ and $|\Im_\phi|$ within the tracking volume were found to be 0.3 cm and 0.035 cm for the radial and azimuthal components, respectively. These values for the field integrals are better than the design specifications by a factor of 2.

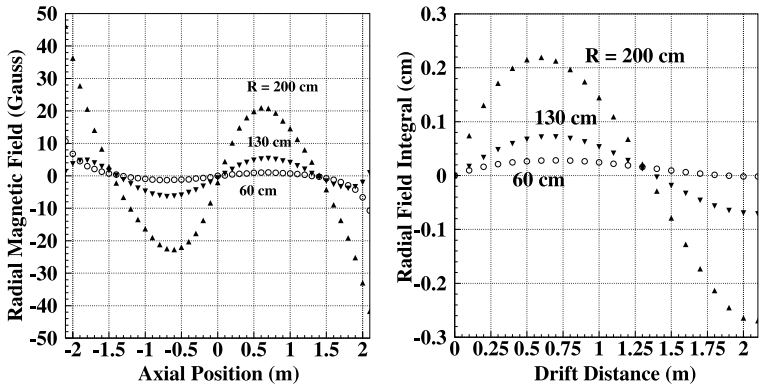

Figure 2.8: (**a**)Measurements of radial component of the STAR magnetic field (Gauss) as a function of axial (z) position for three radii at $\phi = 0°$. The center of the TPC and the magnet are at $z = 0$. The inner and outer radii of the TPC are 50 and 200 cm, respectively. (**b**) Values of the field integral ($\Im_r$) of the STAR magnetic field (cm) as a function of drift distance (z). Representative data are given at three radii in the TPC for $\phi = 0°$ and $z < 0$ (TPC East Half) [30].

2.3.5 STAR TPC

Au+Au collisions at RHIC produce ∼1000 particles per unit rapidity, creating the world's highest density tracking environment at a colliding beam facility. The heart of the STAR detector is a large volume, large acceptance TPC, which essentially performs as a 70 Mega pixel[22] digital camera, allowing for the 3-d reconstruction of nearly all of the charged particles produced in each Au+Au collision.

Time Projection Chambers generally consist of a large gas volume contained in a homogeneous electric field. Electrons, liberated as a charged particle traverses the gas, drift in the electric field to a detection device (generally a wire chamber). Two coordinates are determined by the location where the electron is detected. The third coordinate is reconstructed using the time taken for electron to reach the wire chamber (time bin) and the electron drift velocity of the gas (v_{drift}).

The TPC has a large acceptance and excellent momentum resolution. Consisting of a 4.2 m long cylinder 4 m in diameter, it is the largest single TPC in the world

[22] 5692 pixels/sector × 24 readout sectors × 512 time-samples/event ≃ 7·10^7 pixels/event.

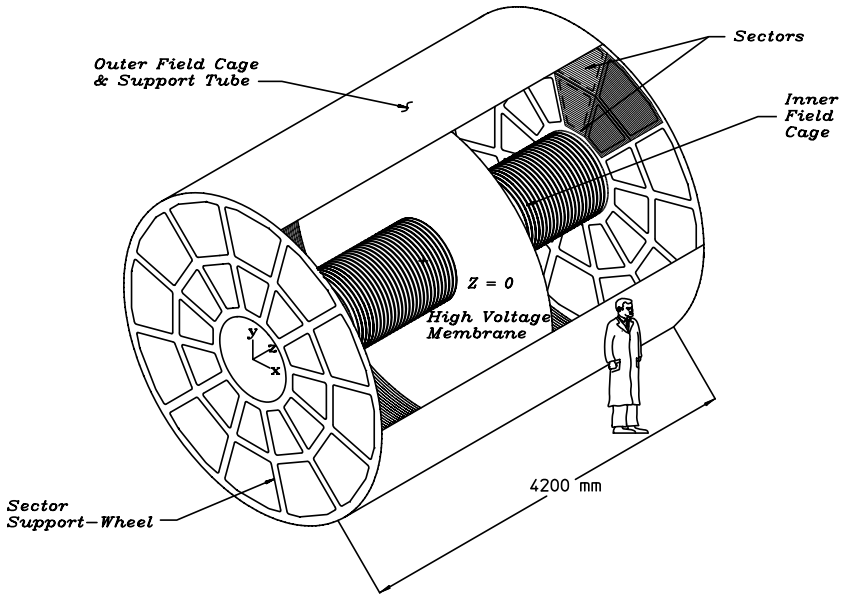

Figure 2.9: Schematic of the STAR TPC [32].

[23](see Fig. 2.9). The cylinder is concentric with the beam line, and the inner and outer radii of the active volume are 0.5 and 2.0 m, respectively. This introduces a lower cutoff of $p_\perp \sim$ 150 MeV/c for tracks accepted into the TPC's tracking volume ($\sim$ 75 MeV/c for 0.25 T). The TPC covers the full region of azimuth ($0 \leq \phi \leq 2\pi$) and covers a pseudorapidity interval that ranges from $-2 < \eta < 2$ for the inner radius to $-1 < \eta < 1$ for the outer radius (see Fig. 2.10). To achieve sufficient $p_\perp$ resolution one generally requires that a track cross $\sim$15 padrows, which effectively limits the pseudorapidity coverage to $-1.4 < \eta < 1.4$.

The TPC volume is filled with P10 gas (Ar, 10% CH_4) at $\sim$ 2 mbar above atmospheric pressure. A particle with charge z traversing a gas of charge number Z and mass number A loses energy by ionizing the gas. The energy loss per distance

[23]The ALEPH TPC was 1.75 m long with a 0.9m radius. NA49[24] had two slightly smaller TPCs, but with a larger combined total volume. The STAR TPC is, however, the biggest TPC in the world to roll on wheels!

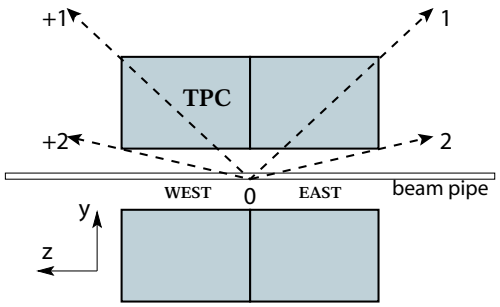

Figure 2.10: Schematic view of the TPC illustrating the coordinate system and pseudorapidity coverage. The x-axis points out of the page.

travelled is given by the Bethe-Bloch formula

$$\frac{dE}{dx} \approx Kz^2 \frac{Z}{A} \frac{1}{\beta^2} \left(\frac{1}{2} \ln \frac{2m_e c^2 \beta^2 \gamma^2 T_{max}}{I^2} - \beta^2 \right) \tag{2.5}$$

where $K \approx 0.31$ MeV cm^2, β and γ are the usual relativistic variables, T_{max} is the maximum kinetic energy imparted to a free electron in a single collision, and I is the mean excitation energy. Charged particle identification in the STAR TPC is thus possible over a limited range of momentum ($p < \sim 1$ GeV) by simultaneously measuring dE/dx and p for charged particles.

The secondary electrons are drifted in the electric field to two detection planes, one on each end of the chamber ($z \simeq \pm 210$ cm). A large diaphragm made of carbon coated Kapton (Central Membrane) having a thickness of 70 μm is stretched between the inner and outer field cages at the center of the TPC ($z = 0$ cm). The Central Membrane is maintained at a high voltage with respect to the detection planes. The liberated electrons therefore drift away from the central membrane to the closest end cap of the TPC, where their position in the r vs. ϕ plane is determined as a function of time. The mean drift time constitutes a measurement of the electron's ionization point along the z axis, yielding the third dimension.

Field Cage Design

The TPC requires the presence of a uniform electric field ($\overrightarrow{E}$), which is created using a set of field cages (see Fig. 2.9). The field cage design consists of two concentric

cylinders which define the active volume of the TPC. A highly uniform electric field is created along the axis by a series of equipotential rings placed on the surfaces of the inner and outer field cages. The magnitude of the field is greatest at the central membrane which is biased at -31 kV and decreases in a steady manner to 0 V at the ground wires located on either end of the TPC. Irregularities in the spacings of the rings or in the rings themselves will result in radial field components and consequently lead to a degradation in the momentum resolution. Field calculations [32] have shown electric field distortions to be well within the design specifications.

The field cage was designed to provide maximal structural integrity while minimizing the mass of the construction material. The field cages were built using two sheets of metal coated Kapton separated by a honeycomb of Nomex. The whole assembly was rolled into a tube and the sheets of Kapton were epoxied to the honeycomb. The Kapton in the OFC[25] is laminated with a 35 micron layer of copper and the metal

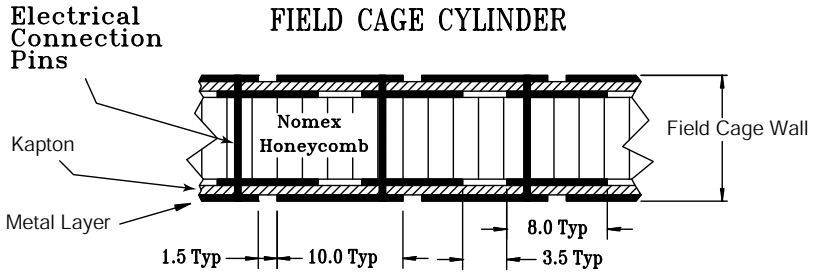

Figure 2.11: An IFC showing the construction and composition of the cylinder wall. Dimensions are in mm [32].

layer is etched into stripes which form the equipotential rings used to establish the electric field within the TPC gas volume. The IFC[26] (Fig. 2.11) is similar to the OFC but the Kapton is laminated with a thinner layer of Aluminum (9 micron) and the Nomex layer is thicker (1.27 cm). The rings are spaced 1 cm apart and are biased by a chain of 2 $M\Omega$ resistors. The OFC rests inside an aluminum gas containment vessel which is separated from the OFC by 5.7 cm of nitrogen gas.

The electric field and the gas conditions determine the drift velocity (v_{drift}) of electrons in the TPC. v_{drift} is measured in several fashions, but a primary calibration

[25]STAR TPC Outer Field Cage
[26]STAR TPC Inner Field Cage

makes use of a mirrored laser system where a single beam is split into many beams of known location. The beams ionize the P10 gas and the electrons are detected in the MWPC[27]. The known location of the beams allows for an absolute calibration of v_{drift}. Such laser events are interspersed in regular data taking to provide running calibration. The drift veolicty was calculated to be 5.44 ± 0.01 cm/μs, with typical time dependent variations on the order of ∼6%.

Multi-Wire Proportional Chamber

Located on each end of the TPC are a set of detection planes to measure the location and arrival times of the drifting secondary electrons. Each detection plane is instrumented with a thin MWPC together with a pad chamber readout. As the electrons near the MWPC wires, their signal is amplified via an avalanche process. The avalanche cloud induces an image charge on the pad readout. This image charge is collected and digitized via an ADC. The design specifics of the MWPC and pad system were chosen to meet the following requirements:

1. Provide an adequate signal-to-noise ratio (∼20:1) for position resolution
2. Operate the MWPC in the proportional region to maintain reasonable $\frac{dE}{dx}$ resolution
3. Provide sufficient spatial resolution to meet two track separation and $p_\perp$ resolution requirements in the high density inner region
4. Maximize the number of $\frac{dE}{dx}$ measurements along a particles trajectory
5. Ensure a reasonable amount of electronic channels in the readout

The first two items drive the choice of the gas gain used, while the last three items drive the choice of pad size, spacing, and sampling rate. Below we describe the structure and operation of the TPC readout system.

As shown in Fig. 2.12, each detection plane consists of twelve pad plane arrays (sectors), arranged in a circular fashion. Each sector is divided radially into an inner

[27]Multi Wire Proportional Counter

and outer subsector (Fig. 2.13). The outer sector consists of 3940 pads of 6.2 by 19.5 mm distributed in 32 rows. To optimize position resolution in the transverse plane, the pad sizes were chosen to maximize the probability of a hit being shared over three pads. Additionally, the pads are closely packed to maximize the amount of charge collected on each pad, thus optimizing the $\frac{dE}{dx}$ resolution. The inner sector contains 1750 rectangular pads of 2.85 by 11.5 mm distributed over 13 rows. The pad spacing between rows is larger in the inner sector to cope with the higher hit density. Information from padrow 13 is excluded from reconstruction due to electrostatic field effects that are not yet understood. Information from padrow 1 is rarely used, as that padrow is generally saturated by the high particle hit density.

Figure 2.14 shows the configuration of the MWPC defined by a set of wire planes and shows their relative position with respect to the pad plane arrays for the inner and outer sectors. The drifting electrons first pass through a gating grid which acts to separate the drift region of the TPC from the amplification region. The drift electrons are collected on the gating grid wires when the gate is closed, and are only allowed to pass through to the amplification region for events meeting the proper triggering

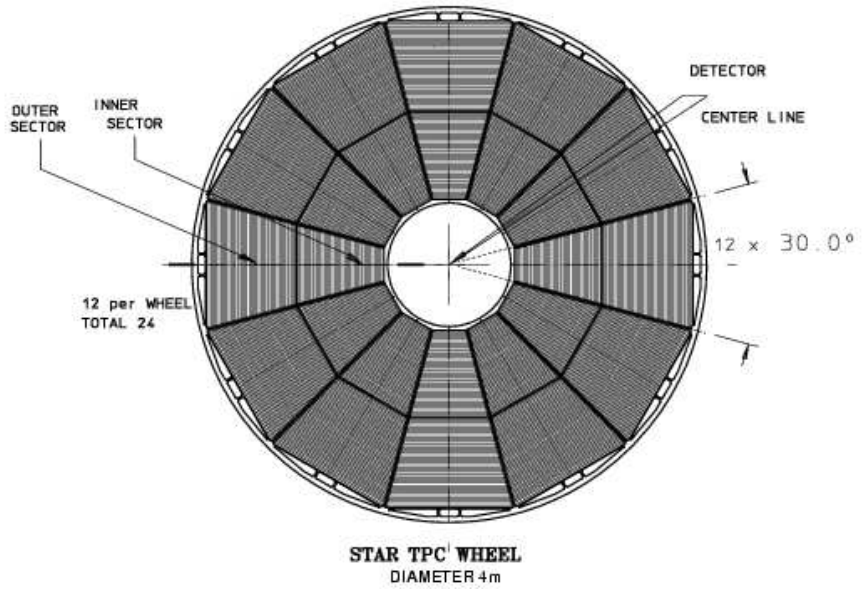

Figure 2.12: TPC sector layout.

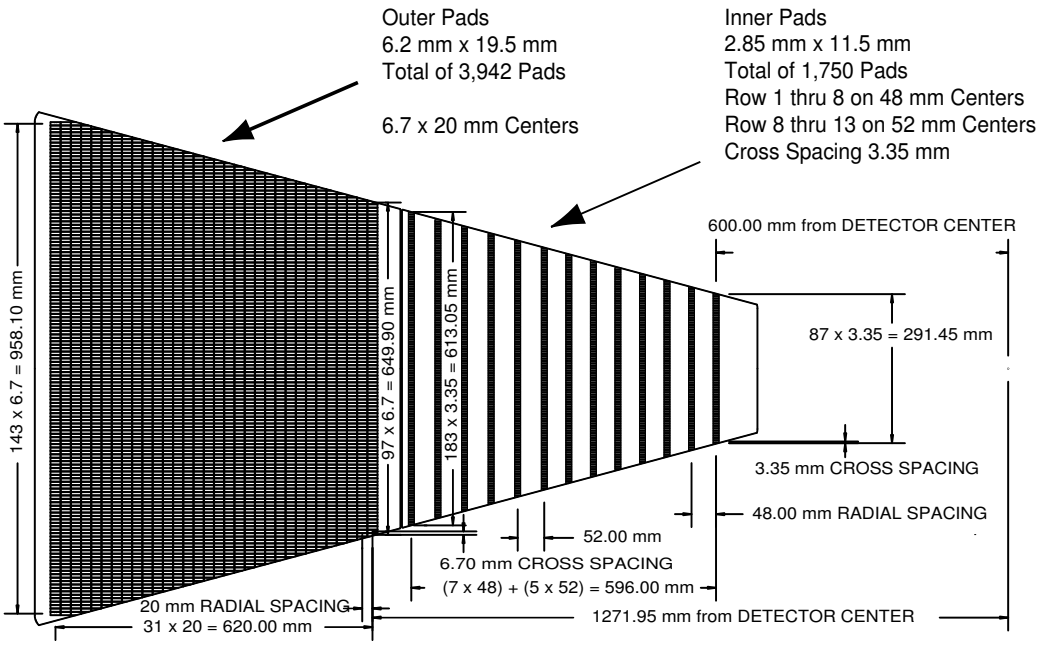

Figure 2.13: Detail of a single super-sector showing inner and outer sectors [32].

conditions. The ground plane acts to define the effective volume of the MWPC. High

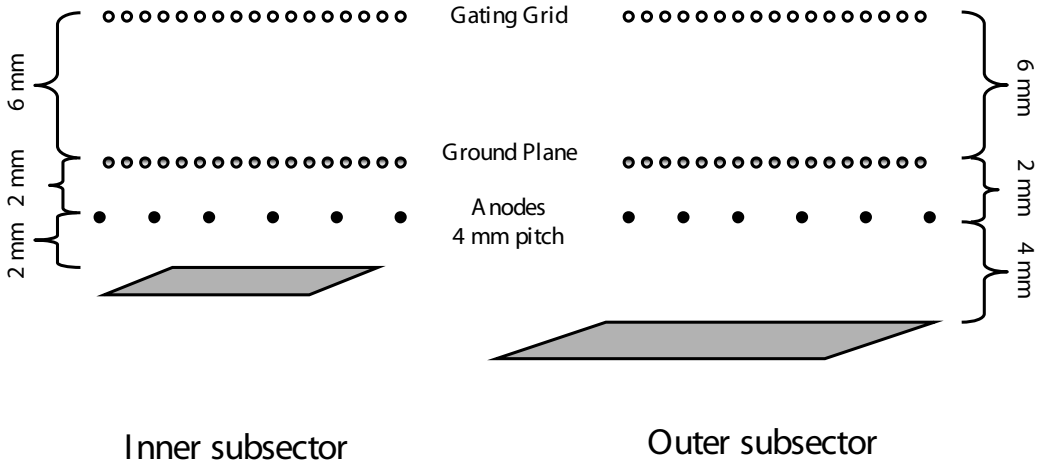

Figure 2.14: The readout chamber region of the STAR TPC. The gating grid and ground plane wires are on a 1 mm pitch, while the anode wires are spaced every 4mm [33].

tension anode wires are placed directly above each pad plane. Drift electrons are

multiplied by avalanches near the anode wires. The ions created in this avalanche process induce a signal on readout pads directly below the anode wires.

Drifting electron clouds diffuse in both the longitudinal and transverse directions. The transverse diffusion in P10 gas [34] is 230 μm/$\sqrt{\text{cm}}$ or σ_T=3.3 mm for a 210 cm drift, thus setting the scale for the pad size. The longitudinal diffusion over a 210 cm drift is σ_L=5.2 mm. A consideration of σ_L yields an estimate for the charge cloud's longitudinal width of $\sim$ 5 mm, which extends $\sim \frac{5 \text{ mm}}{v_{drift}} \backsimeq 100$ ns in time. This determines the sampling rate of 10 MHz. Fig. 2.15 shows the chamber's position resolution in Au+Au events at both full and half field settings. For vertical tracks ($\theta = 90°$) normal to a padrow, a resolution of $\sim$ 400 μm and $\sim$ 750 μm is achieved in the transverse and drift planes, respectively.

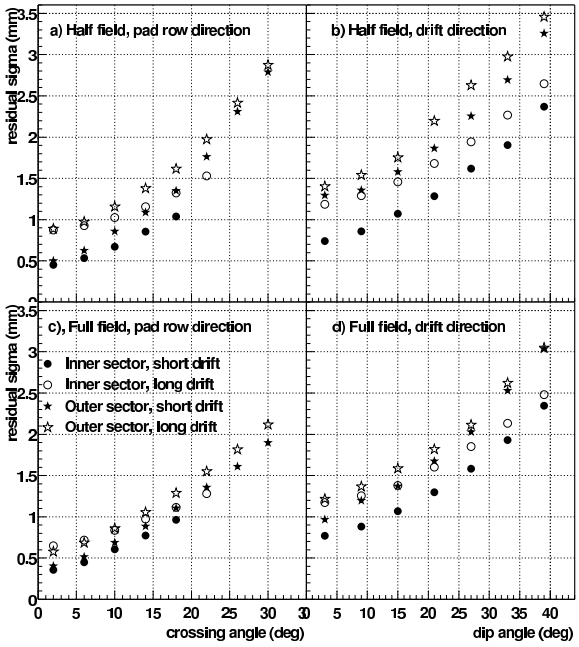

Figure 2.15: Position resolution across the pad rows and along the z-axis of the TPC. The crossing angle is the angle between the particle momentum and the pad row direction. The dip angle is the angle between the particle momentum and the drift direction, $\theta = \cos^{-1}(p_z/p)$ [32].

The gas gain has to be high enough to ensure an adequate signal-to-noise ratio (20:1) for position resolution, while at the same time be small enough to be in the

proportional region in order to maintain a reasonable dE/dx resolution. The gas gain used in the outer sector is ~ 1100. The smaller pad size for the inner sector requires a larger gain (~ 3000) be used in order to ensure the same signal-to-noise ratio of 20:1. The dynamic range of the signal has to accommodate the amount of charge liberated by a highly ionizing particle traveling through the TPC's gas volume and was set at 10 bits. The signal induced on a pad is amplified and integrated by a circuit containing a pre-amplifier and shaper. The signal is sampled at the rate of 10 MHz as discussed above and is stored using a switched capacitor array (SCA). The event is digitized and transmitted over a set of optical fibers to the STAR DAQ[28]. In previous runs the data rate to tape has averaged 10-30 Hz, depending on collision system and trigger criteria.

2.3.6 Detector Material

Structure	Material	Density (g/cm^3)	X_0 (g/cm^2)	Thickness (cm)	Thickness (%X_0)
Beam pipe	Be	1.848	65.19	0.5	x
1 SVT layer	Si, Be Graphite	NA	NA	0.36	0.02
SVT Total					3×0.02
Insulating gas	N_2	0.001	37.99	30	0.10
TPC IFC	Al	2.700	24.01	0.004	0.04
TPC IFC	Kapton	1.420	40.30	0.015	0.05
TPC IFC	Nomex	0.064	40	1.27	0.20
TPC IFC	Adhesive	1.20	40	0.08	0.23
IFC Total (w/gas)					0.62
TPC gas	P10	1.56E-03	20.04	150.00	1.17
TPC OFC	Cu	8.96	12.86	0.013	0.91
TPC OFC	Kapton	1.420	40.30	0.015	0.05
TPC OFC	Nomex	0.064	40	0.953	0.15
OFC	Adhesive	1.20	40	0.05	0.15
OFC Total (w/gas)					2.43

Table 2.1: Approximate material thickness for the STAR tracking volume.

Charged particles suffer angular deflections as they pass through material. The

[28]Data Aquisition System

magnitude of these scattering angles depends on the particle type and momentum, as well as the composition of the material. As such deflections degrade the momentum resolution it is important to specify the amount of material in the tracking region of the TPC.

The RMS[29] angular deflection suffered by a particle of momentum p, charge z, and velocity β is given as

$$\theta_0 = \frac{13.6 \text{ MeV}}{\beta cp} z \sqrt{\frac{x}{X_0}} \left[1 + 0.038 \ln \frac{x}{X_0} \right] \tag{2.6}$$

where x/X_0 is the percent radiation length of the material. Table 2.1 contains the various materials a particle traverses on a path from the beam pipe to the outer region of the TPC. Because the SVT construction is complex, the material structure has been approximated. All six layers of the SVT yield an average radiation length of $\sim 6\%$, while the TPC yields an average radiation length of $\sim 3\%$. Including the beam pipe and the air in the experimental region, the total thickness is ~ 12 %. A 2 GeV/c pion will therefore be deflected by $\theta_0 < 0.15^\circ$. This is well within the design specifications to provide sufficient momentum resolution.

[29]Root Mean Square

Chapter 3

STAR Event Reconstruction

3.1 Introduction

The process of transforming raw detector information into analyzable physics quantities is referred to as event reconstruction. It consists of executing a complex set of algorithms which are implemented in a large chain of various software modules. This process begins by first reconstructing three dimensional space points from the information provided by tracking detectors. Second, these hits are analyzed by a pattern recognition algorithm to group sets of hits coming from common tracks. Third, each track must be fit to a track model, characterizing the three momentum $\overrightarrow{p}$ for this trajectory. Fourth, tracks coming from the primary beam-beam interaction point (primary tracks) are separated from those that do not come from this point (secondary tracks). Finally, primary tracks are re-fit to a track model using the high precision information from the identified primary vertex.

The software used for event reconstruction is currently in flux. A transition from highly refined and TPC centric legacy code (composed in FORTRAN) to object oriented c++ software will occur in January 2004. This change is primarily driven by the addition of new tracking and calorimeter subsystems in STAR. The description here refers to the legacy software which was used to reconstruct the data presented in this thesis[1].

STAR follows a design philosophy common to many collider detectors. Charged particle tracking is performed by several elements. First, a large volume gas ionization chamber (in this case the TPC) is used for the bulk of pattern recognition (track

[1]A substantial fraction of the author's graduate career was devoted to design, implementation, and testing of the new reconstruction software

finding). These tracks are then extrapolated to successive layers of inner detectors (such as silicon) which offer high precision measurements that greatly refine the momentum resolution. Reconstruction is therefore decoupled into different stages. While the data presented here were taken with the SVT activated, the SVT information was not used in the tracking reconstruction chain.

In section 3.2 of this chapter we discuss the elements of the STAR reconstruction software that are primarily responsible for track finding, fitting, and vertexing in the TPC. In section 3.3.3 we present the method used to determine the TPC track reconstruction efficiency.

3.2 TPC Reconstruction

As charged particles traverse the TPC, they liberate electrons from the TPC gas. These electrons are drifted in a uniform electric field towards the end cap of the TPC. There the charge signal is amplified to higher voltage, recorded, and electronically converted to a digital ADC value between 0 and 512. This process is repeated as a function of time bin. The digitization of the TPC information results in $\sim$70 million ADC values with a characteristic total size of $\sim$20 Megabytes per event. From this data volume charged particle trajectories (tracks) must be reconstructed. Tracks must then be extrapolated into the inner tracking subsystems (SVT) and refit using the high position resolution of the additional points.

3.2.1 TPC Hit Finding

The TPC reconstruction process begins by creating three dimensional space points from the TPC pixel data[2]. A TPC pixel consists of several pieces of information: pad number, time bin, and ADC value. Additionally, the location of this pad is known, which ultimately allows for a transformation to global 3d coordinates. The signal from a liberated electron can be shared between several pads and several time bins. The first step in the reconstruction process is then to find groups of pixels which are

[2]We here follow STAR's colloquial use of "pixel" to mean a two-dimensional charge measurement from a specific time-bin.

close together in both position-space and time. This is referred to as TPC cluster finding. This proceeds by the following algorithm:

- Identify a pixel with ADC value above a certain threshold.
- Search for pixels in adjoining pads and time bins.
- Collect these pixels as being from a common cluster and mark them as used.
- Repeat until no unused pixels remain with ADC value above threshold.

It is important to note that corrections for bad pads and relative timing information is applied at the cluster finding stage. Figure 3.1 shows an example of two identified clusters.

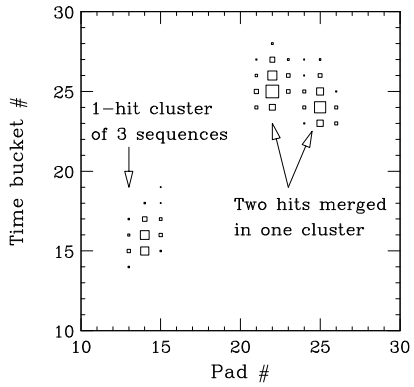

Figure 3.1: An example of two clusters found by the TPC clustering algorithm. The size of the boxes represents the ADC value of the pixels. [35].

The next step is to turn clusters into 3d space points called TPC hits. Intersecting tracks in the TPC can result in more than one hit being reconstructed in the same cluster. Each cluster is analyzed and a search for one or more maxima within the cluster is performed. Merged hits are recognized by studying the cluster width in both pad and time dimensions. Clusters with a RMS value beyond a characteristic width are assigned as consisting of two merged hits. The selection is approximately based on the relation

$$\sqrt{RMS_{pad}^2 + RMS_{time}^2} \leq 2 \tag{3.1}$$

Clusters that consist of merged hits are split according to a deconvolution algorithm into two sub-clusters. Once one or more maxima are found, the mean time and space values are characterized by an independent three point Gaussian fit in both the space and time dimensions. The final step of hit finding is to transform from local coordinates (sector, padrow, pad, time bin) to global cartesian coordinates specified in Figure 2.10. The transverse coordinates x and y are completely defined by the sector, padrow, and pad values. However, the value of the time bin must be mapped to a distance along the beam direction z. This mapping depends on the drift velocity (v_{drift}) of an electron in the TPC gas, which was discussed in Sec. 2.3.4, as well as the time offset between the trigger start time and the beginning of the TPC readout (t_0). The following equation is used

$$|z_{hit}| = L_{tpc} - v_{drift} \cdot (t_{hit} - t_0) \tag{3.2}$$

where L_{tpc} is the TPC length and the negative sign before v_{drift} arises from the direction of the electric field. The sign of z_{hit} is determined by whether the hit originates from the east or west half of the TPC with positive z in the west half.

3.2.2 TPC Track Finding

The final product of TPC hit finding is a collection of points reported in global cartesian coordinates. The next step is to perform pattern recognition to identify hits coming from the same charged particle (track). For a track that exits the outer radius of the TPC, the maximum number of TPC hits is equal to the number of padrows (45). The TPT[3] algorithm can be classified as a "local" algorithm which identifies points that lie close in space (seeds), constructs segments from these points, then successfully merges neighboring segments. The algorithm was originally used in the ALEPH and NA35 experiments at CERN and has been refined for specific application to the STAR TPC. The pattern recognition program flow is illustrated in Figure 3.2 and described below.

The first step is to identify groups of 3 hits that are close in space (3-point seeds).

[3]Time Projection Chamber Tracker

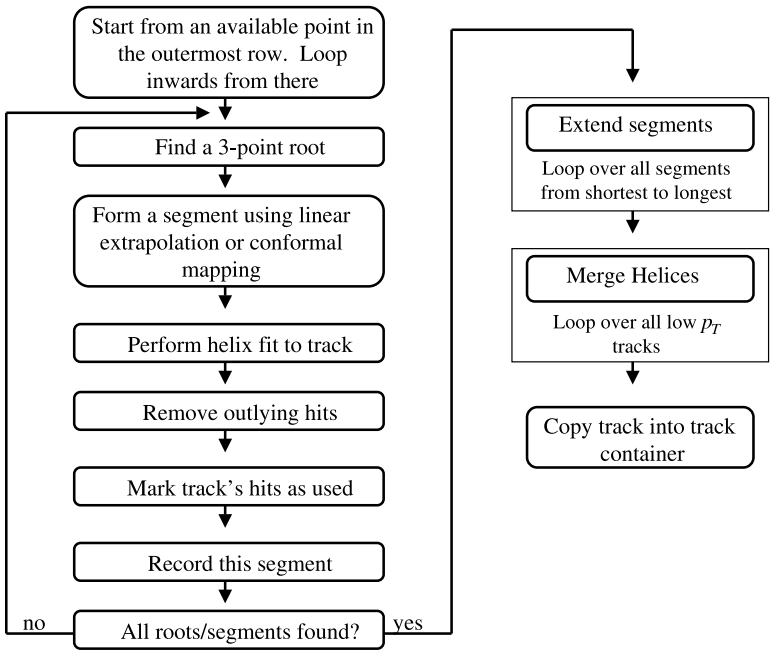

Figure 3.2: Program flow of the STAR track finding algorithm [36].

This process begins at the outermost padrow of the TPC where the detector occupancy is the lowest. TPT manipulates the knowledge of the average cluster properties to find seeds. Primarily, clusters are spread over an average of 3 time bins. Thus, series of 3 hits that overlapped in time are connected. These 3-point seeds are then characterized by a straight line segment. Using this line an extrapolation is performed inwards to the next padrow. Hits lying near the point of extrapolation are added to the seed. These four points (called a track segment) can then be used to define a reasonable helical trajectory. Once a segment is formed, the hits are marked as used and removed from the hit pool. The process of finding a new 3-point seed then begins again using the unused hits in padrow 45. When all hits in padrow 45 are marked as used, then the process begins again in padrow 44, and so on.

The next step is to use a helical extrapolation (actually performed via a conformal mapping of a circle to a line) to add additional points to the segments. This proceeds by extrapolating both inwards and outwards from each segment, adding all possible hits that are near the extrapolation until the extrapolation exits the TPC. Any new

hits added to the segment are marked as used and removed from the hit pool. The final pattern recognition step in TPT is to attempt to merge any segments from tracks that may have been artificially reconstructed in two or more segments. This primarily happens for low-$p_\perp$ tracks that form large angles with respect to the TPC padrows.

Once pattern recognition ends, the TPT package next fits each collection of points to a track model. A charged particle traveling through a constant magnetic field along the z direction follows a helical equation of motion. A well defined track model is a major advantage of the STAR experiment, as it allows one to make precise extrapolations of a trajectory into non-instrumented regions, e.g., inside the beam pipe. These extrapolations are heavily used in the analysis presented in this thesis. Therefore, we explicitly describe the parametrization of the model.

The parametrization describes the helix in Cartesian coordinates, where x, y and z are expressed as functions of the track length s.

$$x(s) = x_0 + \frac{1}{\kappa}[\cos(\Phi_0 + h\ s\ \kappa\ \cos\lambda) - \cos\Phi_0] \tag{3.3}$$

$$y(s) = y_0 + \frac{1}{\kappa}[\sin(\Phi_0 + h\ s\ \kappa\ \cos\lambda) - \sin\Phi_0] \tag{3.4}$$

$$z(s) = z_0 + s\ \sin\lambda \tag{3.5}$$

where here and in the following:

- s is the path length along the helix
- x_0, y_0, z_0 is the starting point at $s = s_0 = 0$
- λ is the dip angle
- κ is the curvature, i.e. $\kappa = 1/R$
- B is the z component of the homogeneous magnetic field ($B = (0, 0, B_z)$)
- q is charge of the particle in units of positron charge
- h is the sense of rotation of the projected helix in the xy-plane, i.e. $h = -\text{sign}(qB) = \pm 1$

- Φ_0 is the azimuth angle of the starting point (in cylindrical coordinates) with respect to the helix axis ($\Phi_0 = \Psi - h\pi/2$)
- Ψ is the $\arctan(\mathrm{d}y/\mathrm{d}x)_{s=0}$, i.e. the azimuthal angle of the track direction at the starting point.

The meaning of the different parameters is visualized in Fig. 3.3.

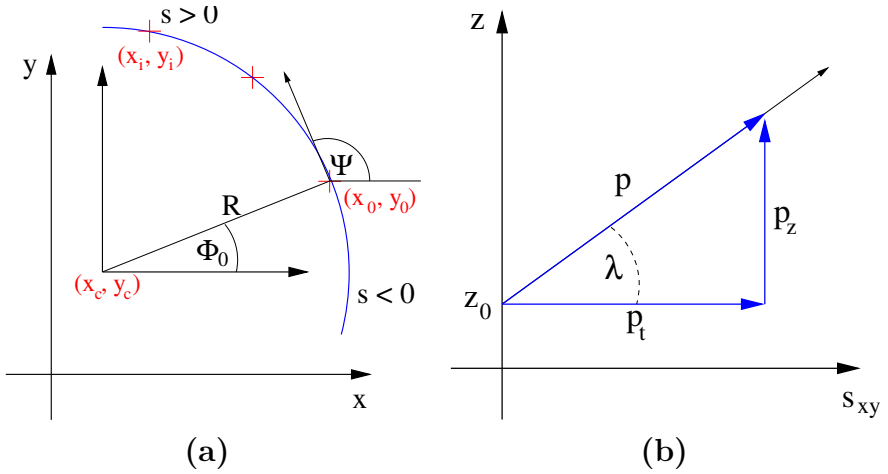

Figure 3.3: Projection of a helix on the (a) xy plane (b) $s_{xy} - z$ plane [37].

The TPT helix fit is actually performed in two separate stages. First a fit is performed in the transverse plane to establish the coordinates of the center of the circle (x_c, y_c) and the radius of the circle ($R = 1/\kappa$). The fit proceeds as follows. The distance between the set of points (x_i, y_i) is minimized relative to the circle $(x - x_c)^2 + (y - y_c)^2 = R^2$ by minimizing the functional

$$K(x_c, y_c, R) = \frac{M(x_c, y_c, R)}{R^2} = \sum_{i=1}^{n} \frac{\left(\frac{x_i^2+y_i^2}{R} - \frac{2x_c x_i}{R} - \frac{2y_c y_i}{R} + \frac{x_c^2+y_c^2-R^2}{R}\right)^2}{w_i}. \tag{3.6}$$

Next, a linear fit is performed in the s_{xy} *vs.* z plane yielding values for z_0 and $\tan\lambda$. The phase of the helix (see Fig. 3.3) is defined as follows:

$$\Phi_0 = \arctan\left(\frac{y_0 - y_c}{x_0 - x_c}\right) \tag{3.7}$$

The reference point (x_0, y_0) is then calculated as follows:

$$x_0 = x_c + \frac{\cos\Phi_0}{\kappa} \tag{3.8}$$

$$y_0 = y_c + \frac{\sin\Phi_0}{\kappa} \tag{3.9}$$

and the helix parameters can be evaluated as:

$$\Psi = \Phi_0 + h\pi/2 \tag{3.10}$$

$$p_\perp = c\ q\ B/\kappa \tag{3.11}$$

$$p_z = p_\perp \tan\lambda \tag{3.12}$$

$$p = \sqrt{p_\perp^2 + p_z^2} \tag{3.13}$$

where κ is the curvature in [m^{-1}], B the value of the magnetic field in [Tesla], c the speed of light in [m/ns] (≈ 0.3) and $p_\perp$ and p_z are the transverse and longitudinal momentum in [GeV/c].

3.2.3 Global Track Refit

The results of the TPT helix fit are stored for each track. These tracks are then stored in a track container which is used as the basis for the rest of the event reconstruction. These track parameters are used for extrapolation into the inner detector layers. It was envisioned that a global refit of each track (using information from all tracking detectors) would then be performed. Only the TPC was used for tracking during RunII reconstruction, so the global refit does not include any extra tracking information. However, the global refit is critical because it

- Corrects for momentum reconstruction biases caused by multiple scattering and energy loss (see Eqs. 2.5 and 2.6)
- Weights each space point by its relative measurement uncertainty
- Discards points from the fit that lie far from the best fit (outliers).

These criteria are fulfilled by application of a Kalman filter routine. The Kalman filter uses information about the particle trajectory, the space points and their errors,

as well as the material that the particle has traversed to make a complete and robust statistical treatment. Essentially, the covariance matrix is fully calculated along every step of the particle's trajectory.

The algorithm proceeds in three stages. First, an outside-in pass is performed for outlying hit rejection. Hits that are beyond 5σ from the helix parametrization are marked and not used in the refit. Next, an inside-out smoothing pass is performed. The smoothing pass makes corrections for average energy loss and multiple scattering. This process depends on an accurate calculation of the amount of material traversed, which is extracted from a GEANT[4] [38] propagation through the STAR detector model. Additionally, outlier removal is once again performed on the smoothing pass. Finally, a third pass is performed to determine the optimal track parameters at the inner most point on the track and to establish the χ^2 value for the Kalman fit. Further details of this procedure can be found in Reference [36]

3.2.4 Primary Vertex Finding

After the global refit, reconstruction proceeds to the primary vertex finding stage. This stage is performed by one of three algorithms, depending on the colliding beam species and the number of global tracks in the event. These three algorithms differ primarily in their treatment of outlier rejection and $p_\perp$ weighting, which will be discussed below. All vertex finding algorithms attempt to locate the position of the primary beam-beam interaction. This position generally has a much better position resolution than a typical TPC hit and is located a distance of $\sim$60 cm from the first TPC padrow. If included in the helix fit, the high precision and long lever arm provided by the vertex position greatly improve the momentum resolution of high-$p_\perp$ tracks. Additionally, requiring that tracks originate from the primary vertex provides a powerful tool for background suppression.

The primary vertex algorithm proceeds as follows:

1. Identify a seed position $\overrightarrow{x}_{seed}$.

[4]GEometry ANd Tracking

2. For each global track, use a helix projection to find the track location that minimizes the three dimensional distance between the helix and $\overrightarrow{x}_{seed}$. Define $d_i = |\overrightarrow{x}_{seed} - \overrightarrow{x}_{track}|$. For specifics on this calculation see Reference [37].

3. Minimize the summed distance $\chi^2 = \sum d_i$ by varying $\overrightarrow{x}_{seed}$.

4. Repeat steps 2 and 3 using the result of the minimization as the new location of $\overrightarrow{x}_{seed}$.

Inclusion of secondary tracks in the calculation of χ^2 can pull the minimization away from the true vertex position. Therefore, tracks with $d_i > \sim 5$ cm are removed from the calculation. This process is iterated until a stable solution ($\overrightarrow{x}_{vertex}$) is found.

Both the probability of finding a primary vertex and the position resolution of the vertex depend on the number and $p_\perp$ of the tracks used in the calculation. The trajectories of tracks with high-$p_\perp$ are less affected by multiple scattering, as shown in Eq. 2.6. The vertex finding efficiency increases with increasing N_{tracks}, saturating at 100% near N_{tracks}=50. In Au+Au collisions, the EVR[5] algorithm is used for events with N_{tracks} >30. Below that, the LMV[6] algorithm is used. In p+p collisions, a variant of LMV called ppLMV[7] is used. ppLMV requires that the seed be defined using only tracks that match to hit portions of the CTB. However, this requirement was relaxed in the final stages of iteration, making ppLMV more susceptible to background contamination than was originally realized. A major effort in this thesis analysis was to remove background contamination from p+p events reconstructed using ppLMV. This is further discussed in section 5.3.

3.2.5 Primary Track Refit

In a Au+Au event the primary vertex position has a typical resolution of 100-200 μm, which is much smaller than the typical resolution of a TPC point (∼700 μm). Therefore inclusion of the primary vertex results in a substantial improvement of the $p_\perp$ resolution. The primary track refit is described below, and the calculation and

[5]Default STAR Vertex Finder
[6]Low Multiplicity Vertex Finder
[7]Proton-Proton Low Multiplicity Vertex Finder

presentation of various acceptance, efficiency, and resolution factors are presented in section 3.4.

Each track is tested to determine if it originated from the primary vertex. This decision is based on calculating $|\overrightarrow{x}_{dca}| = |\overrightarrow{x}_{vertex} - \overrightarrow{x}_{track}|$ where x_{track} is the location of the track at the three dimensional distance of closest approach to the primary vertex. Tracks that satisfy $|\overrightarrow{x}_{dca}| <3$ cm are selected as primary tracks and refit using the primary vertex as the first point on the track. The primary refit is performed by a constrained Kalman fit that forces the track to originate from the primary vertex location. Additionally, the refit accounts for momentum bias due to energy loss and multiple scattering of the particle in the material between the interaction point and the first padrow of the TPC. For global tracks the momentum is reported at the first point of measurement ($r \simeq$60 cm). For primary tracks the momentum is reported at the location of the primary vertex ($r =$0 cm), thus the extra correction is necessary.

3.3 Acceptance and Efficiency Calculations

As the scope and complexity of particle physics detectors grows, a thorough understanding of the detector response is crucial to interpretation of all data. Specifically, one must understand and perform corrections to the data to account for potential sources of bias such as: finite detector acceptance, imperfect track finding efficiency, and finite momentum resolution, to name a few. This is done by appealing to a simulation of the detector description and response. The fundamental concept is based on feeding kinematically known data to a detector response simulator, feeding this simulated detector response to the event reconstruction software, and comparing the input with the final kinematic distributions which are output from the event reconstruction. If the detector response simulator is accurate, then this process allows one to quantify and decouple various inefficiencies and biases.

3.3.1 GEANT Detector Simulation

The first step is to simulate the passage of particles through the detector material. This is accomplished using the industry standard GEANT software package. GEANT is a highly refined library that models electromagnetic and nuclear interactions of particles with matter. The software works by loading a detailed three dimensional model of all material present in the STAR interaction region, including the beam pipe, SVT, TPC gas, magnet, support structure, etc. This complex representation is organized into a sorted structure that can be automatically navigated along an arbitrary trajectory. GEANT then provides tools to propagate a given particle type through the detector model, simulating multiple scattering, energy loss, conversion, and particle decay along each step of the trajectory. Thus, the final output of GEANT is a full simulation of what happens to a particle as it traverses the detector volume. From this information one extracts, e.g., the energy dE liberated at discrete points in the TPC gas. The development of a detailed detector model is a tremendous amount of work and is maintained by one or more full time members of the STAR collaboration. For more information on GEANT see Ref. [38]

3.3.2 TPC Response Simulation

A complex software package was developed to mimic the detector response to real data. Here we focus exclusively on the TRS[8] algorithm. The response simulator is tuned and debugged until various diagnostic distributions (e.g., the distribution of the number of hits on a track) are identical in both real and simulated data. TRS is based on an algorithm first developed in detail by the ALEPH collaboration, as described in Ref. [39]. The TRS package includes highly detailed calculations to simulate the drift, collection, amplification, and digitization of electrons created by particles that ionize the TPC gas. The list of electrons is output from the GEANT simulation. Here we give a brief overview of the workings of TRS. A more complete treatment can be found in Ref. [40]

The four basics steps of the TRS algorithm are:

[8]Time Projection Chamber Response Simulator

1. *Ionization Transport*- drifting of the ionization products (electrons) in the electric field from their knock-out point to the readout system.

2. *Charge collection*- collection of the ionization on the sense wires of the TPC MWPC.

3. *Analog Signal Generation*- charge induction on the pad plane and generation of the time dependent analog signal.

4. *Digital Signal Generation*- conversion of the analog signal into an ADC count.

The ionization transport package begins by transforming the energy loss of a charged particle dE (given by GEANT) into a discreet number of electrons. This transformation depends only on the ionization potential of the TPC gas. Next, the charge transporter evolves the characteristics of the charge cluster as they drift from the creation point to the TPC end cap, diffusing in both the transverse and longitudinal directions.

When the drifting electrons reach the readout plane, they are collected in the MWPC. This is where the primary signal amplification is performed via the avalanche process, multiplying the several tens of electrons to $10^3 - 10^5$, depending on the potential of the wires. This process is modelled by the charge collection routine, which implements the Yule-Furry process [31].

Next, the charge collected on the MWPC wires induces an image charge on the pad plane. The analog signal generation routine models this process by using the distribution of charge induced on a grounded pad plane, which is given by the *Gatti* function [40]. The *Gatti* function gives the charge density $\sigma(x, d)$ induced on the pad plane as a function of the location x on the plane and the distance d from the wire. The *Gatti* function is a slight deviation from a Gaussian distribution. To calculate the total charge induced on the pad plane, $\sigma(x, d)$ is integrated over the pad plane area. A simulation of the pad plane readout electronics is then performed to transform the induced charge into a time dependent analog signal. Finally, this analog signal is converted into an ADC value, completing the response simulation.

3.3.3 Embedding

It has been demonstrated that the aforementioned simulation chain is a realistic representation of the detector response to traversal of primary charged particles [40]. However, real data also consists of further background sources which can influence the reconstruction algorithm. Some potential background sources include: noise in the readout electronics, cosmic ray contamination, beam-gas background, and multiple interactions per readout event. To account for these background sources, an embedding scenario was employed. Real data events of various trigger conditions were mixed with pure simulation at the raw data level, and reconstruction was performed. The level at which the simulated tracks were reconstructed in the realistic background environment defines the real reconstruction efficiency. The embedding was performed for Au+Au and p+p data sets with trigger conditions ranging from central Au+Au collisions to zero-bias (randomly triggered) p+p collisions. A small number of Monte Carlo tracks were embedded into the real data by first running GEANT and TRS to simulate the digital signals of the detector. These digital signals were mixed with the signals from the real data stream and reconstructed. Finally, an association algorithm was performed to associate reconstructed tracks with the input Monte Carlo. This association was performed at the hit level. Below we show a small sample of the results obtained.

3.4 Acceptance, Efficiency, and Resolution

First we evaluate the track finding efficiency for primary tracks. This actually incorporates losses due to finite acceptance of the TPC and inefficiencies in the cluster finding algorithm, as well. The efficiency depends on the user-cuts, specific to an analysis, that a reconstructed track must pass to be accepted. Fig. 3.4a shows the efficiency as a function of $p_\perp$. The reconstructed particles were required to satisfy the following selection criteria: $24 < N_{points\ fit}$ and $|\eta| < 0.7$, and to come within 3 cm of the primary vertex. The efficiency is approximately constant for $p_\perp > 0.4$ GeV/c. This behavior holds in all multiplicity classes. For any multiplicity class, we

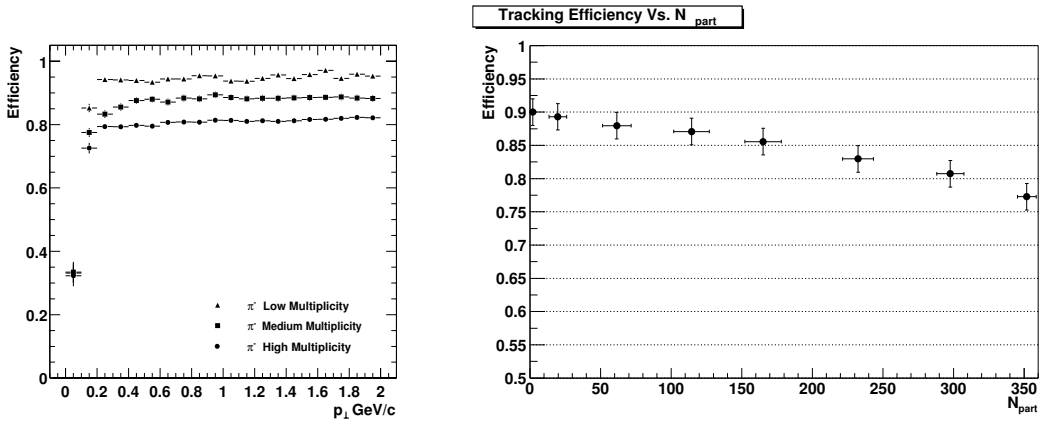

(a) **(b)**

Figure 3.4: Fractional track finding efficiency vs. (a) $p_\perp$ [32] and (b) the number of participating nucleons (N_{part}) for $\sqrt{s_{\rm NN}}$= 200 GeV p+p and Au+Au data. Inefficiencies from finite acceptance and imperfect cluster finding are included. The p+p data correspond to $N_{\rm part}$=2. See the text for single particle selection criteria.

can thus parameterize the efficiency as a constant for particles in this $p_\perp$ region. In Figure 3.4b we show the extracted asymptotic high-$p_\perp$ efficiency for different p+p and Au+Au collision multiplicities. We plot vs. the number of participating nucleons, $N_{\rm part}$, which is proportional to the charged particle multiplicity. For more specifics see App. E. For the p+p data $N_{\rm part}$=2. Even in the p+p data where the charged particle multiplicity is extremely low, the efficiency is only 90%. This represents the acceptance-driven upper limit of the STAR TPC. The remaining 10% can be accounted for by un-instrumented regions between sectors in the TPC.

The primary vertex resolution perpendicular to the beam axis (σ_v) can be determined as

$$\sigma^2(N_{tracks}) = \sigma_b^2 + \sigma_v^2 \tag{3.14}$$

where

$$\sigma_v = \frac{\sigma_{tracks}}{\sqrt{N_{tracks}}} \tag{3.15}$$

Here, $\sigma(N_{tracks})$ is the variance of the track impact parameters in x or y to the beam axis. As shown in Fig. 3.5a, the resolution vanishes for central events and the size of the beam spot is about $\sigma_b = 70\mu$m. Along the beam axis (z) it is not possible

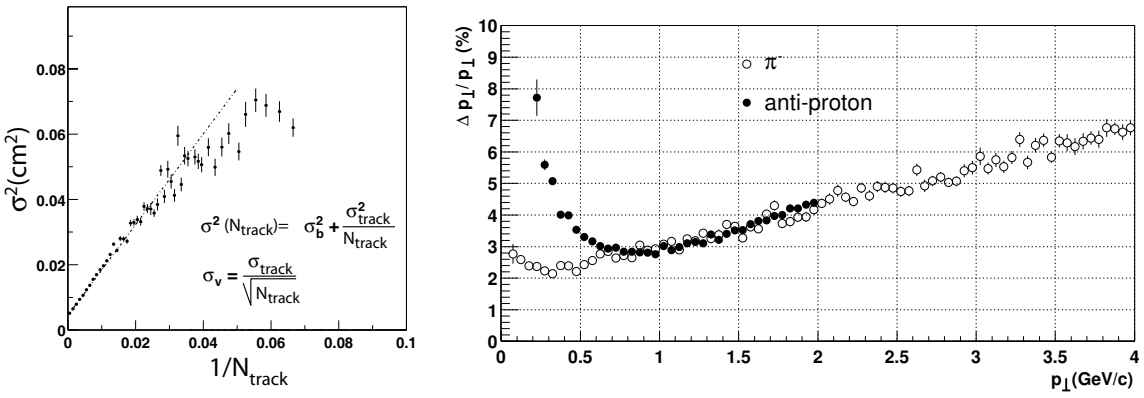

(a) **(b)**

Figure 3.5: (a) Evaluation of the transverse primary vertex resolution $\sigma_v = \sqrt{\sigma^2(N_{tracks} - \sigma_b^2)}$. (b) $p_\perp$ resolution vs $p_\perp$ for 0.25 T magnetic field setting [32]. The resolution is calculated as the sigma of a gaussian function.

to calculate the vertex resolution using this method because of the spread of the primary vertex location ($\sigma_z \approx 90$ cm). However, detailed simulations show that the primary vertex resolution along the beam axis (z) is of similar size as in the transverse direction. The embedding results further find the primary vertex finding efficiency to be 94±2%; 100% for events with more than 50 global tracks, but decreasing to about 60% for events with five or less tracks. Fig. 3.5b shows the transverse momentum resolution for primary tracks as a function of $p_\perp$. The resolution is determined by fitting a gaussian to the distribution $\frac{p_\perp^{Monte\ Carlo} - p_\perp^{reconstructed}}{p_\perp^{Monte\ Carlo}}$ and extracting the σ. The distribution is the sum of two competing effects. At low-$p_\perp$ ($p_\perp^{pion} < 0.4$ GeV/c), the resolution is dominated by multiple scattering, which is driven by the factor $\theta_0 \sim \frac{1}{\beta p}$ in Eq. 2.6. This effect is largest at low-$p_\perp$ and tends to zero in the high-$p_\perp$ limit. At higher $p_\perp$ ($p_\perp^{pion} > 0.4$ GeV/c) is dominated by both the position resolution of the TPC and the primary vertex resolution, yielding a linear rise with $p_\perp$. For the B=0.5 T setting the resolution improves by a factor of ∼3. For minimum-bias Au+Au data at $\sqrt{s_{NN}} = 200$ GeV, the resolution can be parameterized as $\delta p_\perp / p_\perp \simeq 0.007 + 0.004 \cdot p_\perp/(\mathrm{GeV}/c)$ for charged hadrons of $p_\perp > 1.5$ GeV/c.

Chapter 4

Jet Finding Algorithms

4.1 Introduction

The primary goal of this analysis is to study hard parton-parton scattering in "simple" (p+p) and "complex" (Au+Au) systems. Ideally, all measurements would be reported in terms of final state parton momenta p^{μ}_{parton}. However, bare partons have yet to be measured. Instead, only what is left after parton fragmentation into final state hadrons can be measured. A major advance of late twentieth century particle physics has been the rapid improvement of jet finding algorithms [41] [42] [43] . These algorithms cluster the fragmentation products to "reassemble" the momentum of the outgoing parent parton, allowing one to effectively "see" the bare partons.

In general, jet finding algorithms are composed of two parts:

- **Clustering Scheme**: Cluster final state particles that belong to the same jet.
- **Recombination Scheme**: Characterize the properties of the jet, specifically the four momentum (p^{μ}). Given a perfect detector, p^{μ} is identified with the four momentum of the parent parton.

Because the actual fragmentation process is complex and non-perturbative, the algorithm to cluster fragmentation products is challenging. The number, type, and momenta of daughter particles are not specified, so a reconstruction algorithm must be general enough to cope with these changing independent variables, but strict enough to keep from including excessive background particles coming from other physical processes in the same event (e.g., decay of the beam remnants, also called the underlying event). Further, it is not completely straightforward to specify precisely the number of jets and their respective energies in a particular event. This is largely due to the

fact that jet fragments are not infinitely well collimated and will often include remnants of soft gluons that were emitted at large angles. Even worse, partons can rejoin as well as divide. This, combined with quantum interference, implies that a given hadron can be a "decay product" of more than one parton [4]. Such complications have led some to conclude that a jet cross section is to some extent an artifact. If so, then the impetus is in simply providing a careful definition that is both well specified and CIS, as first suggested by Weinberg and Sterman [44]. Such an algorithm must then be applied to both experimental data and theoretical calculations.

These issues have motivated a 20 year effort to standardize jet reconstruction techniques, ultimately culminating in the findings of the Tevatron RunII jet physics working group [41]. Below we summarize the group's specification of the eight attributes of an ideal jet algorithm.

1. *Detector Independence*- The performance should not depend on where the data came from.

2. *Minimization of resolution smearing and angle biases*

3. *Insensitivity to background*- Jet finding should not depend on, e.g., the luminosity of the colliding beams.

4. *Efficient use of computer resources*

5. *Maximal reconstruction efficiency*

6. *Ease of calibration*

7. *Ease of use*

8. *Fully specified*- This includes specifications for algorithm flow, clustering, and recombination schemes.

In the following chapter we discuss the principles of jet finding algorithms. Specifics of the software implementation of the algorithms can be found in Appendix D.

4.1.1 Algorithm Classification

Jet finding algorithms come in two flavors: cone and k_T algorithms [42] [43]. Both algorithms look for final state particles that are close together in space, but they differ in algorithm flow. In general, cone algorithms have historically been applied more often at hadronic colliders, while k_T algorithms have been applied more at lepton colliders. This distinction is based on the fact that the k_T algorithm assigns all final state particles to a jet, while the cone algorithm does not. In e^+e^- collisions all particles should be assigned to a jet, while in hadronic collisions one is generally interested in the primary parton-parton interaction and wants to exclude particles from the underlying event. Both algorithms make use of a basic distance measure, R. In an unpolarized e^+e^- collision, there is no preferred symmetry axis, so one usually works in spherical coordinates. We can write the basic distance measure as

$$R = \sqrt{\Delta\theta^2 + \Delta\phi^2} \tag{4.1}$$

However, in hadronic collisions, one generally uses the pseudo-rapidity variable η to respect the symmetry along the beam direction. We can then write the metric as

$$R = \sqrt{\Delta\eta^2 + \Delta\phi^2} \tag{4.2}$$

where

$$\eta = -\ln\left(\tan\left(\frac{\theta}{2}\right)\right) \tag{4.3}$$

We call this measure the jet cone radius, and previous studies tell us that particles are generally contained within a radius $R < \sim 1$ with respect to the jet axis. Given a "seed" (first guess at the jet axis), we can group particles that lie within $R \approx 1$ unit from the jet axis. This is the basis of the cone algorithm.

The k_T algorithm is a nearest neighbor approach and thus does not require a seed. It uses a similar distance measure to cluster neighboring particles, but it manipulates the knowledge that fragmentation products also tend to have similar momentum magnitudes. Thus, the k_T algorithm uses a distance measure [42]

$$d_{ij} = \min(p_{T1}^2, p_{T2}^2)\frac{\Delta\eta^2 + \Delta\phi^2}{d_{cut}} \tag{4.4}$$

where d_{cut} is a number of order 1.

Once the clustering process is finished, one then proceeds to the recombination process. This process has changed with time, but it is now widely accepted that the most accurate method is to simply sum the four momenta of all final state particles that are clustered. We thus define

$$p^{\mu}_{jet} = \sum_{i=0}^{i=n} p^{\mu}_{i} \tag{4.5}$$

If the particles are sufficiently relativistic, we can take $m = 0$, giving $p^0 = |\overrightarrow{p}|$. Otherwise, we must take care to specify an approximate particle mass.

In the next sections, we discuss the cone and k_T algorithms in more detail.

4.2 Cone Algorithm

The cone algorithm began as a very simple algorithm, but its complexity has increased in parallel with the precision of both jet measurements and theoretical calculations. The current goal of 1% comparisons between theory and experiment at the Tevatron RunII has further refined the cone algorithm. The basis of the cone algorithm is to

1. Identify the approximate jet direction $\left(\frac{\overrightarrow{p}_{seed}}{|\overrightarrow{p}_{seed}|}\right)$ using high-momentum particles. We call this the jet seed.

2. Cluster particles that are within a radius of $R < R_{cone}$ given by equation 4.2. Typically a value of $R_{cone} = 0.7$ is used.

3. Calculate the centroid $(\overrightarrow{C})$ of the cone. $\overrightarrow{C}$ is defined as $\left(\frac{\overrightarrow{p}_{jet}}{|\overrightarrow{p}_{jet}|}\right)$ where $\overrightarrow{p}_{jet}$ is defined via equation 4.5.

4. Repeat these steps until $\overrightarrow{C}$ is the same as the seed direction $\left(\frac{\overrightarrow{p}_{seed}}{|\overrightarrow{p}_{seed}|}\right)$.

The problem lies in the definition of a jet seed. Generally one defines the seed as a track or calorimeter tower that is above a certain threshold E_{seed}. However, Figure 4.1 illustrates an example of collinear sensitivity of a seeded algorithm. Specifically,

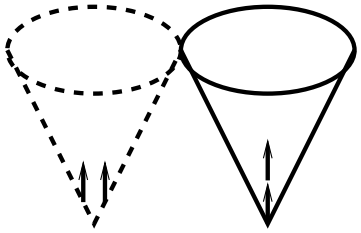

Figure 4.1: Collinear sensitivity. In the right frame, all of the energy is deposited in a single tower, bringing the tower energy above the E_{seed}. In the left frame, the energy is split between multiple towers, both of which have $E < E_{seed}$. Thus, the jet on the left will not be found. [41]

we see that a seed can be missed if the energy is deposited in two towers, both with energy $E_{tower;1,2} < E_{seed}$, instead of all of the energy being deposited in a single tower with $E_{tower;1} > E_{seed}$. Such a phenomenon can make the jet cross-section (in the region $E_{seed} < E_{jet} < 10 \cdot E_{seed}$) strongly dependent on the value of E_{seed}.

Figure 4.2 illustrates another artifact of E_{seed} sensitivity – artificial "spill out" of energy from the cone. These are but two examples where the jet energy is highly

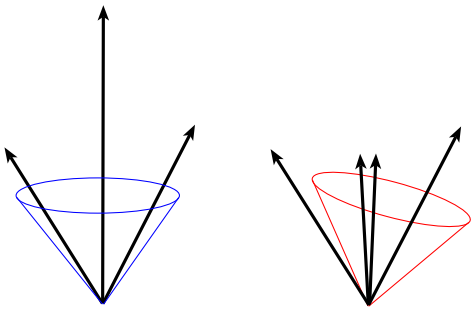

Figure 4.2: An example of artificial spill out. In the right plot, the energy of the middle particle has been split in two towers, the right-most particle was thus used as the seed, causing the artificial exclusion of the left-most particle. We call this phenomenon artificial spill out. [41]

sensitive to the choice of the cone seed. Many more examples exist. Clearly a cone algorithm must minimize sensitivity to seed choice in order to maximize efficiency and energy resolution while minimizing sensitivity to background, in accordance with the aforementioned requirements (2), (3), and (5). There are two possible remedies for this situation:

- **Seedless algorithm**: try all possible directions as seeds. This effectively removes any sensitivity to the choice of seed, but it can be computationally inefficient given the large data volume of most particle physics detectors.

- **Midpoint algorithm**: after finding all stable jets using a seeded cone algorithm, search for missed seeds by using the midpoint between all pairs of found jets as a seed. Often times this midpoint can yield a more stable solution.

4.2.1 Seedless Cone Algorithm

In the seedless algorithm, one uses every possible location (say, tower center) as a seed. Once a seed is chosen, the jet cone is iterated until it arrives at a location where the jet centroid is the same as the seed location. Thus, if there are n towers in a detector, there will be n jets per event. Many of these will be redundant in the case where cones converge on the same local minimum from different trajectories. Thus, one must untangle the n jets to arrive at a unique set of final state jets. This process is done via a jet splitting/merging algorithm that will be discussed in 4.2.3. We adopt the following language. Candidate jets (before splitting/merging) are called proto-jets, and final state jets are called simply jets.

Figure 4.3 illustrates the program flow of the seedless algorithm. Here we simplify the discussion by assuming that all information is coming from a list of calorimeter towers. In reality we use some combination of hadronic charged tracks and/or calorimeter data.

4.2.2 Midpoint Cone Algorithm

The midpoint algorithm was introduced as a way to use a seed based cone algorithm with a second step to search for missed seeds or artificially split jets. Once the clustering process finishes (producing a list of proto-jets) the "midpoint" process begins. Figure 4.4 illustrates the program flow for the midpoint algorithm. The process begins by generating an E_T ordered list of towers, then searching for stable cones around each tower with $E_T > E_{seed}$. Like the seedless algorithm, each "seed cone" is

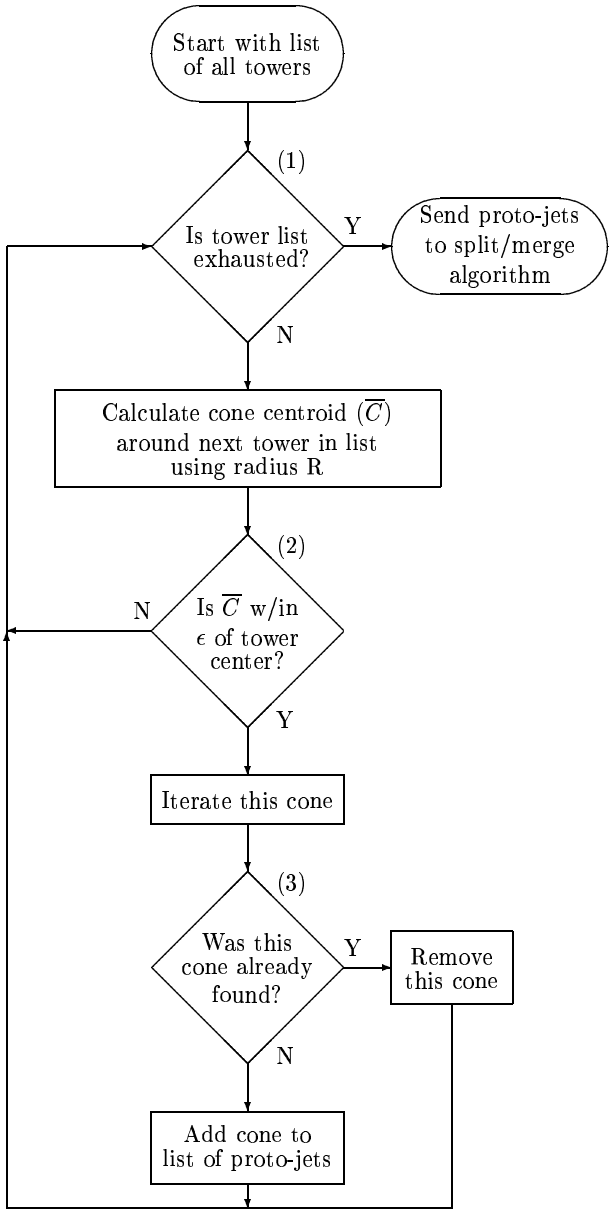

Figure 4.3: Program flow for an ideal seedless algorithm. [41]

iterated until the centroid is the same as the center of the seed tower. Further, all towers above threshold are used as seeds, not just those that are not yet assigned to a proto-jet. Thus, the proto-jet list can contain redundant and overlapping proto-jets. But, before the split/merge step begins, one generates another set of seed candidates.

All pairs of proto-jets are made, and a test seed is generated for any pair of proto-jets with a separation distance $d_{separation} < 2 \cdot R_{cone}$, where $d_{separation}$ is given by equation 4.2. The search algorithm then proceeds as usual, starting at each of the midpoint seeds and iterating each jet cone. Once all midpoint seeds are depleted, the algorithm finally moves to the split/merge step. The output of the split/merge algorithm is the final jet list.

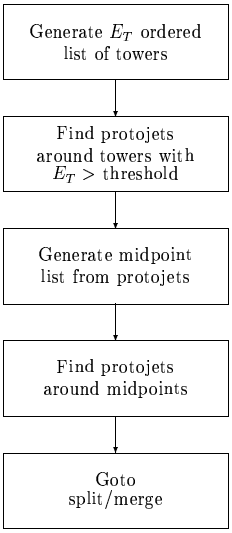

Figure 4.4: Program flow for a midpoint cone algorithm. [41]

4.2.3 Splitting/Merging Algorithm

The split/merge algorithm is used to disentangle proto-jets that share common towers. This is a complicated process, so it is imperative that the process be strictly defined. The basic concept of this algorithm is given below.

1. Find the highest E_T proto-jet. Call this the root.

2. Find all jets that share towers with the root proto-jet. Call these neighbor proto-jets.

3. Choose the highest E_T proto-jet from the set of neighbors.

4. Decide whether to split or merge these jets.

The criterion for splitting or merging a jet is given by the conditional

$$\frac{E_{T\ shared}}{E_{T\ neighbor}} > f_{split-merge} \tag{4.6}$$

where $f_{split-merge} \approx 0.5$. If this condition is satisfied, the two proto-jets are merged into a single proto-jet. Otherwise the two proto-jets are split such that each shared tower is assigned to the closest of the two proto-jets. Figure 4.5 illustrates the program flow of the split/merge algorithm. It is important to note that the split/merge step takes a list of proto-jets that are essentially circular (containing only towers satisfying $d < R_{cone}$), while the final state jet list contains jets that are no longer necessarily circular. That is, jets that result from the merging of two proto-jets generally take on an elliptical shape.

4.3 k_T Cluster Algorithm

The second class of jet algorithms is the QCD inspired k_T algorithm. It is essentially a "local" algorithm that manipulates a nearest neighbor approach. The strength of the k_T algorithm is that it does not depend on any choice of seed. Instead, pairs of towers are clustered until every tower in the event is assigned to a jet. The basis of the algorithm is to assign a "jettiness" measure to **both** pairs of proto-jets **and** single proto-jets themselves. For pairs of proto-jets i and j, we calculate d_{ij} via equation 4.4. For a single proto-jet i, we calculate

$$d_i = p_{T,i}^2 \tag{4.7}$$

Then the algorithm proceeds to either cluster nearest neighbors (if the minimum d is a d_{ij}) or to move a proto-jet to the jet list (if the minimum d is a d_i). The clustering of two proto-jets is defined by the regular recombination scheme of equation 4.5. Figure 4.6 illustrates the algorithm flow, and Figure 4.7 illustrates the time ordered clustering of a sample event. One can consider the particles to be either towers or partons. One can see that the low momentum particles that are close together are

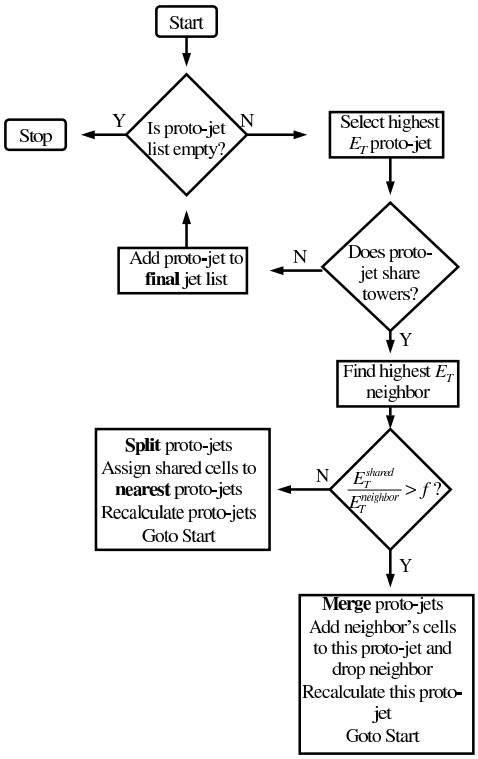

Figure 4.5: Program flow for the splitting/merging algorithm [41].

preferentially clustered. It is easy to see that this yields a CIS algorithm. A particle with an infinitesimal energy will not affect the final number of jets or their momenta, as it contributes infinitesimally to the momentum of the jet to which it is assigned. Similarly, if two particles i and j are nearly collinear ($p_i^\mu \approx \lambda p^\mu, \quad p_j^\mu \approx (1-\lambda)p^\mu$), then the first step of the algorithm is to combine them into one jet with momentum $\sim p^\mu$.

Perhaps the greatest advantage of the k_T algorithm is ease with which it can be applied at both the tower level (measured hadrons) and the parton level. Thus, the same tool can be used for a straightforward jet definition in both experiment and theory calculations. This is also true for the seedless and midpoint cone algorithms,

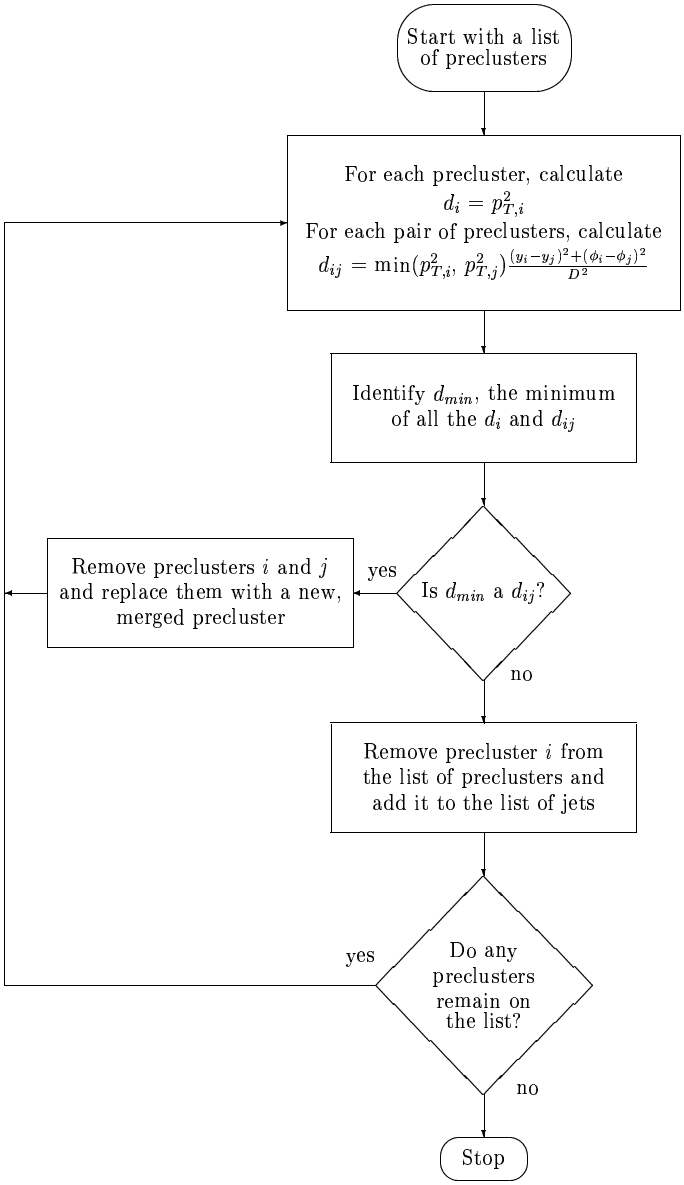

Figure 4.6: k_T cluster algorithm flow. Note that the algorithm does not depend on any choice of seed, and that all towers are assigned to a jet. [41]

but their respective implementations are significantly more complicated. The largest challenge in applying the k_T algorithm in a p+p collision is that the k_T algorithm is like a "vacuum cleaner" – it sucks up every particle in the vicinity of a jet. Thus, it

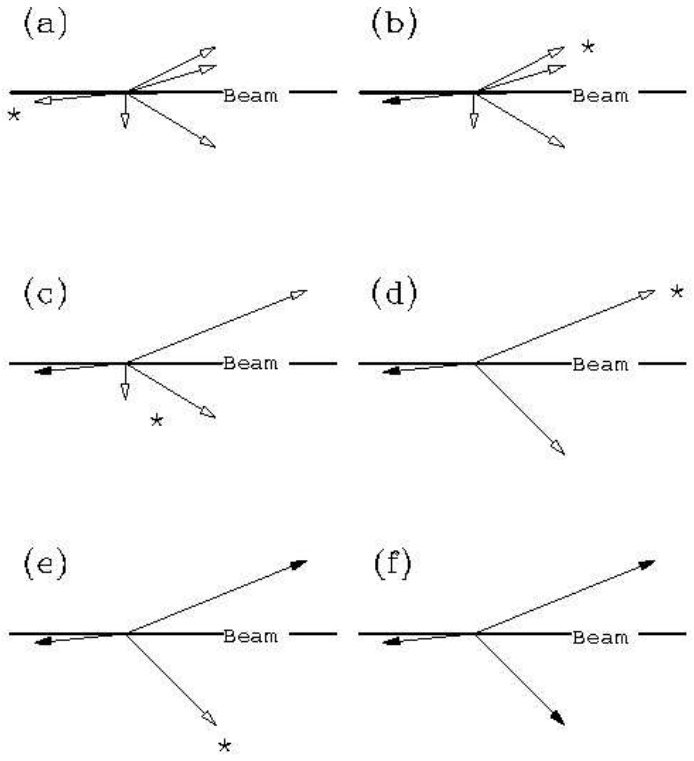

Figure 4.7: An example of k_T clustering in a sample event. Closed (open) triangles represent particles that are (are not) yet assigned to the final jet list. An asterisk (*) represents the location of the d_i or d_{ij} that is a minimum for a given step. Note that the algorithm preferentially clusters low momenta particles that are nearby in angle. [41]

is more sensitive to background contributions than a cone algorithm, and a thorough and challenging calibration of the jet energy scale is required.

Chapter 5

Data Reduction

5.1 Introduction

In this chapter we describe the specifics of the data reduction. The data used are from RHIC RunII which took place between the dates October 2001 and February 2002. The data were divided into three sets according to the beam and trigger combinations. The colliding beams consisted of both Au+Au and p+p at $\sqrt{s_{\rm NN}} = 200$ GeV. The Au+Au data set was taken in two different online triggering configurations

- **Minbias**: A minimum-bias configuration to maximize acceptance of inelastic Au+Au interactions at all impact parameters.
- **Central**: A configuration to accept the $\simeq$7% most central (smallest impact parameter) of the total inelastic Au+Au cross-section.

The p+p data set was taken in the following configuration:

- **ppMinbias**: A minimum-bias configuration to maximize acceptance of all non-singly diffractive inelastic p+p interactions.

These trigger conditions were defined in real-time data-taking by a logical combination of information from the fast trigger detectors: ZDC, CTB, and BBC, as defined in Sec. 2.3. Additionally, a signal from RHIC operations is available notifying of a filled bunch in both the blue (B) and yellow (Y) beams. Thus, bunch-bunch interactions satisfy the conditional (Y=1 and B=1). For the Au+Au run, additional timing information from the ZDC was available. Using the independent timing information from the east and west ZDCs, one can locate the approximate position of the collision along the beam direction. This allowed for selection of events that satisfied

Name	Y	B	ZDC	BBC	CTB	ZDC Timing
minbias	1	1	10<x		75<x	1
central	1	1	10<x<85		33000<x	1
ppMinbias	1	1		1		1

Table 5.1: Threshold values for trigger conditions used in this analysis. The CTB values are listed in units of ADC, where 5 ADC = 1 MIP. The ZDC values are listed in units of summed E+W ADC. For reference, the attenuated ADC value from a single neutron was ∼5 ADC. Information that was not used in a given trigger configuration is left as blank.

$|Z_{vertex}| < 30$ cm. This information was not used in the p+p run, as p+p data uses a coincidence in the BBC instead of the ZDC. The thresholds used in these trigger

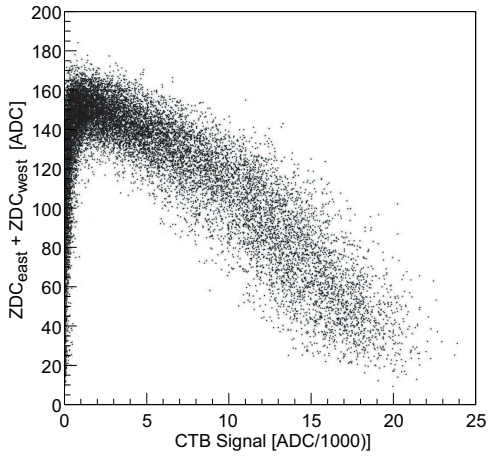

Figure 5.1: Summed ZDC vs. CTB distribution for Au+Au collisions. The lower left corner corresponds to peripheral collisions where a small amount of energy is deposited both at beam-rapidity and mid-rapidity. The lower right corner corresponds to central collisions where a small amount of energy is deposited at beam-rapidity, but a large amount of energy is deposited at mid-rapidity.

configurations are listed in Table 5.1.

5.2 General Data Distributions

Before we begin a complex analysis of jet studies in real data, we must first address the general characteristics of both the events and the single particle distributions.

Specifically, we will concentrate on general distributions that can be used as selection criteria for data quality. Here the purpose is to remove data coming from background sources, be they physical or detector specific, without cutting too deeply into the physics signal we wish to study. We first address general event characteristics. We then address single particle distributions.

5.3 General Event Characteristics

This analysis depends primarily on charged track information from the TPC. In Figures 5.2 we show the primary charged particle multiplicity in the region $|\Delta\eta| < 0.5$ for Au+Au and p+p systems. Note that typical multiplicities for Au+Au collisions

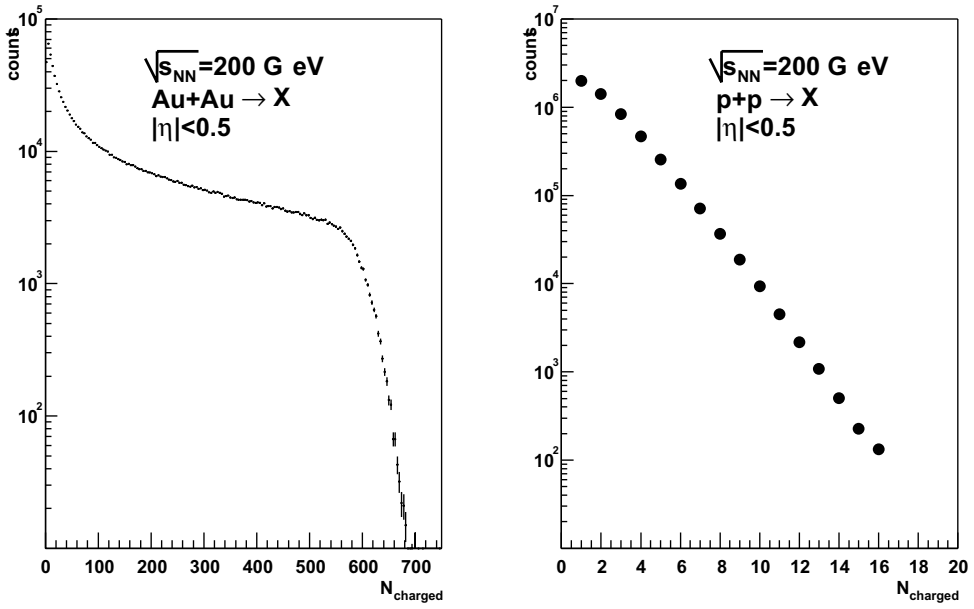

Figure 5.2: Primary charged particle multiplicity in minimum-bias Au+Au and p+p collisions at $\sqrt{s_{\rm NN}} = 200$ GeV. The data are uncorrected and the error bars are statistical only.

are in the range of 50-700, while p+p collisions typically produce much less than 5 charged particles. As stated in the previous chapter, the vertex finding software is optimized for high multiplicity events. One of the challenges of this analysis was applying such software to the low multiplicity, high background environment of p+p

collisions at RHIC. This becomes an issue when (i) the background sources (such as beam-gas collisions) are large compared to the rate of beam-beam interactions or (ii) the signal (high-$p_\perp$ jet production) is rare, but on the same level as the background sources (such as cosmic rays).

The p+p data used in this analysis relies on charged tracks that were associated with the primary vertex as defined by the ppLMV software package. However, ppLMV was run in a configuration that made it especially susceptible to the aforementioned background contamination. Thus, tools were developed to evaluate, event by event, the quality of the primary vertex. Events where the quality was deemed to be low were discarded from analysis. The discarded events were classified as being due to three sources of error: out-of-time trigger information, multiple beam-beam interactions (pile-up), and cosmic ray contamination. We describe these sources and the tools used to remove them from the event sample below.

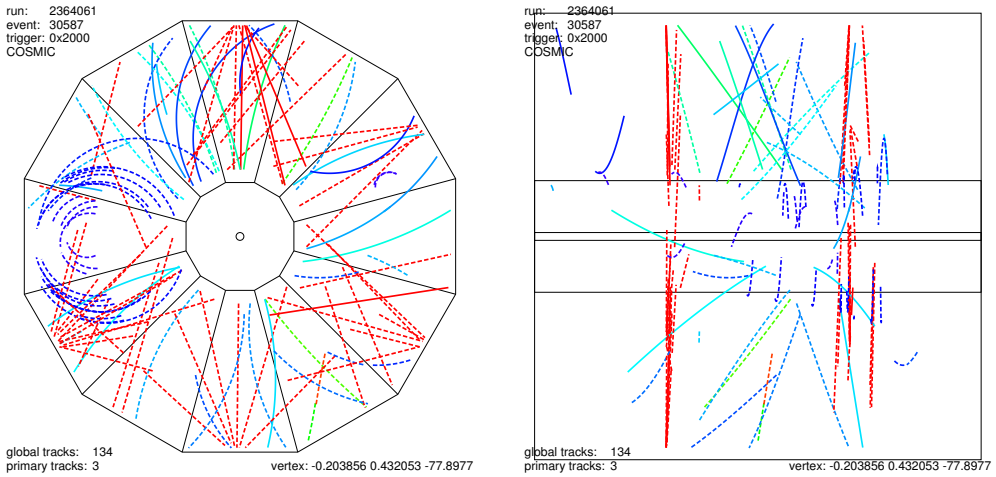

(a) **(b)**

Figure 5.3: (a) end view and (b) side view of an out of time triggered p+p event containing the remnants of a laser event. The solid (dashed) lines point to hit (not hit) CTB tiles. The left and right hand sides of (b) correspond to z values of -200 and +200 cm, respectively. The value of z_{vertex} as found by ppLMV is listed in the lower right of (b).

First, several runs had anomalous triggering information. The start time of the TPC readout was therefore ill-defined, making the z-position of hits unknown. A

typical example of such an event is shown in Figure 5.3 where a laser calibration event is mixed with a real p+p interaction in the same event. The laser tracks, being straight, are reconstructed to have a large $p_\perp$ and are weighted significantly in the reconstruction of the primary vertex, drawing the location of the primary vertex away from the p+p interaction point to the location of a laser crossing. These events were rejected by the back-to-back topology and high-$p_\perp$ of the reconstructed tracks that were associated with the laser positions.

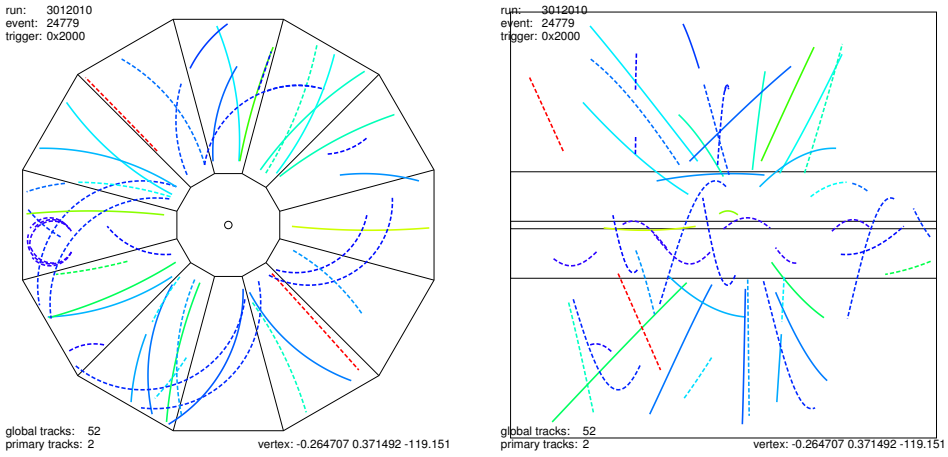

(a) **(b)**

Figure 5.4: (a) end view and (b) side view of an out of time cosmic ray in coincidence with a p+p interaction. The cosmic is reconstructed as the two red tracks best visible on the left hand side of (b). While the primary p+p interaction clearly happened in the center of the TPC, the location of the primary vertex was reconstructed to be precisely where the cosmic ray intersected the beam line.

Second, cosmic rays that were out of time with the triggered event also biased the location of z_{vertex} as found by ppLMV. As with laser tracks, a high-$p_\perp$ cosmic track carries more weight than many low $p_\perp$ tracks from an actual p+p collision. Thus, a cosmic ray that happens to intersect the approximate location of the beam-line usually defines the location of the primary vertex. An example of a cosmic event is shown in Figure 5.4. If a cosmic intersects the beam line it gets reconstructed as two tracks which appear almost exactly back-to-back and can be rejected by cutting on the three dimensional opening angle between two tracks.

Events with multiple interactions, such as that shown in Figure 5.5, are more challenging to analyze. The probability for multiple interactions in a single bunch crossing varied from ∼0.1% at low luminosity to ∼0.4% at peak luminosity [45]. Coupled with a 40 μs drift time of the TPC, this yielded an average of ∼0.5-1.5 pile-up events per TPC readout, at low and high luminosity, respectively. These events

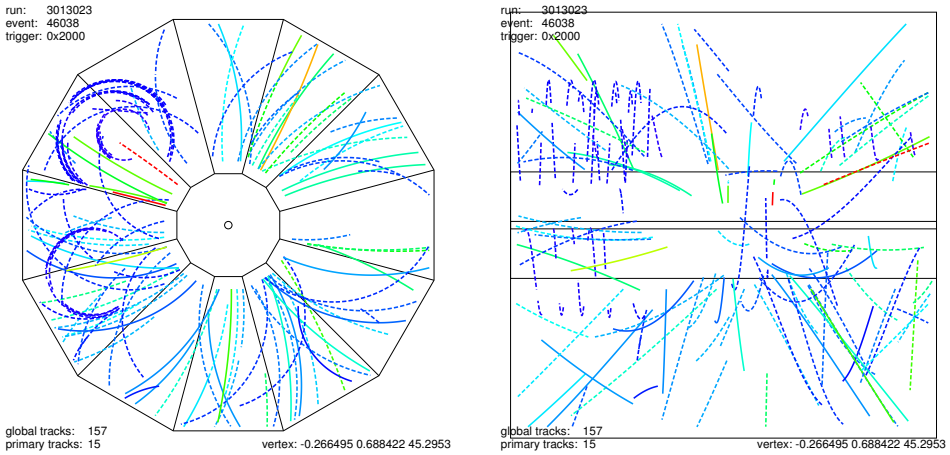

(a) **(b)**

Figure 5.5: (a) end view and (b) side view of multiple interaction pile-up in p+p data. The vertex was reconstructed at $z_{\text{vertex}} = 50$ cm instead of $z_{\text{vertex}} = 5$ cm, which is clearly the primary interaction.

do not have to be a priori rejected, but it is imperative that tracks belonging to the reconstructed ppLMV primary vertex have valid timing information. In principle this can be achieved by requiring that each track points to a hit CTB tile. However, pile-up events tend to have large multiplicities, causing the CTB's poor granularity to be a limiting factor. It was found that the CTB information is necessary but not sufficient to reject pile-up interactions. Therefore an independent post-production vertexing method was developed, called the Hough vertex finder.

The Hough vertex finder (HVF) uses a voting algorithm to independently determine the z-position of vertices in an event that originate from the beam-line. The algorithm works as follows:

- In two dimensions, project all global tracks to the distance of closest approach (dca) to the beam-line. Histogram the z position of the track at this point.

- Search for peaks in this histogram between ± 200 cm. A peak was defined as having more than two counts in a 5 cm window.
- Collect all of the tracks that voted for this peak into a common collection. Call these the daughters of this vertex. These are referred to as HVF vertices.
- Repeat this procedure using only global tracks that project to a hit CTB tile. These are referred to as CTB Hough vertex finder (CHVF) vertices.

Thus, the result is two lists of vertices, one requiring that tracks match the CTB (CHVF), and one without this requirement. Pile-up events characteristically had approximately two to three HVF vertices. The quality of the ppLMV vertex was established by comparing to those returned by CHVF.

In Figure 5.6 the z position of the CHVF vertex with the most tracks ($z_{vertex}^{best\ CHVF}$) was compared to the z position of the primary vertex found by ppLMV (z_{vertex}^{ppLMV}). One can see a clear correlation along the diagonal, as well as an uncorrelated circular

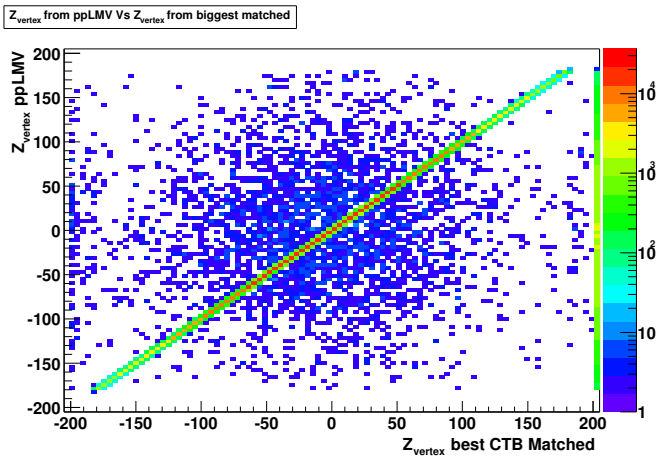

Figure 5.6: Event-by-event comparison of Z_{vertex} position from ppLmv and CHVF. Dimensions are in [cm].

background. Figure 5.7 shows the distribution of $z_\Delta = z_{vertex}^{ppLMV} - z_{vertex}^{best\ CHVF}$. A clear peak is seen for $|z_\Delta|$ <5 cm. Thus, events with $|z_\Delta|$ >5 cm were rejected from analysis. An example of such an event is shown in Figure 5.5. The largest in-time interaction is centered at $z_{\rm vertex} = 5$ cm. However, $z_{vertex}^{ppLMV} = 45$ cm, due to a single short track

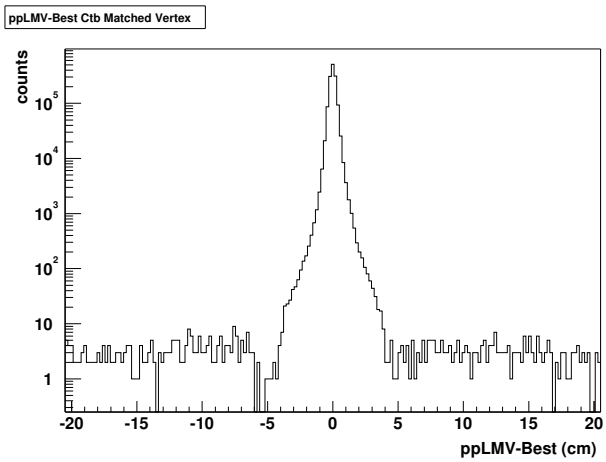

Figure 5.7: Event-by-event distribution of Z_{vertex} positions from ppLmv minus that from CHVF.

at high-$p_\perp$. This discrepancy is illustrated in Figure 5.8 which shows the result of the CHVF for this event. The vertex reported by ppLMV consists primarily of tracks

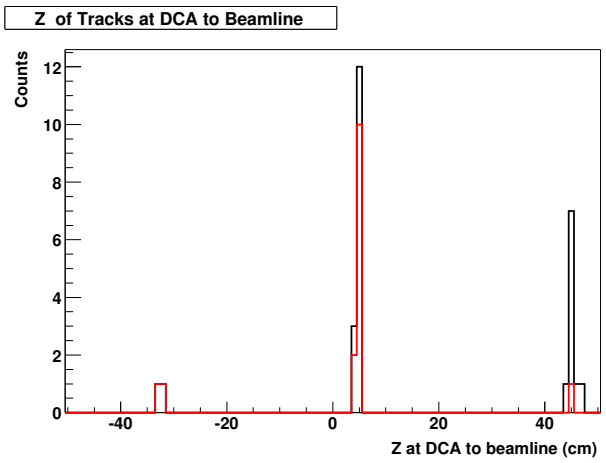

Figure 5.8: Single event distribution of z value of track at DCA to beamline, taken from the event in Figure 5.5. The histogram in red (black) uses tracks that are (are not) matched to the CTB. The peak at z=45 cm consists primarily of out of time tracks.

that do not match to hit CTB tiles and and cannot be used for analysis. A summary of the number of events rejected due to different background sources is given in Table 5.2.

Topology	$N_{rejected}$	Fraction
cosmic	806	0.5%
laser	80	0.05%
No HCtb Vertex Found	$5{\cdot}10^3$	0.6%
ppLmv $\neq$ HCtb	$9.2{\cdot}10^4$	6%

Table 5.2: Fraction of events rejected (from a sub-sample of 1.5M jet events) due to cosmic, laser, and vertex finding cuts.

Finally, lack of timing information at the trigger level resulted in $z_{\rm vertex}$ from valid p+p collisions being widely distributed, as shown in Figure 5.9. To maintain uniform

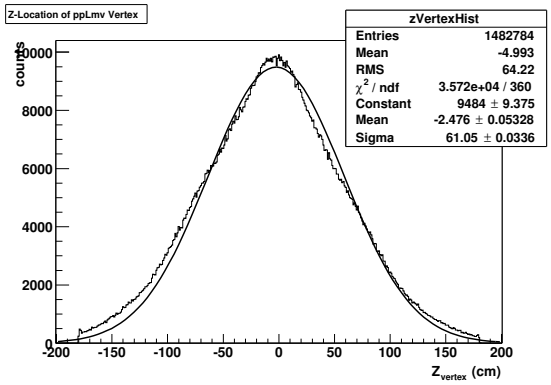

Figure 5.9: The distribution of $z_{\rm vertex}$ determined by ppLMV for p+p interactions. The distribution is approximately characterized by a gaussian function with a sigma of 61 cm. The selection $|z_{vertex}| < 70$ cm rejects only ≈25% of the p+p events.

efficiency as a function of η, only events with $|z_{vertex}|$ <70 cm were analyzed.

Chapter 6

Data Analysis and Results

6.1 Introduction

In this chapter we first present the results of charged particle jet measurements in p+p collisions. The general properties of these jets and the events from which they arise are studied as a function of jet $p_\perp$ in the range $p_\perp^{jet}$ <15 GeV/c. Where possible, we compare with a similar analysis from the CDF[1] collaboration at FNAL. We then study the energy and angular relationship between the jet and its LCP[2]. This motivates the kinematic selections used for the di-hadron correlation analysis which is then applied to the p+p and Au+Au data. Finally, the fate of back-to-back jets in central Au+Au collisions is presented.

6.2 General Jet Properties in $p + p \rightarrow Jet + X$

We first establish the general characteristics of charged particle jets. We stress the fact that the lack of a commissioned calorimeter prevented the measurement of neutral hadrons. The future availability of the BEMC and EEMC[3] will largely remedy this situation by measuring neutral hadrons that interact electromagnetically, primarily π^0 mesons, which take a substantial fraction of the jet energy. In the remainder of this chapter, we use the phrase "jet" to refer to clusters of *charged* hadrons. No correction for the undetected neutral energy was applied to the data, as such a correction is non-trivial for $p_\perp^{jet} < 10$ GeV/c.

Jets were identified using three algorithms:

[1]Collider Detector at Fermilab
[2]Leading Charged Particle
[3]Endcap Electromagnetic Calorimeter

- Iterative midpoint cone algorithm with splitting/merging (see 4.2.2) and implemented via the `StConeJetFinder` software (see D) with $R_{cone} < 0.7$, $E_T^{seed} = 1$ GeV, $f_{split/merge} = 0.5$. Referred to as MkConeJets_d5 (or simply cone) in the following.

- k_T Cluster algorithm implemented via the `StKtCluJetFinder` software (see D) with $d_{cut} = 1$ which corresponds to a cone radius of $R_{cone} \approx 0.7$. Referred to as MkKtJets (or simply k_T) in the following.

- Non-iterative cone algorithm without midpoints or splitting/merging. Designed to mirror the algorithm used in a recent CDF study of charged particle jets[46]. Additionally, it is particulary suited for future application in high multiplicity environments (d+Au and Au+Au collisions). Implemented via the `StCdfChargedConeJetFinder` (see D) with $R_{cone} = 0.7$, E_T^{seed}=1 GeV. Referred to as `StCdfChargedConeJetFinder` (or CdfChargeCone) in the following.

While three algorithms were applied to the data, the majority of the calibration effort was invested in the cone algorithm. The k_T algorithm would require an extensive energy calibration that was deemed impractical without the data from the BEMC. The `CdfChargedConeJetFinder` algorithm (which is not actually infrared safe at the parton level) was found to be biased towards finding jets that fragment hard. Differences between the algorithms do decrease with increasing jet $p_\perp$ (the events grow "jettier"), but can be significant for $p_\perp < 10$ GeV/c. We therefore draw our physics conclusions primarily from the cone algorithm, but results for all algorithms are provided for reference.

The following results were obtained using events with $|Z_{vertex}|$ <50 cm that passed the selection criteria summarized in Table 5.2. Primary tracks reconstructed in the TPC were required to satisfy the criteria listed in 6.1. These cuts were chosen to maximize not only the data cleanliness but also a maximal kinematic acceptance.

Fig. 6.1a shows a typical di-jet event in 2-d position space. The color coding reflects the $p_\perp$ of the charged particles. Fig 6.1b shows a 2-d momentum space representation of the same event. Two jets of $p_\perp \approx 7$ GeV/c, $\eta \approx 0$, and separated by $\Delta\phi \approx \phi$ were found in the event. The di-jet topology is much clearer in momentum

Selection	Motivation
$p_\perp$ >0.2 GeV/c	reject tracks that spiral within the TPC
$\|\eta\|$ <1	require uniform single track efficiency
$\|dca_{track-to-beamline}\|$ <2 cm	minimize background tracks
N_{fit} >15	assure a good helix fit balanced by a wide η acceptance.
$\frac{N_{points\ fit}}{N_{points\ possible}}$ >0.55	reject tracks that are artificially reconstructed as two tracks (split tracks)

Table 6.1: Single track selection used for p+p jet analysis.

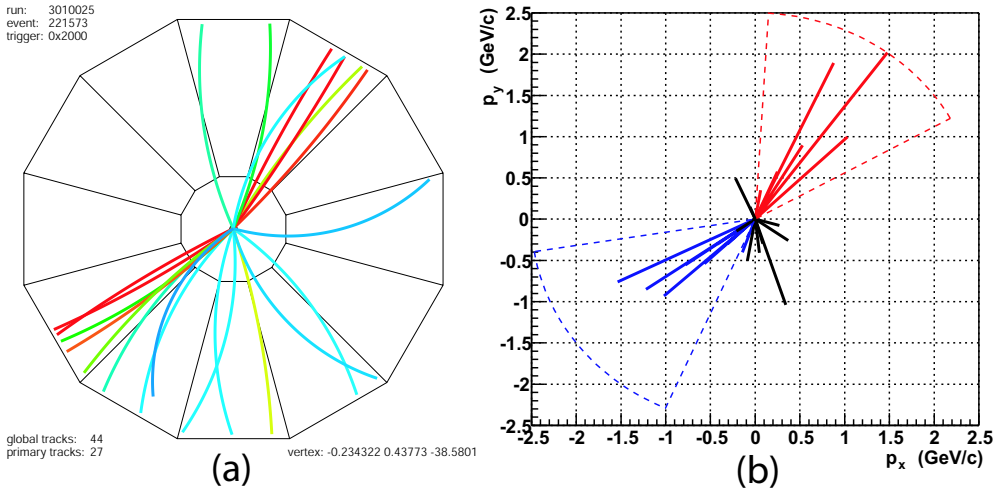

Figure 6.1: Example of a typical $p + p \rightarrow$ di-jet event yielding two jets of $p_\perp \approx$7 GeV/c. (a) y vs. x plot and (b) p_y vs. p_x plot of tracks satisfying analysis cuts. The color coding in the left panel reflects the $p_\perp$ of the particles. The color coding in the right panel reflects the assignment of particles to jets. The dashed lines represent the identified jet cones. The di-jet topology is more apparent when viewed in momentum space.

space, where the dashed arcs represent the approximate jet cone for the two identified jets and the color coding reflects the assignment of particles to jets. Particles that appear to be within a jet cone but not assigned to the jet are actually at significantly different values of η.

We first examine the fragmentation properties of jets by measuring the charged particle multiplicity (n_{ch}) per jet. We expect to find that n_{ch} increases with increasing jet $p_\perp$. We define jet_1 to be the leading (highest $p_\perp$) jet in the event. In Fig. 6.2

we show the distribution of n_{ch} within jet_1 for $5 < p_{\perp}^{jet_1} < 15$ GeV/c as found by the three algorithms. The distribution approximately follows a skewed gaussian, and ap-

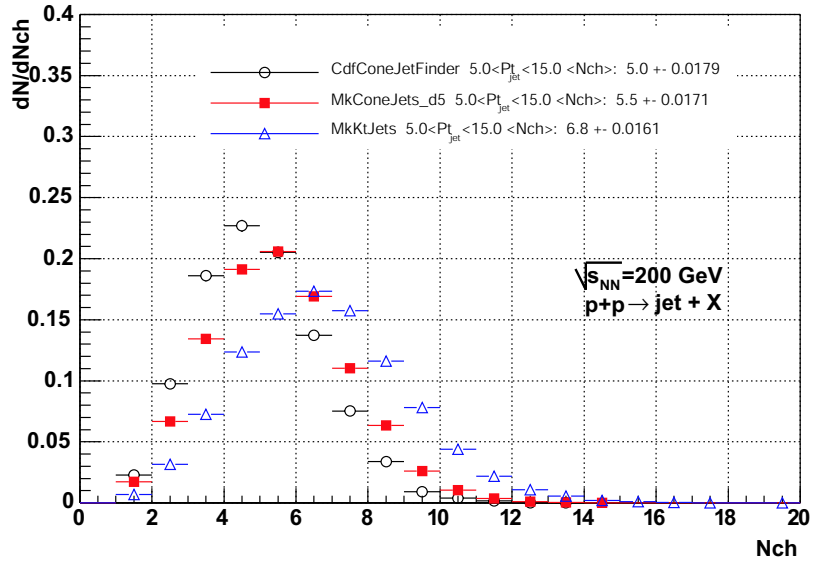

Figure 6.2: Number of charged particles in jet_1 with $5 < p_{\perp}^{jet_1} < 15$ GeV/c. The integral of the distribution is normalized to unity. The arithmetic mean is shown in the legend. Statistical error bars are shown.

proaches the gaussian limit with increasing n_{ch}, as expected. We quantify the centroid of the distribution by calculating the arithmetic mean $\langle n_{ch} \rangle$. Fig. 6.3 shows $\langle n_{ch} \rangle$ vs. $p_{\perp}$ of the leading jet ($p_{\perp}^{jet\ 1}$). In general, the k_T algorithm has the highest value of $\langle n_{ch} \rangle$ per jet, the `CdfChargedConeJetFinder` algorithm has the lowest, and the cone algorithm is in between. Using the cone algorithm as a reference, the k_T algorithm finds on average ≈1.8 additional charged particles per jet. These particles are primarily at low $p_{\perp}$ and distributed on the periphery of the jet cone. For comparison, Fig. 6.3 also shows the results of a CDF study using the analog of (and inspiration for) the `CdfChargedConeJetFinder` algorithm. The CDF data are for $p_{\perp} > 0.5$ GeV/c, where we have used $p_{\perp} > 0.2$ GeV/c. Using the accompanying CDF charged hadron $p_{\perp}$ distribution, this corresponds to one extra charged particle accepted in the STAR analysis. We thus plot $\langle n_{ch} \rangle$+1 for the CDF measurements. While the CDF data ($\sqrt{s} = 1.8$ TeV) are at a much lower value of $x_{bjorken} \approx 2p_{\perp}/\sqrt{s} \simeq 5 \cdot 10^{-4}$ than the STAR data ($x_{bjorken} \approx 5 \cdot 10^{-2}$), there is quantitative agreement over the entire

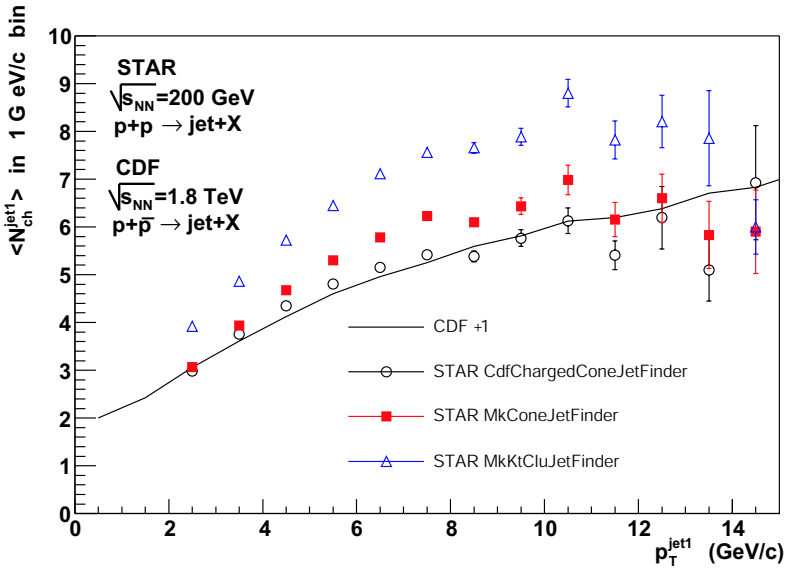

Figure 6.3: $\langle n_{charge}^{jet_1} \rangle$ vs. $p_\perp^{jet_1}$ Also shown are results from CDF (solid curve) [46]. Statistical error bars are shown.

$p_\perp$ region. Both the STAR and CDF distributions follow the expected trend of a rise for $p_\perp$ <8 GeV/c and suggests the onset of a logarithmic rise for $p_\perp$ >8 GeV/c, as predicted by fragmentation models [47].

We next examine the $p_\perp$ distribution of particles in the leading jet. We define $\Delta R \equiv \sqrt{(\phi_{jet} - \phi_{hadron})^2 + (\eta_{jet} - \eta_{hadron})^2}$ and study the scalar sum $p_\perp$ ($p_\perp^{sum} \equiv \sum_i^{n_{ch}} p_\perp^i$) as a function of ΔR, as shown in Fig. 6.4 for the CdfChargeCone algorithm at three different values of jet $p_\perp$. Fig. 6.4 includes a comparison to CDF data at the one overlapping $p_\perp$ value (5 GeV/c). The CDF data are not corrected for the aforementioned difference in kinematic selection, as it was found to make a negligible difference in the continuous variable $p_\perp^{sum}$. The peak for $\Delta R < 0.3$ is indicative of the "hot core" of charged jets, and the sharpness of the peak increases with jet $p_\perp$. The deviation between measured STAR and CDF data at $\Delta R > \sim 0.45$ is understood in subtle differences in the jet algorithms. We can quantify the jet "size" by calculating $\Delta R_{80\%}$ defined via

$$\frac{\int_0^{\Delta R_{80\%}} p_\perp^{sum} dR}{\int_0^{R_{cone}} p_\perp^{sum} dR} = 80\% \tag{6.1}$$

For jet $p_\perp$ of 2.5, 5.0, and 8.0 GeV/c we find $\Delta R_{80\%}$ to be 0.39±0.02, 0.37±0.02,

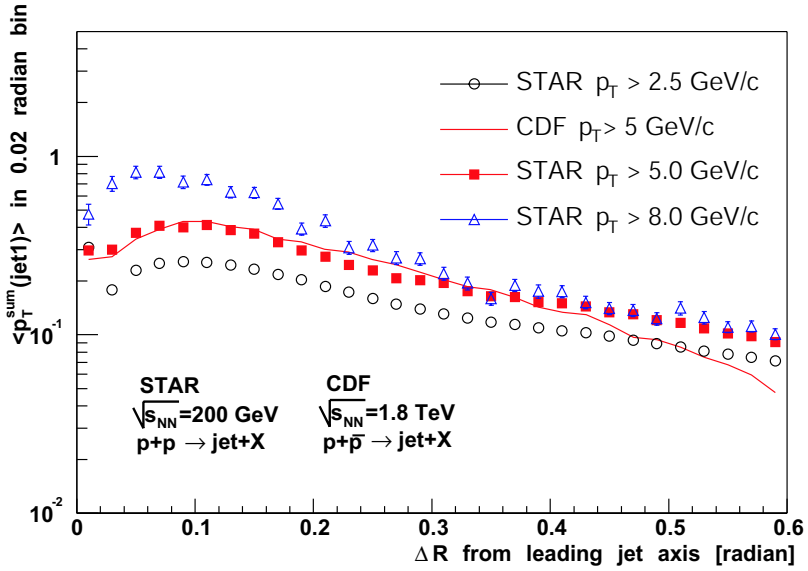

Figure 6.4: $p_\perp^{sum}$ vs. ΔR from axis of leading jet. Statistical error bars are shown. The solid curve corresponds to CDF data [46].

and 0.31±0.02, respectively. For comparison, CDF quotes $\Delta R_{80\%}$ =0.36 at 5 GeV/c. Thus, ∼80% of the jet $p_\perp$ is confined in the region $\Delta R \leq \ \sim R_{cone}/2$.

We next examine the transverse momentum distribution inside of the charged particle jet. We define

$$z \equiv \frac{p_\perp^{hadron\ i}}{p_\perp^{jet}},\ z:\ [0,1],\ \sum_{i=1}^{i=n_{ch}} z_i = 1 \tag{6.2}$$

Thus, z is a measure of the fraction of the jet-$p_\perp$ carried by hadron i. If all neutral energy was included in the definition of the jet (via calorimetry), this would be analogous to the definition of the transverse fragmentation function (the choice of $p_\perp$ instead of p will be further motivated in section 6.4). Figure 6.5a shows the distribution dN/dz for jets satisfying $5 < p_\perp < 15$ GeV/c as measured using three algorithms. The data show the qualitative features expected of a fragmentation function (see Fig. 1.3), namely an approximate exponential fall-off for $0.2 < z < 0.7$ and steeper fall off at high-z. The sharp rise at small z is an experimental bias caused by the lower $p_\perp$ cutoff of the STAR acceptance. The k_T algorithm has the steepest slope while the `CdfChargedConeJetFinder` algorithm has the flattest slope, with the

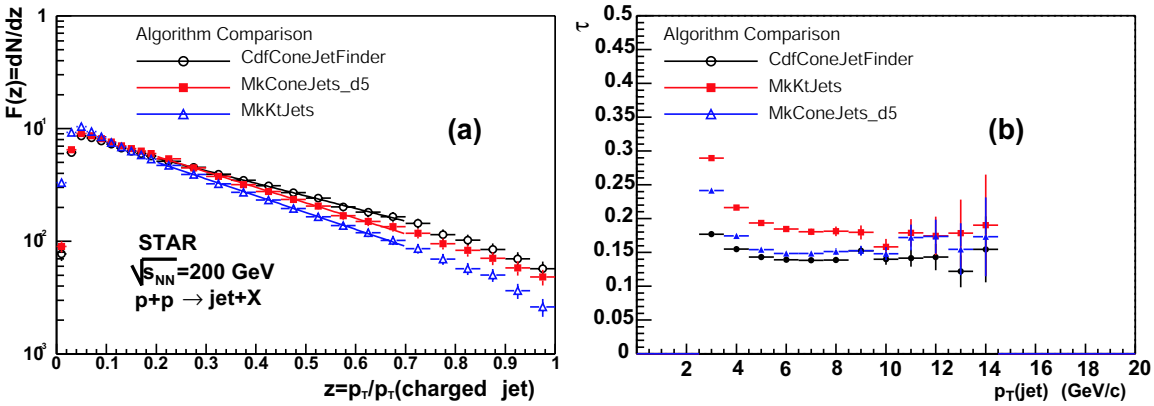

Figure 6.5: $p_\perp$ distribution of charged particles within the leading jet $5 < p_\perp^{jet} < 15$ GeV/c for three algorithms. The data are normalized to unity and statistical error bars are shown.

cone algorithm lying in the middle. This agrees with expectations drawn from the study of $\langle n_{ch} \rangle$, where the k_T algorithm clearly showed the highest values of $\langle n_{ch} \rangle$, thus slightly increasing the value of the jet-$p_\perp$reported by the k_T algorithm. In order to directly compare the slope of dN/dz found by different algorithms, an absolute jet energy calibration must be performed, which was not performed. However, the absolute slope of the distribution is not critical for this study. Fig. 6.5b shows the results of fitting the dN/dz distribution with a function of the form $N_0 \cdot e^{-z/\tau}$ in the region $0.2 < z < 0.7$, where τ is the inverse slope of the distribution. In this limited region of jet $p_\perp$ (and thus q^2), we find approximate scaling of the FF slope with jet-$p_\perp$ for $4 < p_\perp < 15$ GeV/c.

6.3 General Properties of $p + p \rightarrow Jet + X$ events

We next study the general properties of events containing a jet. Our goal is to understand the flow of energy with respect to the axis of hard scattering (thrust axis). As the strength (q^2) of the hard scattering increases, we expect increasing energy and particle multiplicity in the final state. Fig. 6.6a shows $\langle p_\perp \rangle$ from a powerlaw fit to single particle $p_\perp$ spectra as a function of charged particle multiplicity in the region $|\eta| < 0.5$ from the same p+p data sample [45]. Fig. 6.6b shows the

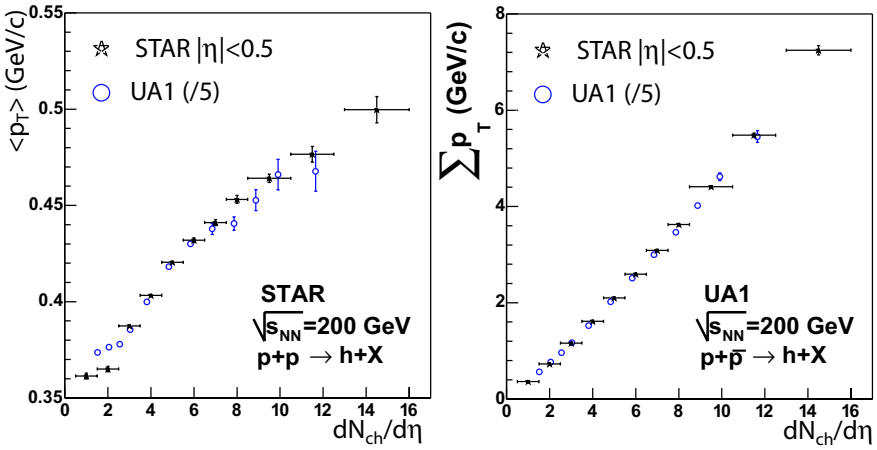

Figure 6.6: $\langle p_\perp \rangle$ and $\langle p_\perp^{sum} \rangle$ vs. $dN_{ch}/d\eta$ in minimum bias p+p and $p + \bar{p}$ events. The STAR data were measured in $|\eta| < 0.5$ while the UA1 data were measured in $|\eta| < 2.5$. The $dN_{ch}/d\eta$ from UA1 was divided by a factor of 5 to account for this difference. The STAR $dN_{ch}/d\eta$ is uncorrected, while the $\langle p_\perp \rangle$ is fully corrected for detector efficiency and acceptance. The STAR data is taken from Ref. [45].

$\sum p_\perp = \langle p_\perp \rangle \cdot dN/d\eta$ vs. $N_{\rm ch}$. Both $\langle p_\perp \rangle$ and $\sum p_\perp$ increase with $N_{\rm ch}$, indicative of the increased multiplicity of jet events. Our goal is to understand the magnitude and angular distribution of this energy with respect to the axis of hard scattering.

Ideally, we should reconstruct the thrust axis and approximate q^2 in di-jet events to quantify the direction and magnitude of the hard scattering. Approximately 10^3 events with two $p_\perp$ >5 GeV/c jets were reconstructed. In Fig. 6.7 we plot the azimuthal difference ($\Delta\phi$) between the leading two jets. A clear back-to-back topology is present, signified by the peak at $\Delta\phi$= 180°. Qualitatively, the results do not depend on the jet algorithm used. This represents the first direct observance of di-jet events using topological jet reconstruction at RHIC. The $\Delta\phi$ distribution was fit with a gaussian function of the form

$$\frac{1}{\sqrt{2\pi\sigma^2}} e^{\frac{-(x-180^\circ)^2}{2\sigma^2}} \tag{6.3}$$

The cone algorithm yields $\sigma = 25 \pm 1.2^\circ$ while the k_T algorithm yields a slightly wider value of $\sigma = 31 \pm 1.2^\circ$. The width of the $\Delta\phi$ distributions narrows substantially as one increases the cut on jet-$p_\perp$ used to define the two leading jets in the event sample. For $p_\perp^{jet} > 7$ GeV/c, the three algorithms all yielded $\sigma \approx 10^\circ$.

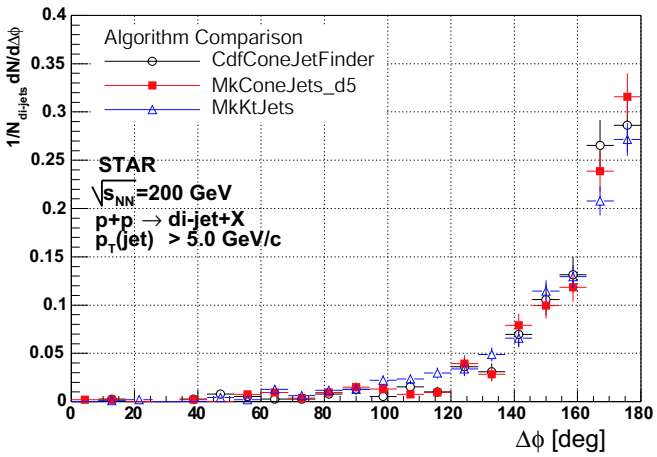

Figure 6.7: Azimuthal angle (in degrees) between two leading jets in di-jet events (see text for details). Results are shown for three algorithms. The distributions were fit according to Eq. 6.3 and the σ values are given in the text. Statistical error bars are shown.

Due to the limited number of di-jet events in the data sample we are forced to approximate the thrust axis and q^2 using the leading jet in each event. Fig. 6.8 shows the distribution of scalar sum $p_\perp$ ($p_\perp^{sum}$) of all charged hadrons (not just those in jets) with $p_\perp > 0.2$ GeV/c and $|\eta| < 1$ as a function of the azimuthal angle ($\Delta\phi$) from the axis of the leading jet. The region $\Delta\phi < 60°$ is within the cone of the leading jet ("toward"), the region $\Delta\phi > 120°$ is within the cone of the away-side jet ("away"), and the region $60° < \Delta\phi < 120°$ is in the "transverse" region. The cone radius $R = 0.7$ radians corresponds to $\Delta\phi \simeq 40°$. For comparison, the CDF results are shown for jet $p_\perp$=2, 5, and 30 GeV/c. The STAR and CDF data are in excellent quantitative agreement at the one common $p_\perp$ value of 5 GeV/c. There are two important features in this graph. First, the strength of the away-side peak grows with increasing values of $p_\perp$ of the leading jet. Thus, classifying events by the $p_\perp$ of the leading jet clearly selects for di-jet topologies. Second, and in contrast to the CDF data, the value of the transverse region is not sensitive to the $p_\perp$ of the leading jet. Instead, the value is constant and flat in the region $60° < \Delta\phi < 120°$ for $2.5 < p_\perp^{jet1} < 11.0$. Limited statistics prohibit the study beyond $p_\perp$ of 11 GeV/c with the present data. The energy flow in the transverse region is composed of contributions from both initial

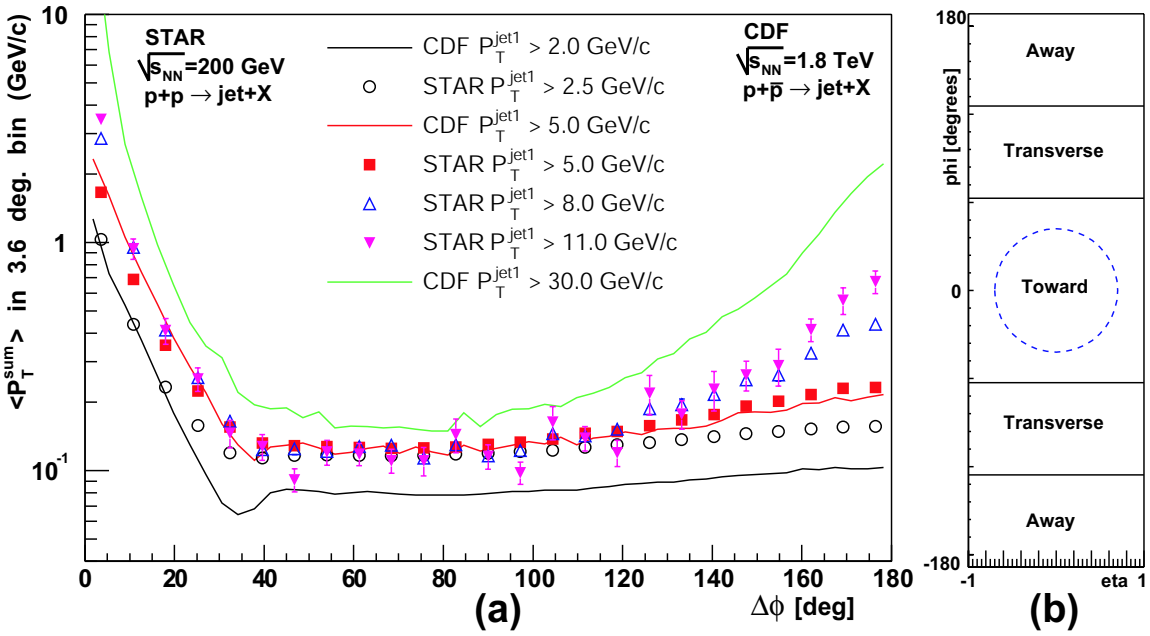

Figure 6.8: $\langle p_\perp^{sum} \rangle$ vs. $\Delta\phi$ from leading jet in p+p events measured at STAR $p + \bar{p}$ events at CDF. The $p_\perp = 5$ GeV/c data from STAR (red points) and CDF (red curve) are directly comparable. Statistical error bars (often smaller than the symbols) are shown.

state and final state radiation, as well as breakup of the "spectator" partons that did not participate in the hard scattering. In jet studies, this region is generally referred to as the "underlying event." One can appeal to Monte Carlo event generators in an attempt to decompose the transverse region into various components. For our purposes, we need only study the magnitude and evolution of the transverse region as a function of $p_\perp^{jet1}$.

Fig. 6.9 shows the integrated $p_\perp^{sum}$ in the toward, away, and transverse regions as a function of $p_\perp^{jet1}$. Both the toward and away curves show an approximately linear dependence on $p_\perp^{jet1}$. Further, the STAR and CDF data are in excellent qualitative agreement for both the toward and away regions. From the STAR data we find the ratio of reconstructed $\frac{p_\perp^{sum}(\text{toward})}{p_\perp^{sum}(\text{away})} \simeq 2.4$, constant with $p_\perp$. This value is understood to be driven by two competing effects, both relating to the non-hermetic nature of the analysis. First, the use of only charged hadrons in jet identification introduces a bias whereby the leading jet in the event has most likely fragmented preferentially

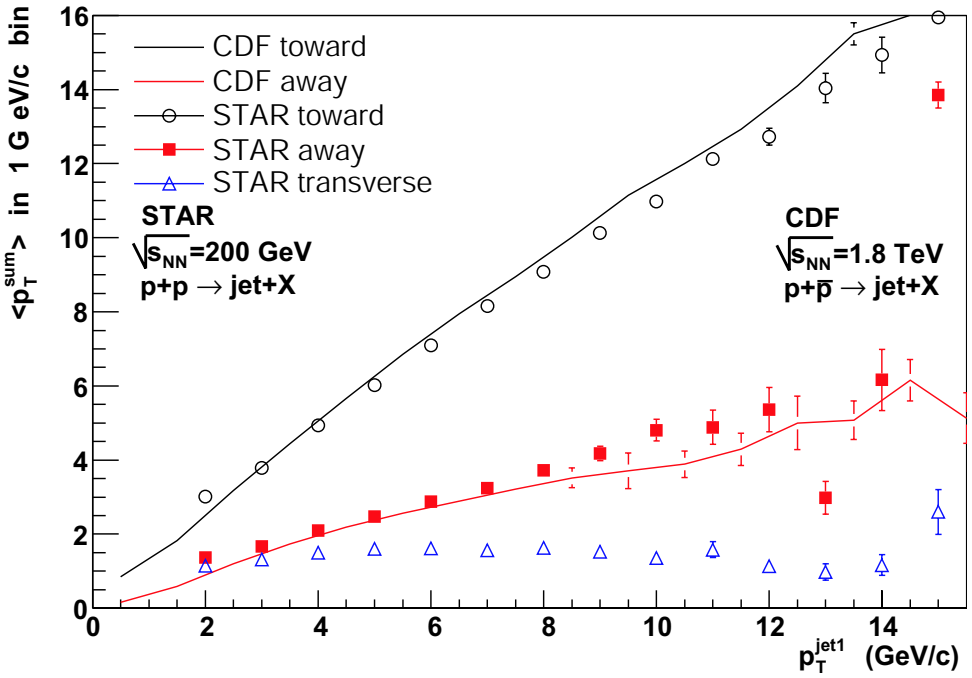

Figure 6.9: Integrated $\langle p_{\perp}^{sum} \rangle$ in the toward, away, and transverse event regions as a function of $p_{\perp}$ of the leading jet as measured at STAR and CDF [46]. Statistical error bars are shown.

to charged particles. Thus, even if two partons emerge from the hard scattering with identical $p_{\perp}$ values, we may reconstruct a very asymmetric di-jet $p_{\perp}$ distribution. Second, the unknown $x_{Bjorken}$ values of the colliding partons yield only a loose correlation in η of the outgoing partons (and also jets). Previous studies [4] show that the correlation width is larger than the longitudinal acceptance of the STAR detector. Thus, some fraction of the away-side jet can "bleed" out of the STAR acceptance[4]. However, the full containment of the away-side jet will not be critical for the remaining analysis, as the comparison of p+p and Au+Au data are made using an identical detector configuration. Finally, let us note that the energy flow in the transverse region is approximately constant as a function of $p_{\perp}^{jet1}$.

[4]The astute reader may then question the agreement between STAR and CDF for the "away" region, as CDF has a significantly larger η-acceptance. However, this specific CDF analysis used only a subset of the total acceptance ($|\eta| < 1$), identical to that presented here.

6.4 Relating Leading Hadrons to Jets

In the previous section we provided the first measurement of jets and di-jets in p+p collisions at RHIC. We now use that data to establish the relationship between leading hadrons and the jets from which they arise. Our purpose is two-fold. We must first establish the energy relationship between a high-$p_\perp$ hadron and its parent jet. Second, we must establish the precision with which we can resolve the jet direction by simply measuring the leading hadron. In many ways this is a step backward. However, the high background of Au+Au events makes direct jet identification impractical in the jet $p_\perp$ regions accessible within the statistics of the present data set.

The mean fraction of the jet-$p_\perp$ carried by the LCP[5] is given by:

$$\langle z \rangle = \langle \frac{p_\perp^{lcp}}{p_\perp^{jet}} \rangle \tag{6.4}$$

Fig. 6.10a shows $\langle z \rangle$ vs. the $p_\perp$ of the LCP. There is a general rise of the distribution

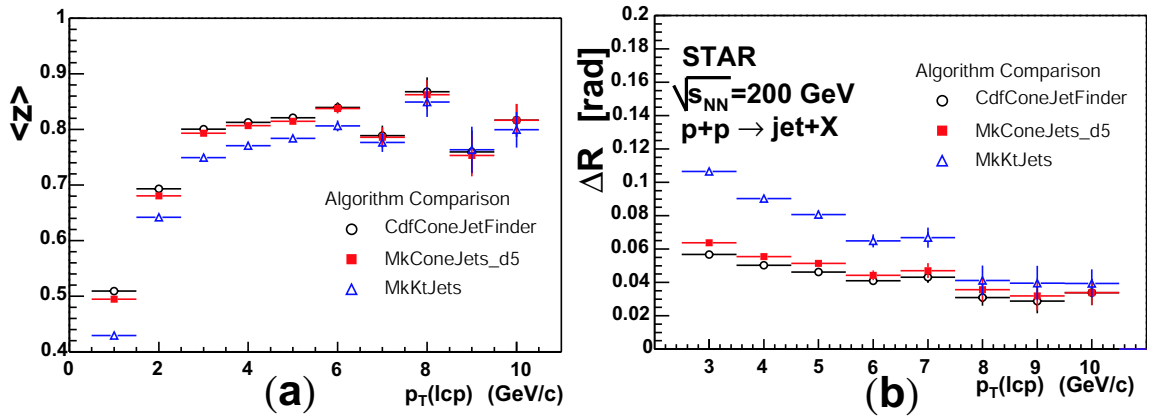

Figure 6.10: (a) scalar $\langle \frac{p_\perp^{LCP}}{p_\perp^{jet}} \rangle$ and (b) $\langle \Delta R \rangle$ vs. $p_\perp^{LCP}$. Statistical error bars are shown. The rise in (a) for $p_\perp^{LCP} < 3$ GeV/c is artificially enhanced by the event selection. See text for details.

for $p_\perp$ <3 GeV/c and then a near plateau for $3 < p_\perp < 8$ GeV/c. The sharp rise for low $p_\perp$ is artificially enhanced by the event selection, where only events with a jet satisfying $p_\perp$ >2.5 GeV/c were analyzed. However, the $\langle z \rangle$ distribution was

[5]Leading Charged Particle

found to be insensitive to the event selection for $p_\perp$ >3 GeV/c. In this region all three algorithms yield $0.75 < \langle z \rangle < 0.85$. We thus conclude that leading hadrons of $3 < p_\perp < 8$ GeV/c carry, on average, 75-85% of the jet transverse momentum, in agreement with a previous E711 p+Nucleus study at $\sqrt{s_{\rm NN}}$= 38.8 GeV [48]. This is in fact an illustration of the well established "trigger-bias" effect: the PDFs tend to fall off faster with increasing momentum than do the FFs. Therefore, the most efficient way of obtaining a high-$p_\perp$ hadron is to shift towards lower x in the PDF and higher z in the FF [4].

Fig. 6.10b shows the mean angular distance $\langle \Delta R \rangle$ vs. $p_\perp^{lcp}$ where ΔR is calculated as $\Delta R = \sqrt{(\phi_{jet} - \phi_{lcp})^2 + (\eta_{jet} - \eta_{lcp})^2}$. One sees a clear decrease in $\langle \Delta R \rangle$ with increasing $p_\perp$, implying that the LCP becomes increasingly collinear with the jet axis as the $p_\perp$ of the LCP increases. Note that 5° corresponds to 0.08 radians. Once again, we find that the k_T jets are wider on average, corresponding to higher values of $\langle \Delta R \rangle$ when compared to the cone algorithm at the same $p_\perp$. This further suggests that the k_T algorithm is more prone to add soft particles on the periphery of the jet cone either from gluon radiation or background sources. Using the data from the cone algorithm in Figs. 6.10 we conclude that leading hadrons of $3 < p_\perp < 10$ GeV/c are highly collinear with the jet direction (within 5°) and carry on average ≈80-85% of the jet transverse momentum. Therefore, we can use the "trigger-bias" effect to reliably tag the jet direction using only the leading charged hadron.

6.5 Azimuthal Correlations

In central Au+Au collisions the charged particle multiplicity is too large to perform direct jet reconstruction for jets with $p_\perp$ <10 GeV/c, where the total jet energy is significantly less then the contribution from the underlying event. However, we can use the knowledge gained in the previous section to look for jet-like correlations of charged hadrons. Our approach will be to study two-particle azimuthal correlations to search for high-$p_\perp$ particles that are close in angle ($\Delta\phi \sim 0$) and back-to-back ($\Delta\phi \sim \pi$). In p+p data this is a straightforward analysis. For example, the UA1 collaboration used a similar analysis to first identify jet and di-jet events in $p + \bar{p}$

events at $\sqrt{s_{\rm NN}}$=540 GeV [49]. However, in Au+Au data there exist physical processes which provide additional sources of angular correlations. We therefore invest a large amount of effort in the Au+Au analysis to extract a clean jet (and di-jet) signal above the background.

In the previous section we demonstrated that high-$p_\perp$ hadrons carry a large fraction of the jet energy and are highly collinear with the jet axis. We therefore use $4 \leq p_\perp \leq 6$ GeV/c hadrons to tag the jet direction[6]. Events with at least one large transverse momentum hadron ($4 \leq p_\perp^{trig} \leq 6$ GeV/c), defined to be a *trigger* particle, are used in this analysis. There can be more than one trigger particle per event. For each of the trigger particles in the event, we increment the number $N(\Delta\phi, \Delta\eta)$ of *associated* tracks with 2 GeV/c $< p_\perp < p_\perp^{trig}$ as a function of their azimuthal ($\Delta\phi$) and pseudo-rapidity ($\Delta\eta$) relative to the trigger particle. The choice of the 2 GeV/c lower threshold will be explained in the following section. We then construct an overall azimuthal pair distribution per trigger particle,

$$C_2(\Delta\phi) \equiv \frac{1}{N_{trigger}} \frac{1}{\epsilon} \frac{dN}{d(\Delta\phi)} \tag{6.5}$$

where $N_{trigger}$ is the observed number of tracks satisfying the trigger requirement. The efficiency ϵ for finding the associated particle is evaluated by embedding simulated tracks in real data. In order to have a high and constant tracking efficiency, the tracks are required to have $|\eta| < 0.7$, which translates to a relative pseudo-rapidity acceptance of $|\Delta\eta| < 1.4$. The single track reconstruction efficiency varies from 77% for the most central Au+Au collisions to 90% for p+p collisions, as shown in Fig. 3.4 and listed in Table 6.2.

If the $\Delta\phi$ distribution measured in p+p and Au+Au data is consistent with hard scattering and jet fragmentation, we expect to find the following:

1. A peak at $\Delta\phi \sim 0$ from particles coming from the same jet. If we take the jet direction to be defined by $\hat{p}_\perp^{trig}$ then this peak will be centered at $\Delta\phi = 0$ and is referred to as the "near-side" peak.

[6]The upper bound of 6 GeV/c prevented contamination from luminosity dependent tracking distortions in central Au+Au events which were not fully corrected for at the time of this analysis.

2. A peak at $\Delta\phi \sim |\pi|$ from particles coming from back-to-back jets. If we take the jet direction to be defined by $\hat{p}_{\perp}^{trig}$ then this peak will be centered at $\Delta\phi = |\pi|$ and is referred to as the "away-side" peak.

3. $C_2(\Delta\phi)$ should have a significant contribution for two-particle combinations where both particles have the same charge sign ($++$ or $--$). This is a characteristic of jet fragmentation that is not shared by most resonance decays.

4. If we divide $C_2(\Delta\phi)$ into subsets that come from (i) oppositely charged pairs ($+-$ and $-+$) and (ii) like charged pairs ($++$ and $--$), the ratio of $C_2(\Delta\phi)_{opp.charge}$ to $C_2(\Delta\phi)_{samecharge}$ should equal 2.7, in accordance with previous fragmentation studies from LEP [50]. This effect will be explained in detail in section 6.5.1

For the Au+Au data the events were required to have $|z_{vertex}| < 25$ cm, where a cut of $|z_{vertex}| < 25$ cm was already selected at the trigger level. The p+p events were required to have $|z_{vertex}| < 70$ cm, which corresponded to the largest possible event acceptance that allowed for an $\eta = 0.7$ track to cross all 45 padrows of the TPC. Due to the $1/N_{trigger}$ factor in Eq. 6.5, the $\Delta\phi$ correlation is self-normalizing to first order. Therefore, a premium was placed on selecting high quality reconstructed tracks and minimizing background tracks. The analysis was constrained to primary tracks that satisfied $p_{\perp}$ >2.0 GeV/c,$|\eta|$ <0.7, $|dca_{track-to-beamline}|$ <2 cm, and $N_{fit\ points}$ >24. This represents a track selection that is stricter than that used for the topological jet analysis in the p+p data, which was driven by the requirements to maximize both the η and $p_{\perp}$ acceptance to contain the full jet cone and fully exploit the limited statistics.

6.5.1 Background Sources

In Au+Au events multiple processes can contribute to $D(\Delta\phi)$. Primary contributions include jets, di-jets, resonance decays and elliptic flow. Additionally, the number of hard parton-parton scatterings per event increases with centrality. Jet production should scale approximately with the number of binary collisions N_{coll} (see App. E). In a central Au+Au collision N_{coll} grows to ∼1000 ($N_{coll} \sim A^{4/3}$). Thus, there will

be not one but many jets in a central Au+Au collision, creating a combinatoric contribution to $C_2(\Delta\phi)$ as well.

When measuring a signal in a high background environment, one must first maximize the signal to background ratio. For this analysis, using only particles with $p_\perp$ >2 GeV/c eliminates over 99% of the tracks present in a central Au+Au collision without cutting significantly into the yield of leading hadrons from $p_\perp$ >4 GeV/c jets, and thus increases the signal to background ratio. One then has two choices to extract the signal yield. First, one can remove the background in a self-normalizing fashion. For example, in studies of $\Upsilon \rightarrow e^+ + e^-$ one models the background contribution to the invariant mass spectrum by using a like-sign analysis. This allows for unambiguous background subtraction without a complete understanding of the composition of the background. Alternatively, if the background is sufficiently well understood it can be modeled (or calculated). We use a combination of both methods in this analysis.

We first use a background subtraction method to study the structure of the near-side peak in $C_2(\Delta\phi)$. The jet and di-jet studies in p+p data show that particles from the same jet will be close in both $\Delta\phi$ and $\Delta\eta$. Particles from back-to-back jets will be highly correlated in $\Delta\phi$, but only loosely correlated in $\Delta\eta$ due to the unknown longitudinal momentum fraction ($x,\ 0 \leq x \leq 1$) of the colliding hadron energy that each incoming parton carries. However, measurements in Au+Au collisions from the STAR collaboration show that correlations stemming from elliptic flow are distributed across all regions of $\Delta\eta$ for particles at mid-rapidity [51]. The contribution from elliptic flow as measured in the region $|\Delta\eta| < 0.75$ should be the same as that measured in the region $|\Delta\eta| > 0.5$. We can therefore measure $C_2(\Delta\phi)$ in the regions $|\Delta\eta| < 0.5$ and $|\Delta\eta| > 0.5$ and subtract the two. The result should still contain all of the correlation from particles in the same jet. We will have subtracted, by design, the contribution from elliptic flow, di-jets, and combinatorics due to multiple scatterings per event.

6.5.2 Jets in Au+Au Collisions

Identical analysis procedures are applied to the p+p and Au+Au data. Displayed in Figure 6.11 are the azimuthal distributions for same-sign and opposite-sign charged pairs from the a) p+p data and b) minimum bias Au+Au data for $4 < p_{\perp}^{trig} < 6$ GeV/c. The data are integrated over the relative pseudo-rapidity range $0 < |\Delta\eta| <$

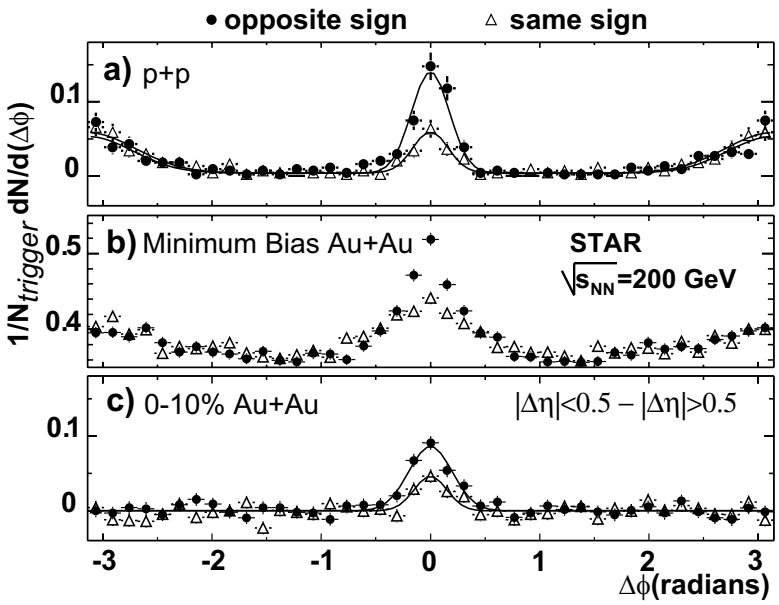

Figure 6.11: Azimuthal distributions of same-sign and opposite-sign pairs for a) p+p, b) minimum bias Au+Au, and c) background-subtracted central Au+Au collisions. All correlation functions require a trigger particle with $4 < p_{\perp}^{trig} < 6$ GeV/c and associated particles with 2 GeV/c $< p_T < p_{\perp}^{trig}$. The curves are one- or two- Gaussian fits.

1.4. Clear correlation peaks are observed near $\Delta\phi \sim 0$ and $\Delta\phi \sim \pi$ in the data. The opposite-sign correlations at small relative azimuth are larger than those of the same-sign particle pairs, while the sign has a negligible effect on the back-to-back correlations.

To isolate the jet-like correlations (localized in $\Delta\phi$, $\Delta\eta$) in central Au+Au collisions, the azimuthal distributions are measured for two regions of relative pseudo-rapidity, $|\Delta\eta| < 0.5$ and $0.5 < |\Delta\eta| < 1.4$ [51]. The difference between the small and large relative pseudo-rapidity azimuthal distributions is displayed in Figure 6.11c

along with single Gaussian fits. Near $\Delta\phi = 0$, the azimuthal distributions from Au+Au and p+p have similar shapes. For the opposite-sign azimuthal distributions, the Gaussian widths are $0.17 \pm 0.01(stat.) \pm 0.03(sys.)$ radians for p+p data, and $0.20 \pm 0.02(stat.) \pm 0.03(sys.)$ radians for the central Au+Au data. For the same-sign azimuthal distributions, the Gaussian widths are $0.16 \pm 0.02(stat.) \pm 0.03(sys.)$ radians for p+p data, and $0.15 \pm 0.03(stat.) \pm 0.04(sys.)$ radians for the central Au+Au data. The systematic errors reflect the spread of values found for different choices of the $\Delta\phi$ bin width. Within the errors, there are no significant differences between the small-angle correlation widths for p+p and central Au+Au collisions.

The ratios of the opposite-sign to same-sign peak areas are $2.7 \pm 0.9(stat.) \pm 0.2(sys.)$ for p+p and $2.5 \pm 0.6(stat.) \pm 0.2(sys.)$ for central Au+Au collisions. In jet fragmentation, there are dynamical charge correlations between the leading and next-to-leading charged hadrons [50] that originate from the formation of $q\bar{q}$ pairs along a string between two partons. This results in a preferential ordering into oppositely-charged adjacent particles along a string during fragmentation. The Hijing event generator, which utilizes the Lund string fragmentation scheme [52] incorporating these concepts, predicts a ratio of 2.6 ± 0.7 for the opposite-sign to same-sign correlation strengths. The agreement of this ratio with those measured in the central Au+Au and p+p suggests that the same jet production mechanism is responsible for a majority of the charged hadrons with $p_T > 4$ GeV/c in p+p and central Au+Au collisions.

The decay of resonances would also lead to small-angle azimuthal correlations, but a resonance decay origin is unlikely due to the observed correlation of particles with the same charge sign, the similarity in the measured small-angle azimuthal correlation widths in the Au+Au and p+p interactions, and the strong back-to-back correlations of large p_T particles seen for p+p collisions in Fig. 6.11a. The latter correlations, indicative of di-jet events [49], are removed from the central Au+Au sample by the subtraction in Fig. 6.11c. A quantitative analysis of back-to-back jet survival in Au+Au requires the more detailed treatment of background correlations described below.

In addition to correlations due to jets, the two-particle azimuthal distributions in

Au+Au exhibit a structure attributable to an anisotropy of single particle production relative to the reaction plane. Previous measurements [51] indicate that, even at large transverse momentum, the particle distributions contain an anisotropy due to elliptic flow that can be characterized by

$$dN/d(\phi - \Phi_r) \propto 1 + 2v_2 \cos(2(\phi - \Phi_r)) \tag{6.6}$$

where Φ_r is the reaction plane angle determined event by event and v_2 is the elliptic flow parameter. This leads to a two-particle azimuthal distribution of the form, $dN/d\Delta\phi = B(1 + 2v_2^2 \cos(2\Delta\phi))$. The elliptic flow component of the two-particle azimuthal distribution is measured using several methods [51]. In this thesis, we use v_2 as determined using a reaction-plane method. The dependence of v_2 on both centrality and $p_\perp$ is one of the major physics topics at RHIC, and we shall return to this in the concluding chapter. For the purposes of this analysis, however, we note that v_2 is approximately constant with $p_\perp$ for $p_\perp > \sim 2$ GeV/c, as shown in Fig. 6.12. Because we only consider particles with $p_\perp > 2$ GeV/c, we therefore take v_2 to be constant with $p_\perp$ in the following calculations.

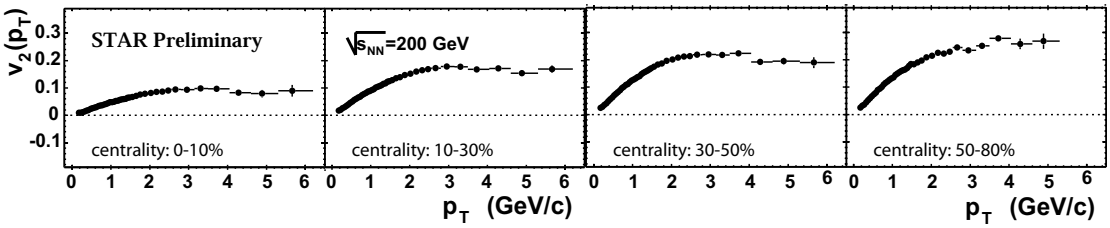

Figure 6.12: The elliptic flow parameter v_2 vs. $p_\perp$ from the two-particle correlation method using charged hadrons. The data are shown for four centralities of Au+Au collisions.

A simple reference model can be constructed for the two-particle azimuthal distributions of high-p_T particles in Au+Au collisions. A number of independent hard scatterings (each similar to that measured in a triggered p+p event) included in an event with correlations due to elliptic flow can be represented by the azimuthal distribution,

$$C_2^{\rm model} = C_2^{\rm pp} + B(1 + 2v_2^2 \cos(2\Delta\phi)). \tag{6.7}$$

The elliptic flow parameter (v_2) is measured independently in the same set of events, and is taken to be constant for $p_T > 2$ GeV/c [51]. The parameter B is then determined by fitting the observed $C_2^{\mathrm{AuAu}}(\Delta\phi)$ in the region $0.75 < |\Delta\phi| < 2.24$ radians, which is largely free of jet contributions in the p+p data. Further, in Sec. 6.3 we have shown that the sum-$p_\perp$ in this region is approximately independent of the momentum transfer of the hard-scattering, which characterized by the $p_\perp$ of the leading charged jet.

In Figure 6.13, the azimuthal distributions for $0 < |\Delta\eta| < 1.4$ in Au+Au collisions at various centralities are compared to Equation 6.7 using the measured p+p data. The centrality selection is constructed by subdividing the Au+Au minimum bias data

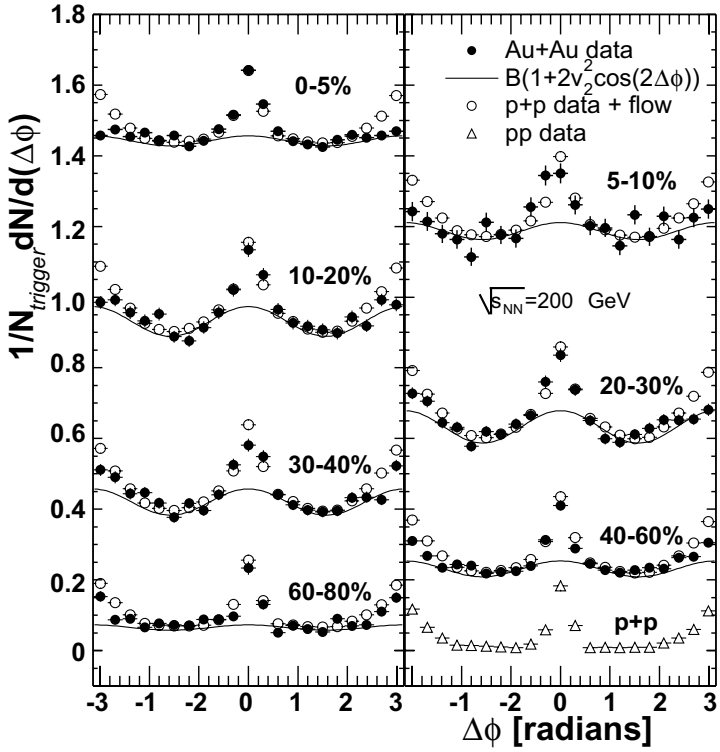

Figure 6.13: Azimuthal distributions ($0 < |\Delta\eta| < 1.4$, $4 < p_T^{trig} < 6$ GeV/c) for Au+Au collisions (solid circles) compared to the expected distributions C_2^{model} from Equation 6.7 (open circles). Also shown is the elliptic flow contribution for each centrality (solid curve).

sample into subsamples with different charged particle multiplicities within $|\eta| < 0.5$

Centrality(%)	N_{part}	ϵ	v_2	B
60-80	20±6	0.89	0.24±0.04	0.065±0.003
40-60	61±10	0.88	0.22±0.01	0.231±0.003
30-40	114±13	0.87	0.21±0.01	0.420±0.005
20-30	165±13	0.86	0.19±0.01	0.633±0.005
10-20	232±11	0.83	0.15±0.01	0.931±0.006
5-10	298±10	0.81	0.10±0.01	1.187±0.008
0-5	352±7	0.77	0.07±0.01	1.442±0.003

Table 6.2: Centrality, number of participants, single track efficiency ϵ, v_2, ($2 < p_\perp < 6$ GeV/c), and normalization constant B. The errors on v_2 and B are statistical only, while the errors on the number of participants are systematic (see App. E).

(See Appendix E). The parameters v_2 and B are determined independently for each centrality bin, and are listed in Table 6.2. A clear growth in the vertical offset is seen as a function of centrality. This is indicative of the rise of the combinatorial background, the strength of which is characterized by the magnitude of the parameter B. We expect B to increase with the the total particle multiplicity ($N_{ch} \sim N_{part}$), as seen in the data. For all centralities, the azimuthal correlation near $\Delta\phi = 0$ is well described by Equation 6.7. This indicates that the same mechanism (hard parton scattering and fragmentation) is dominantly responsible for high-transverse momentum particle production in p+p and Au+Au collisions. However, the back-to-back correlations are suppressed in Au+Au collisions compared to the expectation from Equation 6.7, and the suppression is greater for more central collisions. The most central collisions show no indication of any back-to-back correlations beyond that expected from elliptic flow.

The ratio of the measured Au+Au correlation excess relative to the p+p correlation is:

$$I_{AA}(\Delta\phi_1, \Delta\phi_2) = \frac{\int_{\Delta\phi_1}^{\Delta\phi_2} d(\Delta\phi) C_2^{\mathrm{AuAu}} - B(1 + 2v_2^2 \cos(2\Delta\phi))}{\int_{\Delta\phi_1}^{\Delta\phi_2} d(\Delta\phi) C_2^{\mathrm{pp}}}. \tag{6.8}$$

The ratio can be plotted as a function of the number of participating nucleons (N_{part}), deduced from the centrality bins as described in App. E. I_{AA} is measured for both the small-angle ($|\Delta\phi| < 0.75$ radians) and back-to-back ($|\Delta\phi| > 2.24$ radians) regions. The ratio should be unity if the hard-scattering component of Au+Au collisions is

simply a superposition of p+p collisions unaffected by the nuclear medium. These ratios are given in Figure 6.14 for the trigger particle momentum ranges indicated. The asymmetric systematic errors are dominated by the +5/-20% systematic uncertainty on v_2 due to the potential non-flow contributions [24] as well as other sources of systematic uncertainty [51]. For the most peripheral bin (smallest N_{part}), both

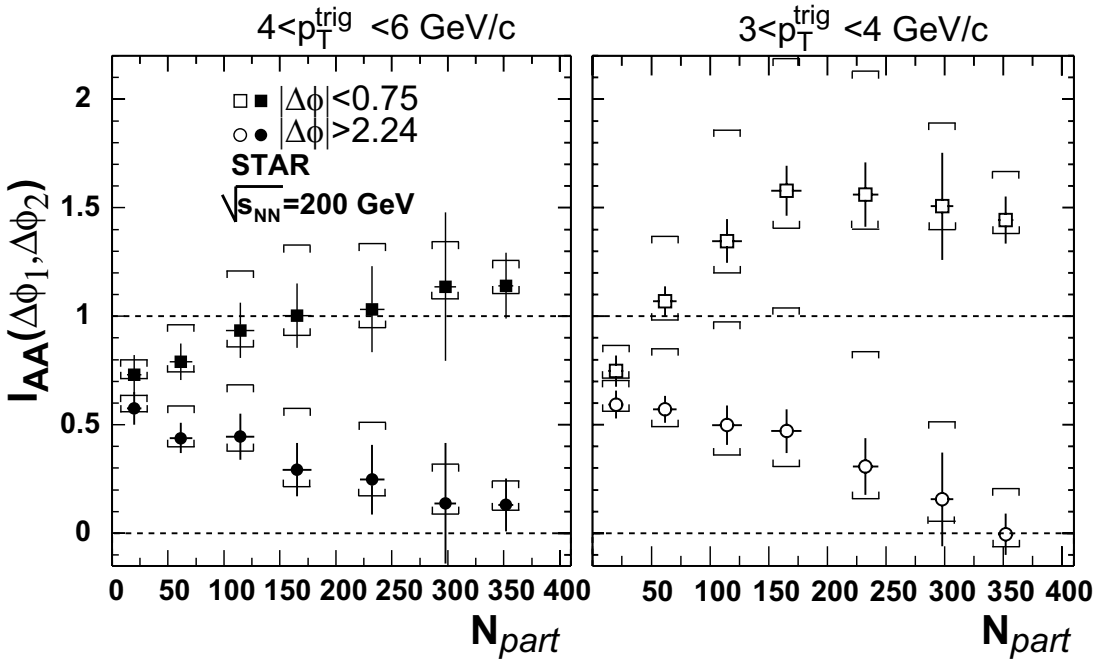

Figure 6.14: Ratio of Au+Au and p+p (Eq. 6.8) for small-angle (squares, $|\Delta\phi| < 0.75$ radians) and back-to-back (circles, $|\Delta\phi| > 2.24$ radians) azimuthal regions versus number of participating nucleons for trigger particle intervals $4 < p_{\perp}^{trig} < 6$ GeV/c (solid) and $3 < p_{\perp}^{trig} < 4$ GeV/c (hollow). The horizontal bars indicate the dominant systematic error (highly correlated among points) due to the uncertainty in v_2.

the small-angle and back-to-back correlation strengths are suppressed compared to the expectation from Equation 6.7. This intriguing phenomenon is not understood. It may be an indication of initial state nuclear effects such as shadowing of parton distributions or scattering by multiple nucleons, or may be indicative of energy loss in a dilute medium [53] [54]. As N_{part} increases, the small-angle correlation strength increases, with a more pronounced increase for the trigger particles with lower p_T threshold. If there were a large non-jet contribution to particle production

(i.e. collective transverse flow) at the trigger threshold and above, it would dilute the jet-related correlation signal and this ratio would be reduced. The back-to-back correlation strength, above background from elliptic flow, decreases with increasing N_{part} and is consistent with zero for the most central collisions. In the extreme case, if there were *no* elliptic flow for the 0-5% most central collisions, $I_{AA}(2.24, \pi) = 0.4 \pm 0.1$ for $4 < p_T^{trig} < 6$ GeV/c, compared to $I_{AA}(2.24, \pi) = 0.1 \pm 0.1$ using the measured elliptic flow value. Therefore, an overestimation of the elliptic flow cannot explain the observed suppression of back-to-back correlations.

In summary, we have measured azimuthal correlations for high-p_T charged particles over a large relative pseudo-rapidity range with full azimuthal angle coverage. Comparison of the opposite-sign and same-sign correlation strengths indicates that hard scattering and fragmentation is the predominant source of charged hadrons with $p_\perp > 4$ GeV/c in central Au+Au collisions. The azimuthal correlations in Au+Au collisions have been treated as the superposition of independently determined elliptic flow and individual hard parton scattering contributions, the latter measured in the STAR p+p data. The most striking feature of the hard-scattering component is a suppression of back-to-back di-hadron pairs relative to the near-angle pair. This suppression of the away-side correlations increases with increasing centrality.

Chapter 7

Interpretation and Comparison to Theory

In this chapter we discuss the results presented in Sec. 6.5, make comparison to theory, discuss the importance of these measurements in the broader context of the RHIC physics, and draw conclusions. The Au+Au data show the remarkable features that:

- the small-angle ($\Delta\phi \sim 0$) correlations are quantitatively similar to those from the p+p data. In central Au+Au events, the background-subtracted yield of small-angle pairs (relative to p+p) is consistent with one.
- For peripheral Au+Au collisions, the large-angle ($\Delta\phi \sim \pi$) correlations are quantitatively similar to those in p+p data, but for central Au+Au collisions, the background-subtracted yield of away-side pairs is strongly suppressed.

These phenomena are consistent with a picture in which observed hadrons at $p_T > 4$ GeV/c are fragments of hard scattered partons that were strongly scattered or absorbed in the nuclear medium. In this scenario the observed correlated pairs would result preferentially from hard-scattered partons generated on the periphery of the reaction zone and heading outwards, as predicted by Bjorken [14]. Therefore, the properties of small-angle hadron correlations will have a weak dependence on the size of the colliding system, whereas the back-to-back correlations will exhibit strong suppression for a large system relative to a small one, both as observed. The data are therefore consistent with large energy loss in a system that is opaque to the propagation of high-momentum partons. This interpretation, however, begs the following two questions:

1. Could there be a pre-hard-scattering mechanism that suppresses the cross section for hard parton-parton scattering?

2. Could the suppression of the away-side jet be due to hard-scattered partons actually fragmenting inside of the medium, with the fragmentation products losing energy via *hadronic* interactions with the medium?

These questions are considered below.

7.1 Alternative Particle Production Models

The last decade has witnessed tremendous theoretical effort to understand the effects of non-abelian induced gluon radiation. Another theoretical enterprise of equal magnitude has been developing in parallel to understand the potential phenomenon of "gluon saturation." The essential idea behind the model is that the nucleon PDF is gluon dominated at small-x. When nucleons are bound in a nucleus, and this nucleus is probed at small-x, the abundance of gluons leads to a novel saturation phenomenon that shadows the gluon contribution to the PDF. If there is substantial overlap of the gluon wave functions, the probability of two gluons fusing becomes large and effectively limits the number of gluons that can be found inside a nucleus. The theoretical activity was motivated by a significant scaling observed in identified single particle $m_\perp$ spectra in central Au+Au collisions. One interpretation was that this scaling was a direct remnant of the initial gluons which were liberated from gluon-saturated PDFs.

In practice, the theory involves calculations in semi-classical QCD. The theory is particularly attractive because of the (relative) ease of semi-classical calculations, the ability to calculate such non-perturbative bulk properties of Au+Au collisions as the total particle multiplicity, and for the clear solution to the unitarity crisis, whereby gluon-saturation effectively limits the growth of the total inelastic hadron-hadron cross section at asymptotically large energies. The calculations also lead to novel predictions such as high-$p_\perp$ suppression of inclusive particle spectra and a significant "mono-jet" cross section (from 2 to 1 gluon fusion).

These predictions all stem from a unique property of the Au wave function when probed at RHIC scales. The saturation model is therefore often referred to as an "initial state" model. The fact that models of partonic energy loss (a "final state" model) and the saturation model both described the observed high-$p_\perp$ suppression in Au+Au collisions was a driving factor leading to the d+Au run at RHIC. Before the data were taken, the saturation model predicted an $\sim$ 30% suppression in inclusive high-$p_\perp$ particle yields and the away-side di-hadron correlations [26], while perturbative QCD calculations predicted an *enhancement* of the single particle yields stemming from $p_\perp$ broadening effects [27] [55]. When the data were analyzed, all four RHIC experiments rapidly concluded that they found an enhancement of high-$p_\perp$ particles, in agreement with perturbative calculations and in clear contradiction to the saturation predictions (see Fig. 1.7) [25] [56] [57] [58]. Recent preliminary results from the BRAHMS collaboration *do* however suggest a suppression of high-$p_\perp$ inclusive spectra at forward rapidity ($x \approx \frac{2p_\perp}{\sqrt{s}} e^{-y} \approx 10^{-3}$) in d+Au collisions. This has renewed interest in the saturation calculations for the forward regime and raised the possibility that RHIC fortuitously occupies a kinematic region where the relative strength of (initial state) gluon saturation and (final state) partonic energy loss can be "dialed-in" by proper selection of transverse momentum and rapidity. However, the saturation predictions are in clear contradiction with the mid-rapidity charged hadron R_{AA} from d+Au collisions for $p_\perp > 4$ GeV/c.

7.2 Alternative Final-State Mechanisms

Could the observed high-$p_\perp$ suppression be due to strong hadronic interactions? This question is fundamentally rooted in estimates of the time required for a hard-scattered parton to fragment and form hadrons. Ref [59] is the most recent in a series of works that suggest outgoing partons *do* fragment inside the medium and can lose substantial energy via hadronic collisions. The calculations are (i) motivated by order-of-magnitude estimates for hadron formation time (t_{form}) and (ii) carried out using a combination of the PYTHIA event generator and a hadronic interaction code that

treats independent hadronic interactions within the medium[1]. The authors conclude that the suppression of inclusive single particle $p_\perp$ spectra can be described within their model.

Calculating the formation time of a hadron is clearly non-trivial; it probes the subtle distinction between perturbative and non-perturbative physics. Estimates ranging from 1-50 fm/c arise from application of identical formulae when applied by different authors [20] [59]. Perhaps the most fundamental estimate is given by Dokshitzer [60]. The hadron formation time (t_{form}) is the time needed for the parton to develop a radiative field around itself with the typical transverse momentum that separates perturbative and non-perturbative physics. This momentum is Λ_{QCD} and is usually taken as ∼200 MeV (see Fig. 1.1b). The hadronic radius is then given by $R_h = 1/\Lambda_{QCD}$. Dokshitzer derives [60] that $t_{form} \approx E_{parton} \cdot R_h^2 \approx E_{parton}/\Lambda_{QCD}^2$. Using $\Lambda_{QCD}^2 = 0.2$ GeV, we find $t_{form} = 10$ (20) fm/c for a relatively low momentum parton of $E = 2.5$ (5.0) GeV. Ref [59] uses a value of $\Lambda_{QCD}^2 = 1.2$ GeV to derive formation times smaller by a factor of four. These timescales are compared to the lifetime of the medium, which is typically taken as ∼10 fm/c. Clearly, factors of four significantly change one's conclusion regarding whether partons fragment inside this medium.

These estimates should certainly be taken with a degree of caution. We are not lost, however, as we can appeal to data to address this question. Ref [59] requires an initial hadronic density of 1 nucleon / fm^3 to produce sufficient hadronic energy loss to describe the central Au+Au data. The same mechanism should therefore exist in d+Au data where the initial density is 1 nucleon /fm^3, thereby implying a suppression of high-$p_\perp$ inclusive spectra and back-to-back di-hadron pairs. As shown in Fig. 1.7, this is clearly in contradiction with the data. We hope the data provided in this document, specifically the quantitatively similar nature of the near-angle di-hadron peak in p+p and all centralities of Au+Au, will provide significant constraints on models of hadronic energy loss. This issue is not yet closed within the community, and perhaps will *only* be determined when the hadronic energy loss model predictions become more specific, as we shall address at the end of this chapter.

[1]Given the experimental verification of the LPM effect, one could perhaps be skeptical of the application of Monte Carlo methods to the problem of a particle traversing dense media.

7.3 Comparison to Theory

We now compare the data to three recent theoretical analyses, attempting to briefly present the most significant strengths and weaknesses of each analysis without diving too deeply into the details of the calculation. Broadly speaking, the large suppression of the back-to-back correlation peak in central Au+Au collisions is thought to originate from contributions of several phenomena:

- Intrinsic transverse momentum k_T of partons in a nucleus
- Partonic energy loss dE/dx in medium
- Size and dynamical expansion of the medium
- $p_\perp$ broadening of jets due to multiple scattering of partons in the medium.

The relative contribution of these effects to the away-side suppression is the subject of much current experimental and theoretical work. In some cases these effects can be factorized, the best example being the use of p+p and d+Au collisions to study the magnitude of k_T. Some effects are highly coupled – calculations predict that both partonic dE/dx and $p_\perp$ broadening result for strong final state interactions and can in fact be functionally related. The analyses presented below were chosen because of their particular focus on the relevant contribution of the aforementioned effects.

7.3.1 Hydrodynamics + Jet Model

In Ref. [21], Hirano and Nara compose a two component scenario with the emphasis on a realistic modelling of the propagation of jets (component 1) through a dynamically expanding medium (component 2). The jet yield (for a p+p collision) is calculated in LO[2] pQCD, which was implemented via the PYTHIA 6.2 [52] Monte Carlo event generator. The PYTHIA code depends on several input factors which are given in Ref. [21]. The parameter choices were rather standard [3], with the exception of the choice of an independent fragmentation scheme (based on the Feynman-Field

[2]Leading Order

[3]CTEQ5L PDFs evaluated at $Q^2 = (p_\perp/2)^2,\ q^2 > 2$ GeV/c, $\langle k_T^2 \rangle = 1$ GeV^2/c^2

model)[4]. It was verified that the PYTHIA single particle $p_\perp$ distributions agreed well with existing $p + \bar{p}$ data at the same energies. In PYTHIA, the partonic k_T is incorporated by an additional convolution. This results in the insertion of the factors

$$\int dk_{T,a}^2 \; g(k_{T,a}) \int dk_{T,b}^2 \; g(k_{T,b}) \tag{7.1}$$

in the cross section formula given in Eqs. 1.3 and 1.4, where the functional form of $g(k_T)$ is taken to be a gaussian of width $\langle k_T^2 \rangle$ centered about zero. This is a standard parametrization. The jet yield in Au+Au collisions (*before* partonic energy loss) was assumed to scale with N_{coll}, specifically $d\sigma(Au + Au)/dp_\perp = \langle N_{coll} \rangle d\sigma(p + p)/dp_\perp$.

Hydrodynamics is employed to model the low $p_\perp$ dynamics of the medium. A particularly sensitive test of hydrodynamic calculations results in the comparison of elliptic flow v_2 values with data. At RHIC, the validity of hydrodynamic calculations are motivated by the agreement with species-dependent v_2 measurements at low-$p_\perp$. This indicates that the calculations quantitatively describe the fluid dynamics of the expanding medium. The Hirano-Nara calculation assumes a deconfined quark-gluon equation of state. With the EOS[5] specified, one can write down the components of the stress energy tensor $T^{\mu\nu}$. Imposing the continuity equation $\partial_\mu T^{\mu\nu} = 0$ yields a set of coupled differential equations that can be solved numerically in 3+1 dimensions. The solutions of these equations give both the density and the velocity flow as a function of position and time.

The hard scattered partons output from PYTHIA are propagated through the hydrodynamic description of the medium. The authors employ the results from a reaction operator calculation of coherent induced gluon radiation [15] [22] [54] [61] [62] [63], which is relevant for reactions where the number of jet scatterings is small. The first order formula is

$$\Delta E = C \int_0^\infty d\tau \; \rho(\tau, \overrightarrow{x}(\tau)) \; (\tau - \tau_0) \log\left(\frac{2E}{\mu^2 L}\right) \tag{7.2}$$

where the medium density function $\rho(\tau, \overrightarrow{x}(\tau))$ is obtained from the hydrodynamics and C is an adjustable parameter that depends on the parton species of both

[4]It is generally accepted that the Lünd string fragmentation model is in better agreement with data than the Feynman-Field model. However, the Monte Carlo implementation of the hydro+jet model prevented the use of the Lünd subroutines.

[5]Equation Of State

the propagating jet and the matter. The authors interpret the effective value of C (described below) as an average value. To summarize, hard scattered partons are produced via PYTHIA, lose energy while propagating through an expanding medium, and then hadronize as if they were in vacuum. These fragmentation products are used to construct the correlation function $C_2(\Delta\phi)$, which is compared to the STAR results after background subtraction (i.e., Au+Au data minus the "p+p + flow term" from Fig. 6.13).

The value of the scale constant C in Eq. 7.2 is highly constrained by the ratio of single particle $p_\perp$ spectra in p+p and Au+Au collisions. Fig. 7.1a compares hydro+jet model ($\langle k_T^2 \rangle$=1 GeV^2/c^2) predictions with R_{AA} obtained from π^0 mesons from central PHENIX data [23]. The curve C=0.27 best describes the data, showing quantitative

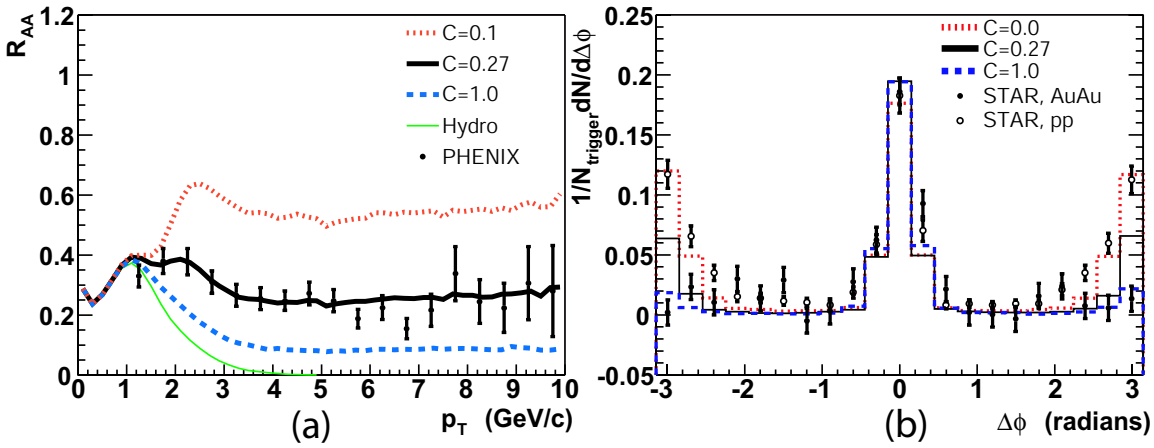

Figure 7.1: (a) Comparison of hydro+jet predictions for R_{AA} of π^0 mesons in 10% central collisions from PHENIX data [23] for different values of C. Figure taken from Ref. [21]. (b) Comparison of hydro+jet predictions for $C_2(\Delta\phi)$ in minimum bias p+p and 0-5% central Au+Au collisions at STAR. Figure taken from Ref. [21].

agreement for $2 < p_\perp < 10$ GeV/c. The sensitivity of the prediction is demonstrated by showing curves corresponding to different choices of C. Fig. 7.1b shows the corresponding prediction for $C_2(\Delta\phi)$ compared to both p+p and central Au+Au data from STAR. There are several features to note. First, setting $C = 0$ corresponds to no modification of the jet fragmentation and should therefore reproduce the p+p data. Excellent agreement is seen in both the near and away-side peaks, satisfying this

expectation. Second, varying C substantially has little effect on the near-side peak, having nearly negligible effect on both the integral and the width of the peak. Third, varying C *does* have a strong effect on the size of the away-side peak. However, the model only agrees with the central Au+Au data on the away-side for $C = 1$, which is clearly disallowed by Fig. 7.1a. The best fit value of $C = 0.27$ accounts for ∼50% of the away-side suppression. In this model, energy loss alone cannot describe the data.

In the single particle $p_\perp$ spectrum, there is a competition between k_T and energy loss. Increased k_T transports low-$p_\perp$ particles to higher $p_\perp$, stiffening the $p_\perp$ distribution, while energy loss transports high-$p_\perp$ particles to lower $p_\perp$, softening the $p_\perp$ distribution. Thus, increasing k_T in the hydro+jet model requires a simultaneous increase of the energy loss parameter C, with the net result constrained to fit the π^0 R_{AA} measurement. Fig. 7.2a studies the dependence of the correlation on k_T. The

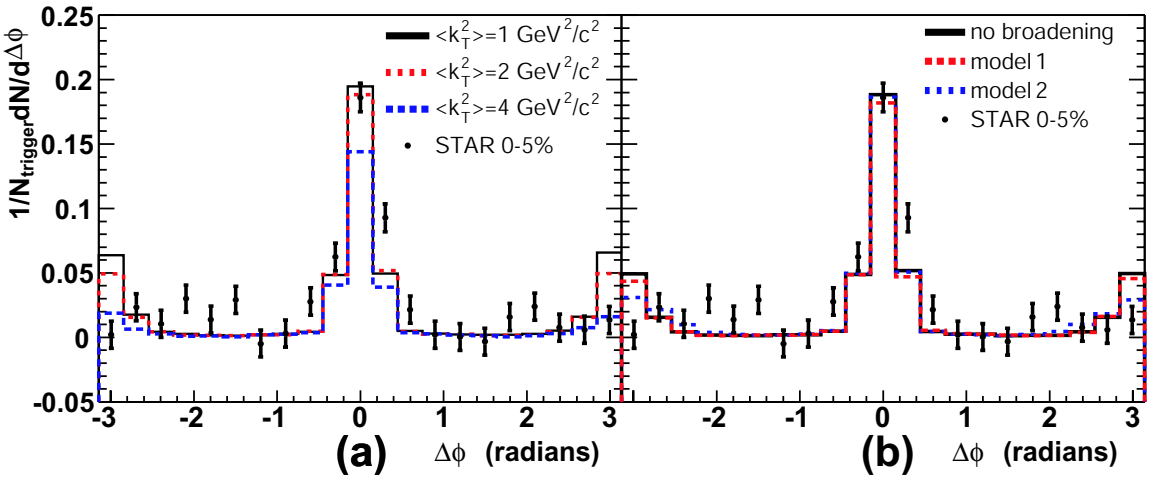

Figure 7.2: (A) k_T dependence of hydro+jet model compared to 0-5% central STAR Au+Au data. The parameter sets are described in the text. Figure taken from Ref. [21]. (B) Comparison of hydro+jet predictions including $p_\perp$ broadening for $C_2(\Delta\phi)$ to 0-5% central Au+Au collisions at STAR. Figure taken from Ref. [21]. See text for details.

parameter sets are $(\langle k_T^2\rangle, C) = (1.0, 0.27)$, $(2.0, 0.35)$ and $(4.0, 0.5)$, where $\langle k_T^2\rangle$ is in units of GeV^2/c^2. Larger values of k_T indeed decrease the strength of the away-side peak. However, a value of $\langle k_T^2\rangle = 4$ is needed for agreement in the away-side peak. At such extreme values, the strength of the near-angle peak is decreased, in quantitative

disagreement with the data.

The strong final state interactions of a fast parton with the medium lead to both non-abelian energy loss and $p_\perp$ broadening. Fast partons can build up a net non-zero momentum orthogonal to their original direction as they follow a zig-zag path through the medium. The $p_\perp$ broadening of these jets can be functionally related to the calculation of dE/dx. Hirano and Nara consider the predictions of two different calculations. The BDMPS calculation from Refs. [64] and [65] (model 1) predicts

$$\langle p_\perp^2 \rangle = \left(\frac{\alpha_s N_c}{4} \right)^{-1} \frac{dE}{dx}. \tag{7.3}$$

The Wang calculation from Ref. [66] (model 2) predicts

$$\langle p_\perp^2 \rangle = \left(\frac{\alpha_s N_c}{2} \right)^{-1} C \int_{\tau_0}^{\infty} d\tau \ \rho(\tau, \overrightarrow{x}(\tau)). \tag{7.4}$$

Eq. 7.3 was formally obtained in the limit of a static plasma, but is accurate except for a logarithmic correction for a longitudinally (1+1 dimensional) expanding plasma [67]. Hirano and Nara note that R_{AA} is largely insensitive to $p_\perp$ broadening. Fig. 7.2b shows the effect of $p_\perp$ broadening on the correlation function, using $\langle k_\perp^2 \rangle$=2 GeV^2/c^2 and C=0.35. The BDMPS result shows an additional factor of $\sim$2 suppression of the away-side peak, while the Wang prediction shows negligible influence on the away-side peak. Neither model has significant effect on the near-side peak. The difference between the two broadening models is not fully understood.

7.3.2 $p_\perp$ broadening in vacuum, cold, and hot nuclear matter

The study of Hirano and Nara shows that the away-side correlation peak is sensitive to k_T effects. The use of two $p_\perp$ broadening formalisms, however, yields conclusions that are different by a factor of two on the away-side. Vitev and Qiu have since performed a rigorous analysis to calculate the magnitude of the effect that $p_\perp$ broadening has on the away-side di-hadron correlation [55] [68]. They extend the GLV[6] reaction operator approach [15] to multiple elastic scatterings to account for longitudinal momentum

[6]Gyulassy, Vitev, and Levai

reduction due to the medium recoil when a fast parton propagates through cold nuclear matter, as probed in d+Au collisions. The total induced broadening can then be decomposed into initial state (IS) and final state (FS) portions [68] as

$$\langle \overrightarrow{k}_T^2 \rangle = \langle \overrightarrow{k}_T^2 \rangle_{vac} + 2 \left(\frac{\mu^2}{\lambda}\right)_{eff} \langle L \rangle_{IS} + 2 \left(\frac{1}{2}\right)_{projection} \left(\frac{\mu^2}{\lambda}\right)_{eff} \langle L \rangle_{FS} \qquad (7.5)$$

where a typical range for the transport coefficients for gluons in cold nuclear matter is given by $(\mu^2/\lambda_g)_{eff,\ IS \approx FS}$ = 0.1-0.3 GeV^2/fm. The value of $\langle \overrightarrow{k}_T^2 \rangle_{vac}$ = 1.5 GeV^2/c^2 is extracted from a di-hadron correlation analysis of preliminary p+p data from PHENIX. A similar analysis using the p+p data from STAR presented in this thesis yields $\langle \overrightarrow{k}_T^2 \rangle_{vac} = 1.7$ GeV^2/c^2.[7] No uncertainties are available for these k_T values. Fig. 7.3 shows a comparison of Vitev's resulting perturbative calculation with the STAR p+p data. The data show reasonable quantitative agreement, with the

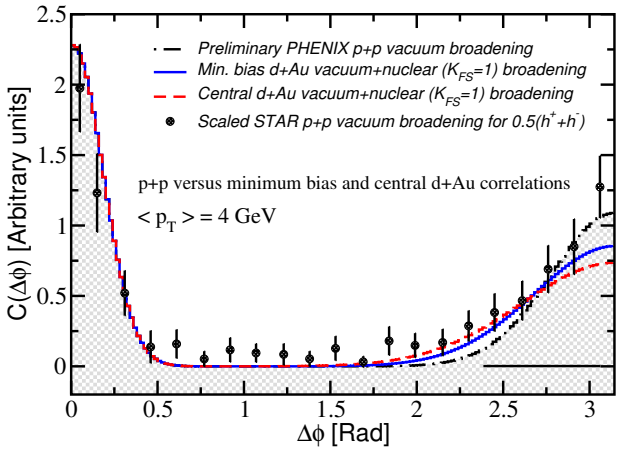

Figure 7.3: Elastic broadening of the back-to-back di-hadron correlation function in minimum bias p+p collisions compared to STAR data. Predictions are shown for d+Au collisions. Figure taken from Ref. [68].

slight discrepancy at $2.3 < \Delta\phi < 2.5$ attributed to the assumption of a gaussian k_T distribution. Power law corrections to this approximation are small and can be calculated [68] [15]. Vitev and Qiu then calculate the additional $p_\perp$ broadening in cold

[7] Werner Vogelsang, private communications

nuclear matter (d+Au collisions) using Eq. 7.5. Fig. 7.4a shows comparison of data and theory for p+p and d+Au data from STAR. The d+Au data come from RHIC RunIII and are not a part of this thesis analysis[8] but they are a critical constraint of modifications due to cold nuclear matter. The Vitev-Qiu prediction is in excellent

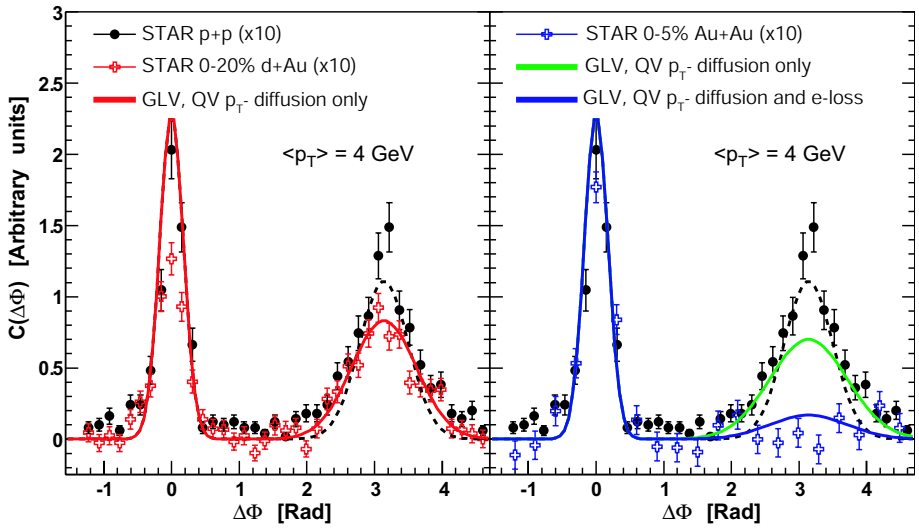

Figure 7.4: (a) The broadening of the far-side di-hadron correlation function in p+p and d+Au compared to STAR data. The data have been plotted for $-\pi < \Delta\phi < 3\pi/2$ to emphasize the difference of the near- and away-side peaks. (b) The same, but for p+p and 0-5% central Au+Au collisions. Predictions for Au+Au are shown for broadening only and broadening+energy loss. Figure reproduced from Ref. [19].

agreement with the away-side correlation peak in the d+Au data.

Predictions for central Au+Au are shown in Fig. 7.4b. In hot nuclear matter the last term in Eq. 7.5 is modified. The contribution of final state broadening $(\mu^2/\lambda)_{eff}\langle L\rangle_{FS}$ is then evaluated in a 1+1d Bjorken expanding QGP [67]. The initial gluon density dN_g/dy =1150 is fixed by the measured R_{AA} from central STAR and PHENIX data. Calculations were performed for two cases: (i) broadening only and (ii) broadening plus partonic energy loss. One clearly sees that, while broadening alone does widen the away-side correlation peak, it is still in significant disagreement with the data. However, the inclusion of energy loss in the same formalism results in

[8]While I did make significant contributions to the data taking, reduction, and general analysis, this analysis was completed by D.H. Hardtke

the near extinction of the away-side peak, in quantitative agreement with the data.

An analysis similar to that presented in Sec. 6.5 has recently been performed at the CERN SPS ($\sqrt{s_{NN}} = 19$ GeV/c) [69]. Using charged pion pairs of $p_\perp > 1$ GeV/c they find evidence for semi-hard scattering in the di-pion correlation function. While they do observe a broadening of the away-side peak in central Pb + Au collisions, they find no evidence for away-side suppression. This is perhaps consistent with $p_\perp$-broadening in cold nuclear matter, although a thorough theoretical analysis is necessary.

7.3.3 Global Extraction of Energy Loss

In Refs. [70] and [20], Wang analyzes data from (i) single particle $p_\perp$ spectra, (ii) elliptic flow spectra, (iii) semi-inclusive DIS, and (iii) di-hadron correlations in Au+Au collisions. He finds that a LO parton model incorporating partonic energy loss is in excellent quantitative agreement with the data and provides an approximate, but quantitative, measure of partonic energy loss. Additionally, he proposes the use of "hadron triggered" FFs for a more precise measure of parton energy loss.

The Wang parton model is a LO pQCD calculation with the addition of

- N_{coll} scaling from p+p to Au+Au
- Gaussian k_T smearing via Eq. 7.1 incorporating both intrinsic partonic k_T and nuclear broadening
- Impact parameter dependent shadowing of the PDFs in Au nuclei
- Modification of the FF due to radiative energy loss

The PDFs are assumed to be factorizable in the PDFs in a free nucleon (given by the MRS D- parameterization [71] and an impact parameter dependent modification [72] [73]. The modification to the PDFs is highly constrained by the STAR single particle $p_\perp$ distributions taken at the different beam energies of $\sqrt{s_{\rm NN}}$= 130 and $\sqrt{s_{\rm NN}}$=200 GeV. Partonic energy loss was incorporated via the modification of the FFs for parton

a of energy E to fragment to hadron h with momentum fraction z. The actual formula has its roots in the approximate definition:

$$\tilde{D}_{a\to h}(z) \approx \frac{1}{1-\Delta z} D_{a\to h}\left(\frac{z}{1-\Delta z}\right) \tag{7.6}$$

where the shift in z is related to the energy loss by $\Delta E/E = 1.6\Delta z$. The factor of 1.6 is mainly caused by the unitarity correction in the pQCD calculation, and a similar effect is also found in the opacity expansion approach [15]. The exact modification of the FF is in fact quite complicated and incorporates detailed balance between both radiative gluon energy loss and gluon absorption. The final FF is a function of z, Q^2, and ΔE, where ΔE is evaluated in a 1+1 dimensional expanding medium with gluon density $\rho_g(\tau, r)$ that is proportional to the transverse profile of participant nucleons. Wang uses the BKK[9] parameterizations for the unmodified FFs [74].

In Fig. 7.5 we show an example application of Eq. 7.6 for illustrative purposes. We plot the Kretzer parameterization of the FF for light quark fragmentation to a π^+ [12] from a LEP analysis: $D_{q\to\pi^0}(z) \simeq z^{-0.8}(1-z)^{0.9}$. Using the static 1-d energy loss calculation from Ref [70] for $E_{jet} = 10$ GeV, we derive $\Delta E \sim 2$ GeV and $\Delta z \sim 0.2$. The modified FF is softened considerably with respect to the vacuum FF.

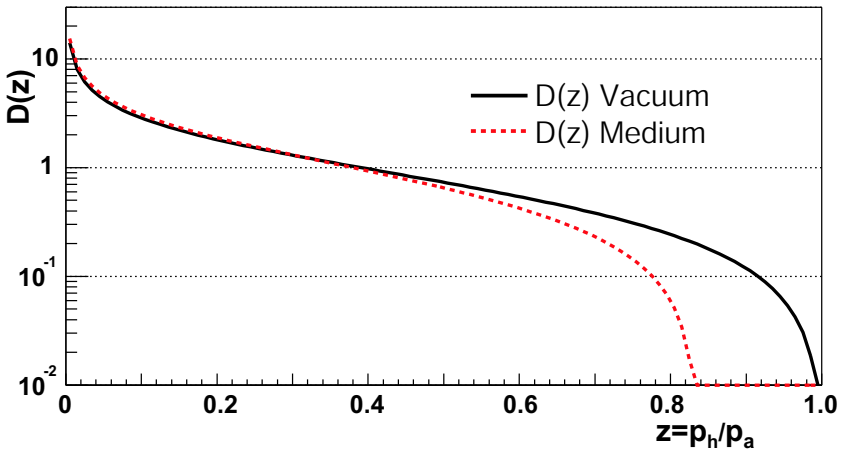

Figure 7.5: Illustration of modified FF assuming $\Delta z = 0$ (solid line) and $\Delta z \simeq 0.2$ (dashed line). The modified FF is noticeably softer. See text for details.

[9]Binnewies, Kniehl, and Kramer

This effectively leads to increased fragment multiplicity at characteristically lower $p_\perp$ values.

Final state energy loss has recently been studied in semi-inclusive DIS of electrons on nuclear targets by the HERMES[10] collaboration. If hadronic rescattering or absorption were responsible for jet quenching, it would most likely be present in DIS as well, where hard-scattered quarks traverse cold nuclear matter. Fig. 7.6a shows the ratio of FFs measured in DIS on nuclear targets (A) and deuterium targets (d). The ratio $R_{DIS} \equiv D_A(z,Q^2)/D_d(Z,Q^2)$ is plotted vs the kinematic variable ν, which is proportional to the outgoing quark energy. One sees a target-dependent suppression

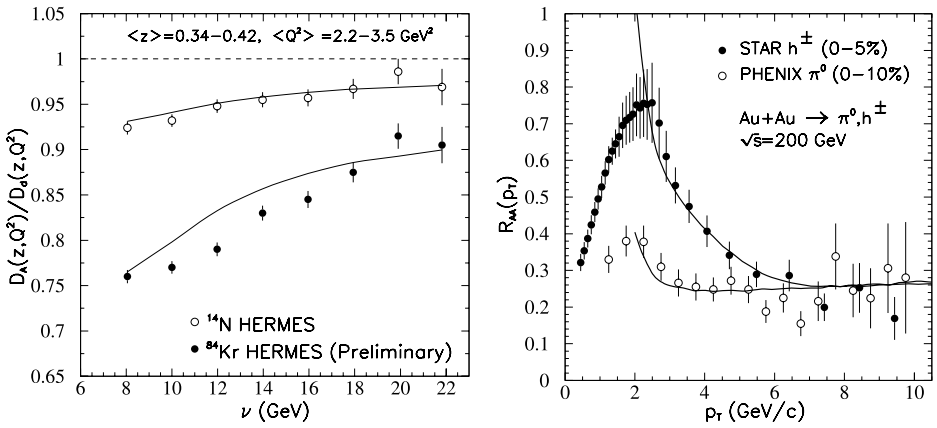

Figure 7.6: The suppression factor for (a) deeply inelastic scattering off nuclear targets and (b) single inclusive hadron spectra in central Au+Au collisions. Data are from PHENIX [75] [23], STAR [76] [77] and HERMES [78] [79]. Figure and caption taken from Ref. [20].

($R < 1$) that decreases as the outgoing quark momentum increases. Fig. 7.6b shows the suppression factor R_{AA} as measured in central Au+Au collisions at RHIC. A flat suppression of an approximate factor of five is seen for $p_\perp > 6$ GeV/c in both the π^0 and inclusive hadron data. Fig. 7.6 also shows Wang's calculations. The model calculations in DIS are identical to those in Au+Au, with two exceptions: (i) different initial gluon densities for the medium and (ii) gluon absorption is only incorporated in the Au+Au calculation. The calculations agree well with both the RHIC and DIS

[10]HERa MEasurement of Spin

data, although the HERMES data can also be explained by hadron absorption after a short formation time [80]. In the Wang calculation, the different energy dependence in the DIS and Au+Au data are "explained by the effect of absorption of thermal gluons from a thermal bath, which only exists in heavy ion collisions but is absent in DIS [20]."

We have already seen that the magnitude of partonic energy loss depends on the size of the medium. By selecting different centralities, one essentially selects mediums of different sizes. Fig. 7.7 shows the centrality dependence of R_{AA} as measured in STAR and predictions from the Wang model. Theory curves are shown with and

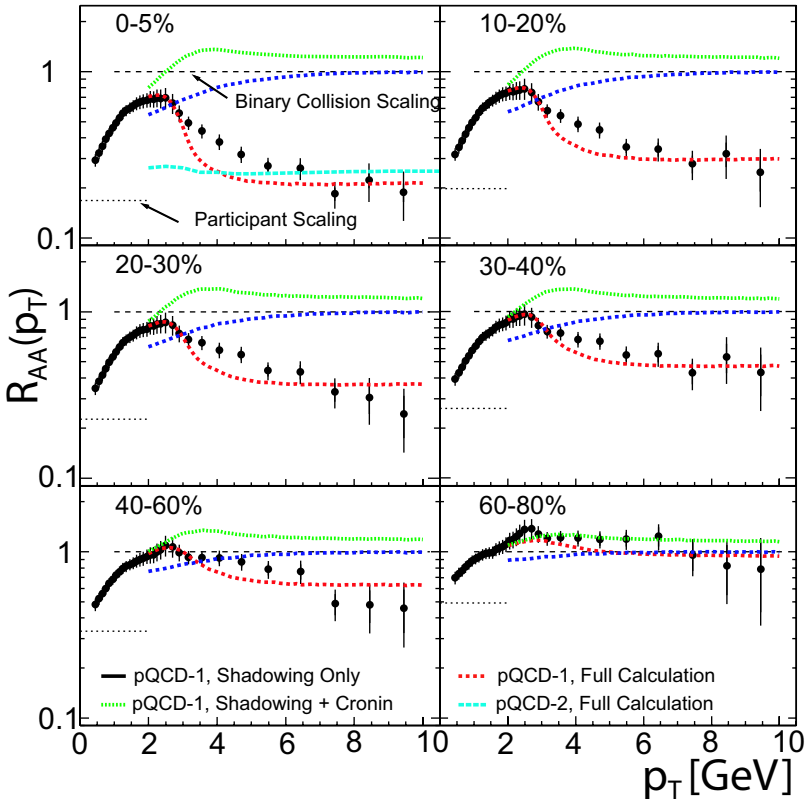

Figure 7.7: The centrality dependence of the measured single inclusive hadron suppression at high-$p_\perp$ compared to model predictions incorporating parton energy loss. Calculations from Wang (pQCD 1) and Vitev (pQCD 2) compared to STAR data. Figure taken from Ref [77].

without energy loss, and also for different parameterizations of the PDF shadowing.

In the absence of energy loss, the theory predicts a value of $R_{AA} \sim 1$ for $p_\perp > 2$ GeV/c for all centralities, while the inclusion of energy loss is in agreement with the data for all centralities. It is important to note that the initial gluon density ρ_0, which cannot yet be calculated, was fixed by the central data. Once fixed, however, the centrality dependence evolves naturally within the model. Fig. 7.8 shows calculations of back-to-back di-hadron correlations compared to the background subtracted STAR p+p and Au+Au two-particle correlation measure $C_2(\Delta\phi)$. We note that Fig 7.8

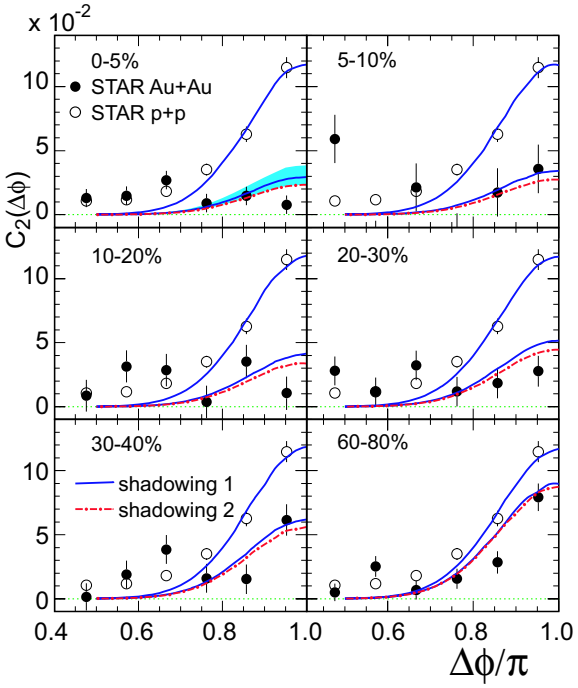

Figure 7.8: The centrality dependent suppression of back-to-back correlations from charged hadrons with 2 GeV/c $< p_\perp < p_\perp^{trig}$, $p_\perp^{trig} = 4 - 6$ GeV/c and $|y| < 0.7$ in Au+Au (lower curves) and p+p (upper curves) collisions. The STAR data are compared to model predictions from Wang incorporating parton energy loss. Figure taken from Ref [70].

also demonstrates that shadowing does not have a significant effect on the $C_2(\Delta\phi)$ measurement. The model calculations are in excellent agreement with the p+p data and further describe the simultaneous centrality dependent suppression of R_{AA} and the away-side di-hadron peak in Au+Au.

In a perturbative calculation like Wang's, one can directly calculate the energy relation between a leading hadron of $p_\perp^{trig}$ and the energy of its "parent" parton, which he calls $E_\perp^{jet}$ [11]. Fig. 7.9a plots $\langle E_\perp^{jet}\rangle - p_\perp^{trig}$ as a function of the centrality measure N_{part}. Calculations with and without energy loss are shown, and the curves converge

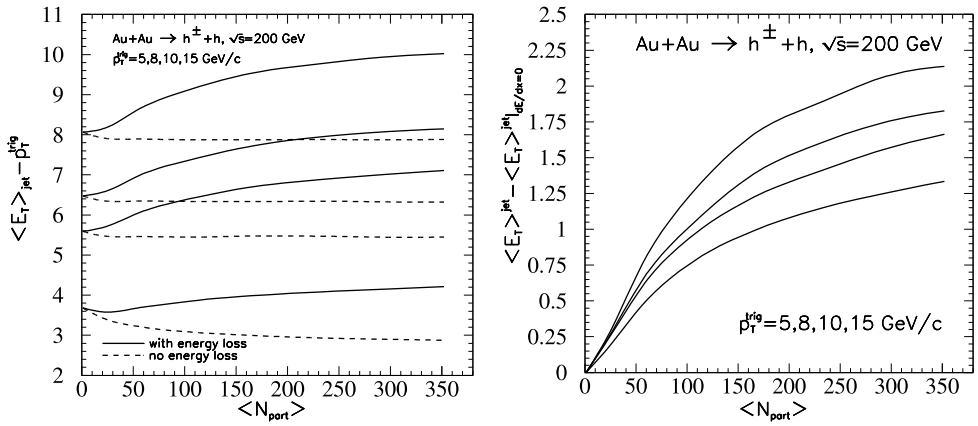

(a) **(b)**

Figure 7.9: (a) Centrality dependence of $\langle E_\perp^{jet}\rangle - p_\perp^{trig}$ from Wang analysis for $p_\perp^{trig}$= 5, 8, 10, and 15 GeV/c, from top to bottom. Dashed curves represent the results with energy loss turned off in the calculation. (b) Wang prediction for the average energy loss for partons that produce a final hadron with $p_\perp^{trig}$ in Au+Au collisions. $p_\perp^{trig}$ increases from bottom to top. Figures taken from Ref. [70]

at $N_{part} = 0$, where $\Delta E \to 0$. The STAR p+p data ($N_{part} = 2$) from Fig. 6.10a, after an approximate correction of 1.5 for undetected neutral energy (primarily π^0 mesons), can be compared to the calculation in Fig. 7.9a. Using $p_\perp^{trig}$= 5 GeV/c and $\langle z_{charge}\rangle$ ≈0.85, we find $\langle E_\perp^{jet}\rangle - p_\perp^{trig} \approx 3.8$, which is in approximate agreement with the prediction.

In heavy ion collisions, an outgoing parton loses energy before it hadronizes. Therefore, it must have a larger pre-fragmentation energy than in a p+p collision in order to produce a leading hadron with the same $p_\perp^{trig}$ [70]. This increased energy is responsible for the rise with increasing N_{part} shown in Fig. 7.9a. The difference

[11] Wang uses "jet" synonymously with parton. This is perhaps based on the prediction that induced gluon radiation does not change the total reconstructed jet energy.

between the solid and dashed lines is then the mean energy loss for a parton that experienced radiative energy loss and multiple scatterings to produce a leading hadron with momentum $p_{\perp}^{trig}$. This is shown in Fig. 7.9b as a function of the centrality measure N_{part}. For $N_{part} \simeq 340$, corresponding to the 0-5% central event class, we find that a leading hadron of $p_{\perp}^{trig} = 5$ (12) GeV/c is a fragmentation product of a parton that suffered a mean energy loss of 1.3 (2.2) GeV.

7.3.4 Theory Comparison: Conclusions

By comparing these theoretical models to the data, we conclude that the suppression of back-to-back di-hadron pairs in central Au+Au collisions can be described by perturbative calculations that incorporate $p_{\perp}$ broadening (in vacuum and nuclear matter) and induced gluon radiation. The same calculations are consistent with results from d+Au collisions and semi-inclusive DIS, where one tests the influence of cold-nuclear matter. Further, partonic- and nuclear-k_T alone are not sufficient to explain the magnitude of the suppression of the back-to-back correlation peak. In the framework of these perturbative analyses, significant partonic energy loss and large gluon densities are needed to describe the data. In the most central Au+Au collisions, partons that produce a leading hadron of $p_{\perp}^{trig}$ =5-15 GeV/c lose approximately 1.4-2.2 GeV of energy to induced gluon radiation [20] as they interact strongly with a dense medium that has an initial energy density of $\sim$20 GeV/fm^3, more than 100 times the $\sim$0.14 GeV/fm^3 density of cold nuclear matter [19].

However, good science is more than testing for *consistency* of model predictions with data. Rather, it is the active, non-ceasing attempt at falsification that draws the most sensitive predictions from competing hypotheses. The question of whether hadronic energy loss could also explain the data is still open. It is the author's opinion that definitive closure of this issue will involve testing sensitive predictions of both models. Empowered by the successful formalism of perturbative QCD, the partonic energy loss calculations are significantly more advanced. It will most likely require additional rigorous calculations within the framework of hadronic interaction theories to produce predictions of similar scope. In the next section, we briefly introduce future

directions that could potentially be useful in settling this issue.

7.4 Future Directions

The analysis presented here is the first attempt to search for modifications to jet structure and fragmentation in central Au+Au collisions. Due to the large combinatorial background and elliptic flow, the analysis was limited to the region $p_\perp > 2$ GeV/c. Calculations incorporating induced gluon radiation predict an effective "softening" of the FF. In the absence of background, one would ideally reconstruct the full jet in central Au+Au and p+p collisions. The $p_\perp$-dependent yield of reconstructed jets should be nearly identical in Au+Au and N_{coll}-scaled p+p data, as most of the emitted gluons should fall within the jet cone. However, the jets resulting from partons suffering induced gluon energy loss should be characterized by larger than average multiplicities and fragmentation products of characteristically smaller $\langle z \rangle$. Due to the color charge factor $C_A/C_F = 2.25$, these effects are predicted to be even larger for gluon jets [15].

These predictions are specific and most likely different than those from a hadronic energy loss scenario where collisional energy loss, not gluon bremsstrahlung, is the dominant mechanism [59]. Due to the large backgrounds in central Au+Au collisions, this analysis was forced to "live on the tails" of the steeply falling FF and was largely insensitive to several of the aforementioned predictions. The suppression of the away-side correlation peak *is* consistent with a suppression of high-z fragments. However, sensitivity to enhancement of low-z fragments was lost due to the 2 GeV/c threshold that was necessary to identify a clear jet signal in central Au+Au. Several possibilities exist to overcome this obstacle. The completion of the STAR calorimeter will allow triggered data sets with enhanced yields of jets, greatly extending both the $p_\perp$ reach ($p_\perp <\sim 50$ GeV/c) and the jet reconstruction abilities. From these data sets, one hopes to measure modifications to the fragmentation function for $z >\sim 0.2$. This, however, is potentially several years away.

Alternatively, one can perhaps identify a reasonable approximation to the true FF. Various alternatives have been proposed to measure the FF without topologically

reconstructing the entire jet. It was originally proposed to use photon-jet events, where the tagged energy of the photon is approximately equal to the entire energy of the recoil jet. Thus, one can measure the FF by measuring the $p_\perp$ distribution in a cone recoiling against the photon. This can be done without actually topologically tagging this away-side jet. Large experimental backgrounds have to date prevented this measurement. However, there has been a revival of the concept of a "hadron triggered" FF (which dates to the pre-QCD studies of Feynman, Field, and Fox) where the role of the photon is replaced by the leading hadron in the event with momentum $p_\perp^{trig}$. One histograms the fractional energy distribution ($z_T \equiv p_\perp / p_\perp^{trig}$) in a cone on the away-side of the trigger particle. Perturbatively, the hadron triggered FF can be calculated as

$$D^{h_1 h_2}(z_T, \phi, p_\perp^{trig}) = \frac{d\sigma^{h_1 h_2} dp_\perp d\phi}{d\sigma^{h_1}/d^2 p_\perp^{trig}}. \tag{7.7}$$

Fig. 7.10a shows predictions from Wang of hadron-triggered FFs for p+p collisions at various values of $p_\perp^{trig}$. The hadron-triggered FFs show the general characteristics

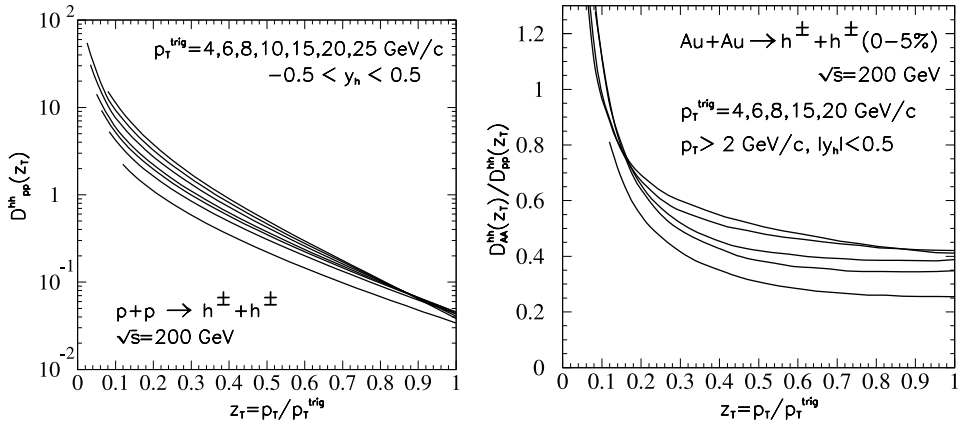

Figure 7.10: (a) Hadron-triggered effective fragmentation function in p+p collisions and (b) medium modification of the hadron-triggered FFs (see Eq. XYZ) from Wang parton model for different values of $p_\perp^{trig}$ (increasing from bottom to top). Figures taken from Ref. [20].

expected of FFs, namely the approximately exponential decrease for $0.2 < z_T < 0.7$.

The dependence on $p_{\perp}^{trig}$ is primarily due to the Q^2 dependence of the QCD evolution. Fig. 7.10b shows the ratio of the hadron-triggered FF calculated in central Au+Au collisions to that calculated in p+p collisions ($D^{hh}_{AuAu}(z_T)/D^{hh}_{pp}(z_T)$) for different values of $p_{\perp}^{trig}$. The ratio reflects the expectation that partonic energy loss softens the fragmentation function, yielding a suppression of high-z particles and an enhancement of low-z particles in Au+Au collisions with respect to p+p collisions. Both the curvature and high-z value of the ratio are sensitive to the magnitude of partonic energy loss. Additionally, a large fraction of the QCD scale dependence seen in Fig. 7.10a is cancelled by taking the ratio of Au+Au to p+p. These measurements should be attainable using data from the long RHIC Au+Au run beginning in winter 2004, and we hope they help differentiate between models of partonic energy loss and hadronic energy loss.

7.5 Final Remarks

We provide here the first study of jets in p+p collisions at RHIC using topological jet reconstruction of charged particles. The tools developed will form the basis of the STAR jet physics program. Using angular correlations of high-$p_{\perp}$ di-hadron pairs, we also provide the first ever direct observation of jets in heavy ion collisions. Jet fragmentation to charged hadrons is then studied in Au+Au collisions as a function of impact parameter. The background-subtracted yield of small-angle high-$p_{\perp}$ di-hadron pairs in Au+Au collisions is consistent with that measured in p+p collisions in the same detector. However, a strong centrality dependent suppression of large-angle pairs is found in the Au+Au data. This suppression is largest in the most violent Au+Au collisions, and no similar phenomenon was found at the lower energies of the CERN SPS. These results must be interpreted in combination with the previously measured suppression of the inclusive charged hadron and identified π^0 high-$p_{\perp}$ spectra. Fig. 7.11 shows the centrality dependence of the asymptotic value R_{AA} in the flat region, the small-angle di-hadron correlations, and the large-angle di-hadron correlations. In the most central collisions, a factor of $\sim$4-5 suppression is found for both charged hadron and π^0 meson R_{AA} values. Using the additional information provided

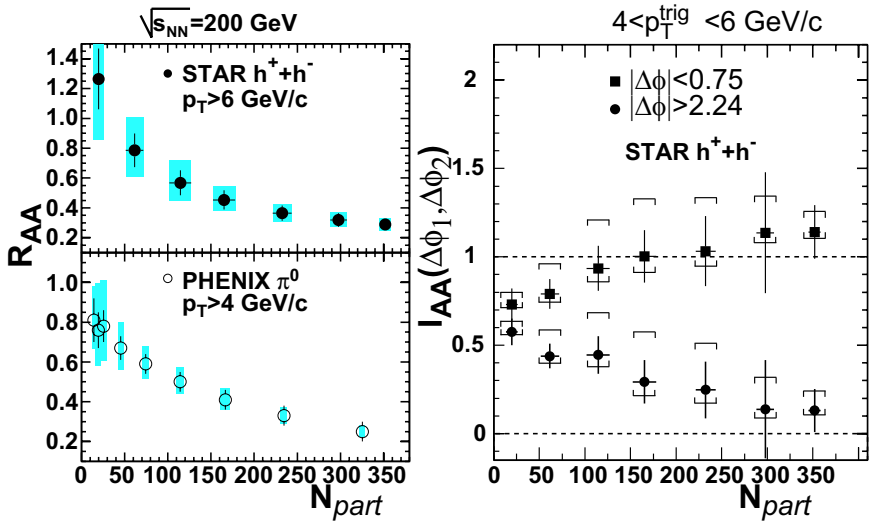

Figure 7.11: Centrality dependence of (left) R_{AA} and (right) I_{AA} at RHIC. The asymptotic value of R_{AA} is plotted for the high-$p_\perp$ region where the R_{AA} value is independent of $p_\perp$[20] [81].

by the di-hadron measure, we conclude that this suppression occurs primarily on the away-side of a detected jet. These data are consistent with perturbative calculations incorporating induced gluon radiation, and (when combined with recent d+Au data) inconsistent with calculations from the gluon saturation model. Calculations incorporating partonic energy loss require an initial energy density of $\sim$20 GeV/fm^3, more than 100 times the density of cold nuclear matter. Combined with the large measured elliptic flow, which is indicative of strong interactions in the medium at very early time scales, this is suggestive of the formation of a novel, deconfined state of quark-gluon matter. However, further studies, both experimental and theoretical, are necessary to exclude models of hadronic energy loss.

Appendix A

Reconstructing Initial State Parton Kinematics

Consider a 2→2 hard scattering where the initial two partons are bound in the incoming hadron beams of symmetric energy $\sqrt{s_{\rm NN}}$. We choose the z axis parallel to the beam. We take all rest masses to be negligible, and we additionally take the intrinsic transverse momentum of the incoming partons k_T to be zero. Parton *1* collides with parton *2*, giving rise to outgoing particles *3* and *4*. Each incoming parton i has a longitudinal momentum fraction $x_{Bjorken} = x_i = \frac{p_i}{p_{hadron}}$. Our goal is to reconstruct the values x_1 and x_2 from final state measurments. Before the collision we thus have

$$p_1^\mu = \left(x_1\frac{\sqrt{s}}{2}, 0, x_1\frac{\sqrt{s}}{2}\right), \quad p_2^\mu = \left(x_2\frac{\sqrt{s}}{2}, 0, -x_2\frac{\sqrt{s}}{2}\right) \tag{A.1}$$

After the collision we have

$$p_3^\mu = (p_{03}, p_{\perp 3}, p_{z3}), \quad p_4^\mu = (p_{04}, p_{\perp 4}, p_{z4}) \tag{A.2}$$

with $p_{0i}^2 = p_{zi}^2 + p_{\perp i}^2$. Energy and momentum conservation yield

$$\frac{\sqrt{s}}{2}(x_1 + x_2) = p_{03} + p_{04} \tag{A.3}$$

and

$$\frac{\sqrt{s}}{2}(x_1 - x_2) = p_{z3} + p_{z4} \tag{A.4}$$

Introducing the rapidity variable

$$y \equiv \frac{1}{2}\ln\left(\frac{p_0 + p_z}{p_0 - p_z}\right) \tag{A.5}$$

and using the relations

$$e^y = \sqrt{\frac{p_0 + p_z}{p_0 - p_z}}, \quad e^{-y} = \sqrt{\frac{p_0 - p_z}{p_0 + p_z}} \tag{A.6}$$

we can derive

$$p_{0i} = p_{\perp i}\cosh(y_i), \quad p_{zi} = p_{\perp i}\sinh(y_i) \tag{A.7}$$

We can then rewrite Eqs A.3 and A.4 as

$$\frac{\sqrt{s}}{2}(x_1 + x_2) = p_{\perp 3}\cosh(y_3) + p_{\perp 4}\cosh(y_4) \tag{A.8}$$

and

$$\frac{\sqrt{s}}{2}(x_1 - x_2) = p_{\perp 3}\sinh(y_3) + p_{\perp 4}\sinh(y_4) \tag{A.9}$$

By adding Eqs A.8 and A.9 and rearranging we find

$$x_1 = \frac{1}{\sqrt{s}}(p_{\perp 3}e^{y_3} + p_{\perp 4}e^{-y_4}) \tag{A.10}$$

Subtracting Eqs A.9 from A.8 and rearranging yields

$$x_2 = \frac{1}{\sqrt{s}}(p_{\perp 3}e^{-y_3} + p_{\perp 4}e^{y_4}) \tag{A.11}$$

Consider Drell-Yan production via $p + \overline{p} \rightarrow e^+ + e^-$. Transverse momentum conservation yields $p_{\perp e^+} = p_{\perp e^-} \equiv p_\perp$, implying

$$x_{1,2} = \frac{p_\perp}{\sqrt{s}}(e^{\pm y_3} + e^{\mp y_4}) \tag{A.12}$$

For scattering at $\theta = 90^\circ,\ y_3 = y_4 = 0$ yielding

$$x_1 = x_2 = x_T \equiv \frac{2p_\perp}{\sqrt{s}} \tag{A.13}$$

We believe this to be the often quoted, rarely explained, source of the statement $x_{Bjorken} \approx x_T = 2p_\perp/\sqrt{s}$.

Appendix B

QCD Color Charge Factors

Here we briefly present the origin of the QCD color charge factors. We follow the derivation from Ref. [4], although it is presented in nearly all QCD texts. In QCD the gluon is associated with a color charge $C_A = 3$ and the quark with a charge $C_F = 4/3$. These factors are derived from the N_c-dimensional fundamental representation (F) and the $N_c^2 - 1$ -dimensional adjoint representation (A) of the group $SU(N_c)$. For representation R, one can choose $SU(N_c)$ generators that satisfy the condition

$$\mathrm{Tr}[T_a^{(R)} T_b^{(R)}] = T(R)\delta_{ab} \tag{B.1}$$

where $T(R)$ is a number that is characteristic of the representation. Each representation has an associated invariant, $C_2(R)$, defined by

$$\sum_{n=1}^{N_c^2-1} (T_a^{(R)})^2 = C_2(R) I \tag{B.2}$$

where I is the identity matrix. The Lie algebra is then defined by the commutation relations of the $SU(N_c)$ structure constants C_{abc}, where $a, b, c = 1...N_c^2 - 1$. The commutation relations are

$$[T_a^{(F)}, T_b^{(F)}] = i C_{abc} T_c^{(F)} \tag{B.3}$$

The generators $T_a^{(F)}$ are a complete set of $N_c^2 - 1$ matrices of dimension $N_c \times N_c$ that are traceless and hermitian. The generators $T_a^{(A)}$ are defined by the structure constants C_{abc} as

$$(T_a^{(A)})_{bc} = -i C_{abc} \tag{B.4}$$

The relevant constants for the fundamental representation are then given by

$$T(F) = \frac{1}{2}, \quad C_2(F) = \frac{N_c^2 - 1}{2N_c} \tag{B.5}$$

and the relevant constants for the adjoint representation are given by

$$T(A) = N_c, \quad C_2(A) = N_c. \tag{B.6}$$

One generally finds the notation $C_A \equiv C_2(A)$ and $C_F \equiv C_2(F)$. For $N_c = 3$, we have $C_A = 3$ and C_F=4/3, and we thus understand the origin of the ratio $C_A/C_F = 9/4 = 2.25$, which is ubiquitous in QCD.

Appendix C

The Landau Pomeranchuk Midgal Effect

The Landau Pomeranchuk Midgal Effect (LPM) [82] [83] exemplifies the critical role of coherence in various QED and QCD phenomena. We provide here a brief introduction, beginning with the QED case. In the 1950's, LPM predicted that the QED bremsstrahlung cross section for relativistic particles in dense media is suppressed (with respect to the Bethe-Heitler prediction) due to interference between amplitudes of nearby interactions. The suppression is fundamentally rooted in the uncertainty principle ($\Delta x \Delta p \sim \hbar$). The bremsstrahlung kinematics require the longitudinal momentum transfer between the nucleus and the electron to be small, thus requiring that the interaction occur over a large longitudinal distance scale. This distance, often called the "formation length", can be interpreted as the distance required for the electron and photon to reach sufficient separation to be considered distinct particles. If the electron Coulomb scatters while traversing this zone, the bremsstrahlung amplitude from before and after the scattering interfere, conspiring to reduce the amplitude for bremsstrahlung photon emission. Specifically, the photon radiation intensity per unit length in the Bethe-Heitler and LPM calculations is given by

$$\omega \frac{dI_{BH}}{d\omega dz} \sim \frac{\alpha}{\lambda}; \qquad \omega \frac{dI_{LPM}}{d\omega dz} \sim \frac{\alpha}{\lambda} \cdot \sqrt{\frac{\omega}{E^2} E_{LPM}}; \qquad \frac{\omega}{E} < \frac{E}{E_{LPM}} \tag{C.1}$$

Here E is the energy of the projectile, and E_{LPM} is the energy scale of the problem and is composed of quantities characterizing the medium:

- λ: mean free path of the electron
- μ: typical momentum transfer in a single scattering (of the order of the inverse

radius of the scattering potential)

This yields $E_{LPM} = \lambda\mu^2 \sim 10^4$ GeV, a large value, perhaps contributing to the fact that the LPM effect was not experimentally verified until 1995 [84][85]. The energy loss per unit length results from integrating C.1

$$-\frac{dE^{QED}}{dz} \sim \frac{\alpha}{\lambda}\sqrt{EE_{LPM}} \tag{C.2}$$

Fig. C.1a shows a comparison of the BH and LPM for the bremsstrahlung cross sections of 25 GeV electrons on a uranium target. At k = 10 MeV, $kd\sigma_{BH}/dk \approx$

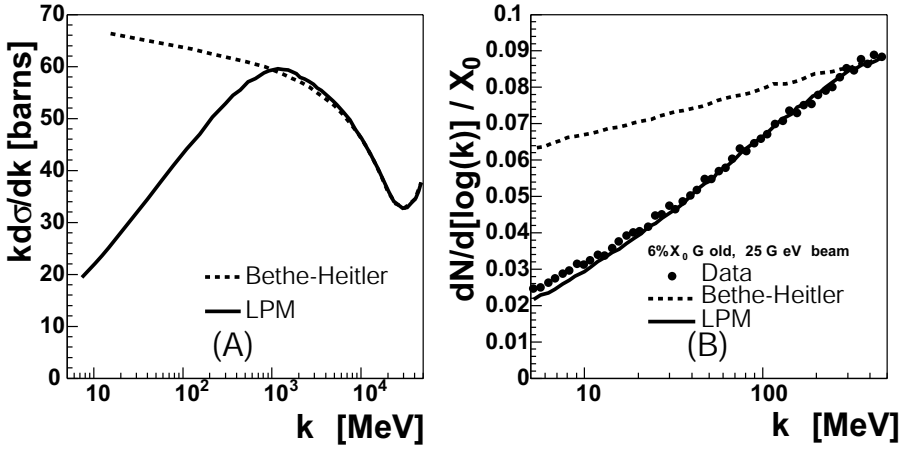

Figure C.1: (A) Comparison of $kd\sigma_{LPM}/dk$ and $kd\sigma_{BH}/dk$ for 25 GeV electrons incident on a uranium target. The cross sections are not corrected for edge effects. (B) Measurement of $dN/d(\log k)$ compared with calculated theoretical curves for 25 GeV electrons incident on 6% X_0 Gold. Statistical error bars are smaller than the data points. The cross sections are given in terms of $dN/[d(\log k)/X_0]$, where N is the number of events per photon energy bin per incident electron. Reproduced from Ref. [84].

$3 \times kd\sigma_{BH}/dk$, clearly a significant effect. Fig. C.1b shows a comparison of data with the BH and LPM predictions for a 25 GeV electron beam incident on a 6% X_0 Gold target. The data clearly follow the LPM prediction, with the slight deviation at low k due to edge effects in the material.

Let us now make the connection to QCD. From Eq. C.1 we find that the LPM effect *suppresses* induced radiation, and that a group of N_{coh} scattering centers acts

as a single source of radiation. We can rewrite Eq. C.1 as

$$\omega\frac{dI_{LPM}}{d\omega dz} = \omega\frac{dI_{BH}}{d\omega dz}\cdot\frac{1}{N_{coh}^{QED}}; \qquad N_{coh}^{QED} = \sqrt{\frac{E^2}{\omega E_{LPM}}} > 1 \tag{C.3}$$

Rigorous and detailed QCD calculations of the LPM effect yield the simple and astonishing result that the QCD spectrum can be obtained from the QED spectrum via the simple reciprocity relation $\omega/E \Rightarrow E/\omega$, yielding

$$\omega\frac{dI_{LPM}^{QCD}}{d\omega dz} \sim \frac{\alpha_s}{\lambda}\cdot\frac{1}{N_{coh}^{QCD}} = \frac{\alpha_s}{\lambda}\sqrt{\frac{E_{LPM}^{QCD}}{\omega}} = \qquad \omega > E_{LPM}^{QCD} \tag{C.4}$$

where E_{LPM}^{QCD} is of order 1 GeV. For a complete derivation, see Ref. [7]. The essential message here is that quantum mechanics plays a critical role in the physics of multiple interactions, with the results often anti-intuitive and inaccessible from classical considerations alone. Dokshitzer concludes, "The LPM physics sends a warning message: a classical Monte Carlo modelling of intra-nuclear particle multiplication at very high-energies is like robbing banks – tempting but dangerous.[1]" It is rather easy to accept that a quark and bremsstrahlung gluon pair should not be treated as separate particles until time $t < t_{form.}$, implying that one should not treat multiple interaction of secondaries with the medium as independent for $t < t_{form}$. However, it is harder to accept that $t_{form.}$ depends on this interaction, and that it cannot be modelled classically.

The previous discussion has dealt with an infinite medium, but finite size effects are indeed important. For an infinite medium, integration of Eq. C.4 yields $\frac{dE_{LPM}^{QCD}}{dz} \sim \sqrt{E}$, in accordance with the QED result given in Eq. C.2. Finite size effects change the QCD prediction. The LPM formalism essentially slices the medium into groups of N_{coh} scattering centers, implying that the longitudinal size of the medium (L) is large enough to contain at least one such group, i.e., $L > L_{cr}$ where

$$L_{cr} = \sqrt{E\frac{\lambda}{\mu^2}} \tag{C.5}$$

[1]Ref. [7]. This warning will be revisited in Sec. 7

For $L < L_{cr}$, the finite size effects conspire to make the induced gluon energy L-dependent, and one finds the energy loss per unit length to be proportional to the *size of the medium*, instead of $\sqrt{E}$, and integrating over z leads to the total loss growing as L^2, a purely coherent enhancement. The full prediction (for $L < L_{cr}$) given in Ref. [7] is

$$-\frac{dE^{QCD}_{LPM}}{dz} = \frac{\alpha_s(B^2)N_c}{8}\frac{\mu^2\tilde{v}(B^2)}{\lambda}\cdot L \tag{C.6}$$

where B is the impact parameter inversely proportional to the accumulated gluon transverse momentum $k_\perp$, with $B^2 \ll (1\text{ fm})^2$. The dimensionless factor $\tilde{v}$ characterizes the scattering potential of the medium and is thus sensitive to the color charge density (*gluon density*).

We can now establish the influence of parton energy loss on a measurement. Consider the inclusive single particle cross section $d\sigma(p_\perp)/dp^2_\perp$. In medium, one must convolute the production cross section of the parton of energy $p_\perp + \epsilon$ with the distribution $D(\epsilon)$ in the parton energy loss ϵ in the final state:

$$\frac{d\sigma^{medium}(p_\perp)}{dp^2_\perp} = \int d\epsilon D(\epsilon)\frac{d\sigma^{vacuum}(p_\perp+\epsilon)}{dp^2_\perp} \tag{C.7}$$

The distribution $D(\epsilon)$ describes the energy loss due to medium induced gluon energy. The relation between the in-medium and vacuum cross sections is given by

$$\frac{d\sigma^{medium}(p_\perp)}{dp\ \perp^2} = \frac{d\sigma^{vacuum}(p_\perp + S(p_\perp))}{dp\ \perp^2} = \frac{d\sigma^{vacuum}(p_\perp)}{dp\ \perp^2}\cdot Q(p_\perp) \tag{C.8}$$

where $S(p_\perp)$ is the "shift function" representing the propagation of partons from higher to lower $p_\perp$, and $Q(p_\perp)$ is the "quenching" function. Both approaches exist in the literature, and can be related in certain limits. The BDMPS collaboration calculates $Q(p_\perp)$, showing that it is indeed a CIS quantity. Further, they show that characteristics of the gluon energy spectrum yield $S(p_\perp) \sim \sqrt{p_\perp}$.

Appendix D

STAR Jet Finding Software

D.1 Introduction

A major fraction of this thesis research was dedicated to defining, implementing, debugging, and running the jet finding algorithms discussed in chapter 4. For reference purposes, we here summarize the structure design and program flow of this software. The guiding principles of the software design are listed below.

The software should

1. Provide a common user interface for jet finder I/O that does not depend on the actual algorithm applied
2. Implement both the k_T and cone jet finding algorithm, but also allow for natural implementation of other algorithms
3. Be CPU[1] efficient and memory conscious
4. Be written in object oriented, portable c++ that depends only on ansi standard libraries.

To meet these criteria a new c++ STAR software library was created StRoot/`StJetFinder`. Below we briefly describe this library and its relation to the aforementioned design criteria.

[1] Central Processing Unit

D.2 Input/Output Specification and Work Objects

To begin, the concept of proto-jet and four-vector are used to define both the input and output of the jet finder. The jet finding algorithm should not depend on the detector subsystem(s) that are providing the information. Thus, we abstract the output of a single measurement as a class `AbstractFourVec`, which simply encapsulates

1. the information stored by a covariant four-vector p^{μ}
2. the c++ functionality expected by a covariant four-vector, e.g., $p_T(), phi(), e_T()$, etc.

As its name suggests, `AbstractFourVec` is a pure-virtual class. The information of an actual charged track measurement is encapsulated in the publicly derived class `StMuTrackFourVec`. `StMuTrackFourVec` simply wraps the measurement data stored in `StMuTrack` to conform to the interface imposed by `AbstractFourVec`. Thus, each of the momenta measurements in an event is encapsulated as an individual `AbstractFourVec` object.

Next, the concept of proto-jet is encapsulated in the class `StProtoJet`. A proto-jet is simply a collection of one or more four-vectors. The class `StProtoJet` thus stores a collection of `AbstractFourVec` pointers, and `StProtoJet` is responsible for encapsulating the sum momenta of the collection of `AbstractFourVec` objects. `AbstractFourVec` objects can be added or removed from a `StProtoJet` object. Further, there is no loss of information in the clustering process. That is, one can still retrieve the the individual charged tracks from `StProtoJet`.

It is assumed that the jet finding algorithm will operate strictly on a collection of `StProtoJet` objects. However, `StProtoJet` actually inherits from `AbstractFourVec` while storing a collection of `AbstractFourVec` objects, thus establishing a one-to-many relationship with a common interface. Additionally, two `StProtoJet` objects can be merged. Thus, jet finding proceeds by first creating `StProtoJet` objects, passing them to the jet finder, clustering `StProtoJet` objects, and then retrieving them from the jet finder.

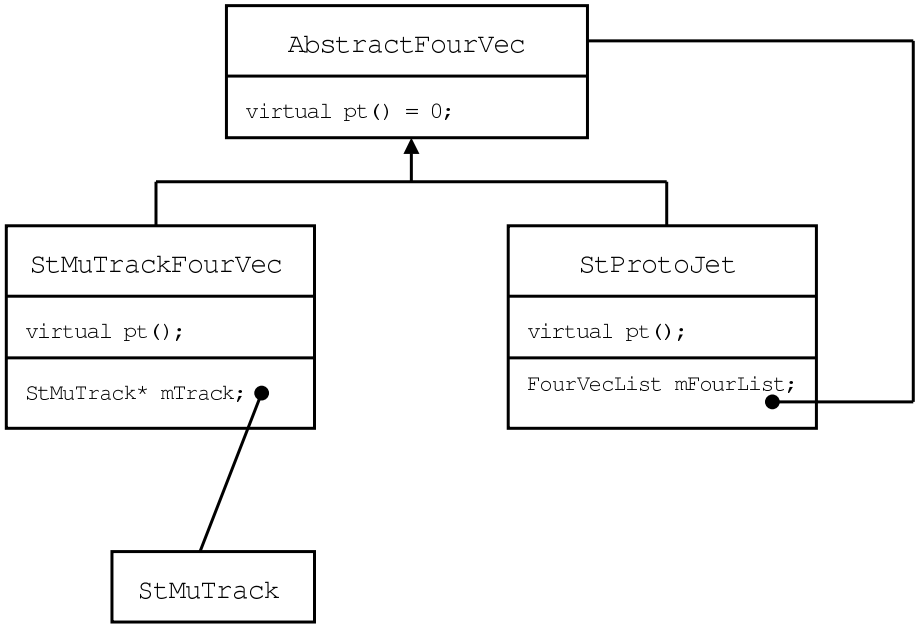

Figure D.1: A class diagram that encapsulates four-momenta.

D.3 StJetFinder

To provide a common interface for all jet finding algorithms, we create the abstract class `StJetFinder`. `StJetFinder` has a single abstract function called $findJets$. This method is implemented by any of the derived classes, where each derived class implements a specific algorithm (k_T, cone, etc). The proto-jets are unpacked from the container, clustered, and the results are re-packed into the same container. Thus, the caller of $findJets$ is responsible for separating the proto-jet list into jets and beam-jets by some criteria (namely, $E_{T\ jet}$). Currently, there are 3 jet finding algorithms that are implemented: `StKtCluJetFinder`, `StConeJetFinder`, and `StCdfChargedConeJetFinder`. We describe these below.

`StKtCluJetFinder` implements the k_T algorithm. Essentially, `StProtoJet` objects are clustered using the work class `StProtoJetPair`. These proto-jets are then

repacked into the proto-jet container, and the users is responsible for separating the jets from beam-jets. The only control parameter of the algorithm is d_{min} which is of order 1. Increasing d_{min} effectively broadens the search radius of the algorithm.

`StConeJetFinder` is slightly more complicated. `StProtoJet` objects are first sorted into a grid in η *vs.* ϕ space for computational efficiency. There is no true loss of information or granularity in this process. The work class `StJetEtCell` is used for the individual lattice points. `StJetEtCell` simply stores a container of `StProtoJet` objects and returns the scalar sum E_T of all of the `StProtoJet` objects in a given cell. This E_T value is used to identify cells that are above the seed threshold around which clustering can begin. The cone search algorithm then begins and iterates until the jet centroid is equal to the center of the cell. After clustering (and splitting/merging) is finished, the `StProtoJet` content of the cells is unpacked, and all `StProtoJet` objects in a given jet are merged. These `StProtoJet` objects are then repacked in the proto-jet container, and the user is responsible for separating jets from beam jets by the regular criteria.

Additionally, there are switches to turn on/off the inclusion of midpoint seeds and the splitting merging steps. The algorithm then has several control parameters

- R_{cone} The cone radius, generally $\simeq$0.7.
- E_{seed} The threshold above which cells are considered as jet seeds.
- $doMidpoints$ Add seeds at midpoints of all found jets?
- $doSplitMerge$ Execute the splitting/merging routine?
- $f_{split/merge}$ The control fraction of the splitting/merging routine, generally $\simeq$0.5

`StCdfChargedConeJetFinder` is is a very specific cone algorithm that is not CIS at the parton level. It is meant to work in a high-background environment such as d+Au or Au+Au collisions. It is a very basic cone algorithm, where proto-jets are once again sorted into an η vs. ϕ grid. Clustering then proceeds by searching for cones around cells above a seed threshold. However, instead of using the summed E_T of the cell, this algorithm sorts the cells based on the E_T of the most energetic

particle in the cell. Further, no iteration of the jet cone is performed, so the centroid of the final jet must lie within R_{cone} radians from the seed position. These cells are then marked as used, and are removed from the event sample. When clustering ends, the `StProtoJet` objects in a jet are retreived, merged, and repacked in the proto-jet container to be evaluated by the user. Thus, `StCdfChargedConeJetFinder` essentially clusters particles that lie in a cone about energetic single particles in the event. This is useful if the background consists primarily of many low energy particles, such that $E_{jet} \ll \sum E_{background}$. Note that `StCdfChargedConeJetFinder` has no iteration, midpoint addition, or splitting/merging routines.

Appendix E

Centrality Selection and Application of the Glauber Model

E.1 Introduction

In recent theoretical publications [86], [26], [87], [88], [73] the production of hadrons in heavy ion collisions at RHIC has been parameterized as a function depending on the number of participating nucleons N_{part} and the number of binary collisions N_{coll}. Unfortunately, neither N_{part} nor N_{coll} can be measured directly in the experiment and their values can only be derived by mapping the measured data, i.e., the dN/dN_{ch} distributions, to the corresponding distribution obtained from phenomenological calculations, thus relating N_{part} and N_{coll} to the measured dN/dN_{ch} distributions. These type of calculations are generally called Glauber calculations. Fig. E.1 illustrates the correlation of the calculated impact parameter to final state observables such as $N_{charged}$, E_T, and fraction of the measured cross section. Glauber calculations come in two flavors, the optical and the Monte Carlo Glauber calculations. The optical model is based on an analytic consideration of classically overlapping nuclei [86] [89] [90] [91]. The Monte Carlo approach is based on a computer simulation of billiard ball like colliding nucleons [91] [76] [92] [93] [94].

However, as noted in Ref [95], different implementations of the Glauber model, such as the one used in the frequently quoted Kharzeev/Nardi soft+hard collision parameterizations [86] (optical) or in the popular HIJING model (Monte Carlo) [96], lead to slightly different values for N_{part} and N_{coll}, especially for peripheral collisions. Therefore, any results reported in terms of Glauber quantities must be carefully interpreted based upon specifics of the Glauber calculations.

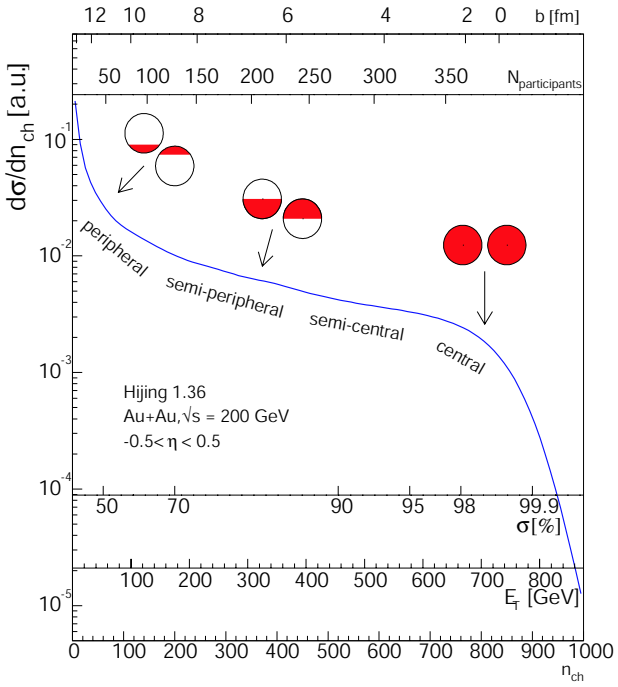

Figure E.1: An example of the correlation of final state observable quantities with Glauber calculated quantities. One measures, e.g., the $N_{charged}$ distribution and calculates the N_{part} distribution. Next one correlates, on a bin-by-bin basis, the mean values of each distribution. Thus, fractions of the total cross section can be mapped to N_{part}, N_{coll}, and b. The figure was taken from Thomas Ullrich, private communications. It is not measured data, but rather intended for illustrative purposes.

In the following sections, we shortly report on the Glauber calculations performed to obtain $\langle N_{coll} \rangle$ and $\langle N_{part} \rangle$ values used in this document and other STAR analyses.

E.2 Basic Glauber Theory

Glauber theory is a catch phrase for a group of approximations that make cross-section calculations in many-body collisions possible. Applied to nucleus-nucleus (AA) collisions, Glauber theory provides a quantitative consideration of the geometrical configuration of the nuclei at the time of collision. Glauber theory is based on the assumptions of

- A characteristic nucleon-nucleon (nn) cross section

- Straight line trajectories of the colliding nucleons

In brief, the complex AA collision is treated as a superposition of many individual nn collisions, each governed by a constant probability of interaction, with all nucleons travelling on constant trajectories. One must only specify a probability distribution for nucleons within the nucleus and a fundamental nn cross section.

E.3 Representation of Nuclei

We must first specify a probability distribution for nucleons in a nucleus. Commonly used approximations are colliding disks, hard spheres, or a more realistic Woods-Saxon distribution. Here we adopt the Woods-Saxon formalism, as this is widely used to characterize measurements of the radial density of charged nucleons in a Au nucleus. The Woods-Saxon distribution is given by

$$\rho(r) = \frac{\rho_0}{1 + exp(\frac{r-r_0}{c})} \tag{E.1}$$

where

- r radial distance from the center of the nucleus
- r_0 mean radius of the nucleus
- c "skindepth" of the nucleus
- ρ_0 nuclear density constant

The first two parameters are well measured in e+Au scattering and the latter is determined by the overall normalization condition

$$\int \rho(r)\ d^3r = A \tag{E.2}$$

where A is the mass number of the nucleus. In general, it is most convenient to change our normalization constraint such that equation E.1 can be treated as a true probability distribution. That is, we reformulate equation E.2 to read

$$\int p(r) d^3r = 1 \tag{E.3}$$

Parameter	Value
ρ_0	0.169346 nucleons/fm^3
r_0	6.5 $\pm$ 0.1 fm
c	0.562 $\pm$ 0.27 fm

Table E.1: Woods-Saxon parameters used for Au nuclei in the Glauber calculation. The value of r_0 was increased from 6.38 fm to 6.5 fm to account for the neutron skin. There is no error assigned to the parameter ρ_0, as it is determined via the normalization condition given by equation E.2.

where

$$p(r) = \frac{1}{A} \cdot \rho(r) \tag{E.4}$$

Let us list the assumptions that are implicit to this Woods-Saxon formalism:

- We assume the nucleus to be spherical and void of deformation.
- We assume the nuclear density profile to be identical for protons and neutrons.
- We use the charge distribution that is experimentally measured in low energy scattering of electrons on Au nuclei.

A useful tool for establishing the systematic uncertainties in the final glauber calculations is to study the dependence of calculation results on the input values, where one can change the input (Woods-Saxon parameters) within the uncertainties. That is, we define three Woods-Saxon classes: small, nominal, and big. The nominal class uses the values quoted in table E.1, and the small (large) class uses smallest (largest) values within the error quoted in table E.1. In figure E.2 we plot the radial integrand (in spherical coordinates) of equation E.2.

E.4 The Optical Glauber Model

In the optical approximation, we can write analytic formulae for the AA collision. Our goal is to write an analytic formulation for the total cross section. To begin, we choose to work in cylindrical coordinates, as shown in Figure E.3. We next introduce

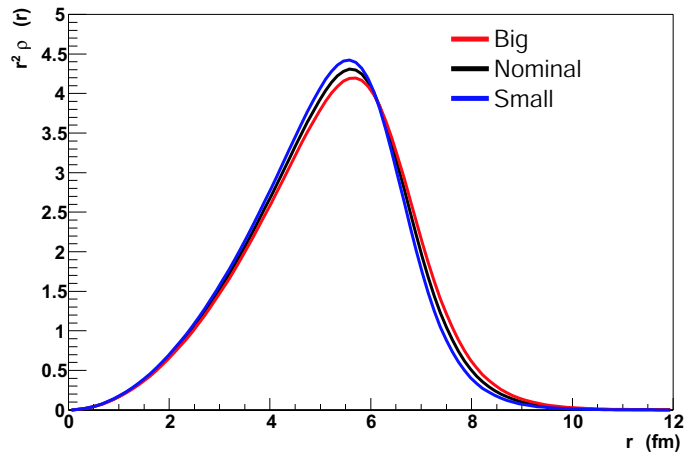

Figure E.2: The Woods-Saxon distributions weighted by the r^2 from the integrand in equation E.2. The middle curve represents the nominal values, while the narrower (wider) curve represents the smallest (largest) limit within the quoted experimental errors.

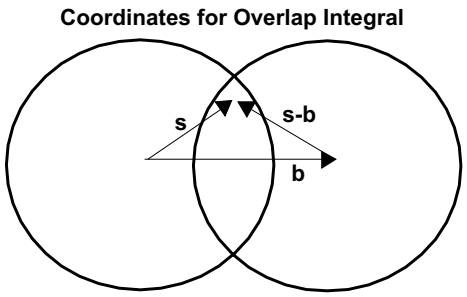

Figure E.3: Schematic of the collision geometry for the calculation of the overlap integral T_{AA} from equation E.6. The area of overlap is the "football" shaped region in the middle of the 2 spheres. The z_1 and z_2 coordinates are perpendicular to the plane of the paper.

the individual thickness function

$$T_A(\vec{s}) = \int p_A(\vec{s}, z_A)\ dz_A \tag{E.5}$$

which represents the properly normalized density element at a given location $\vec{b_A}$ in nucleus A integrated over all z. We can write the same expression for nucleus B, as well. Folding these two probability distributions together, we arrive at what is the

overall thickness function

$$T_{AB}(b) = \int d^2s \; T_A(\vec{s}) \; T_B(\vec{s} - \vec{b}) \tag{E.6}$$

where it is important to remember that the integrand is in cylindrical coordinates. The thickness function represents the probability (normalized to 1) to find a nucleon from *both* nucleus A and nucleus B at a given location. The probability for these two nucleons to interact is given by the non-singly diffractive nn cross section

$$\sigma_{in} = 42 \; (41) \; mb \tag{E.7}$$

at $\sqrt{s}$= 200 (130) GeV. We can then use binomial statistics to write down the probability of n inelastic nn interactions at an impact parameter $\vec{b}$ as

$$P(n, \vec{b}) = \left(\begin{array}{c} AB \\ n \end{array} \right) [T(b)\sigma_{in}^n][1 - T(b)\sigma_{in}]^{AB-n} \tag{E.8}$$

where the first term represents the number of possible configurations yielding n interactions given $A \cdot B$ possible nn encounters, the second term represents the probability of n collisions, and the third term represents the probability of exactly $A \cdot B - n$ misses. We then arrive at an expression for the total probability of an AA interaction between nuclei A and B by summing equation E.8

$$\frac{d\sigma_{in}^{AB}}{d\vec{b}} = \sum_{n=1}^{n=AB} P(n, \vec{b}) = 1 - 1[1 - T(b)\sigma_{in}]^{AB} \tag{E.9}$$

In figure E.4 we plot equation E.9. Finally, we can integrate equation E.9 to obtain the total AA cross section

$$\sigma_{in}^{AB} = \int d\vec{b}\{1 - [1 - T(b)\sigma_{in}]^{AB}\} \tag{E.10}$$

One must remember that the integral is in cylindrical coordinates, explicitly

$$\sigma_{in}^{AB} = \int_0^\infty b \; db\{1 - [1 - T(b)\sigma_{in}]^{AB}\} \tag{E.11}$$

It is worthwhile to mention that equation E.10 represents the best estimate of the (yet unmeasured) Au+Au cross section at RHIC.

Figure E.4: The inelastic differential cross section for Au+Au at $\sqrt{s_{\rm NN}} = 200$ GeV as calculated by the Optical Glauber model using values listed in Table E.1

We can go yet farther and calculated two important geometrical quantities. First, we can establish the total number of billiard ball like nn collisions (N_{coll}) via

$$\langle N_{coll}(b)\rangle = \sum_{n=1}^{n=AB} n\ P(n,b) = A \cdot B \cdot T(b)\sigma_{in} \tag{E.12}$$

Second, we can establish the total number of incoming nucleons that participated in *at least one* inelastic collision ($N_{participant}$ or N_{part})

$$\langle N_{part}(b)\rangle = 2A \int d^2s\ T_{AA}(\vec{s})\{1-(1-T_{AA}(\vec{s}-\vec{b})\sigma_{in})^{A^2}\} \tag{E.13}$$

where we have set $A = B$ for simplicity, although equation E.13 can of course be generalized for $A \neq B$.

To relate $\langle N_{coll}\rangle$ and $\langle N_{part}\rangle$ to an experimental observable, e.g. dN/dN_{ch}, the mean of the total number of charged tracks in our multiplicity classes, we use Equations E.9, E.12, and E.13 to generate the functions $d\sigma/dN_{coll}$ and $d\sigma/dN_{part}$. Mathematically, one must account for the Jacobian in these transformations, which is cumbersome. It is more convenient to use Monte Carlo techniques to calculate $d\sigma/dN_{coll}$ and $d\sigma/dN_{part}$, where the Jacobian is intrinsic to the method. Therefore, we randomly sample the differential cross section (equation E.9) and histogram the values of N_{coll} and N_{part} for each sampling. We then have the distributions $d\sigma/dN_{coll}$ and

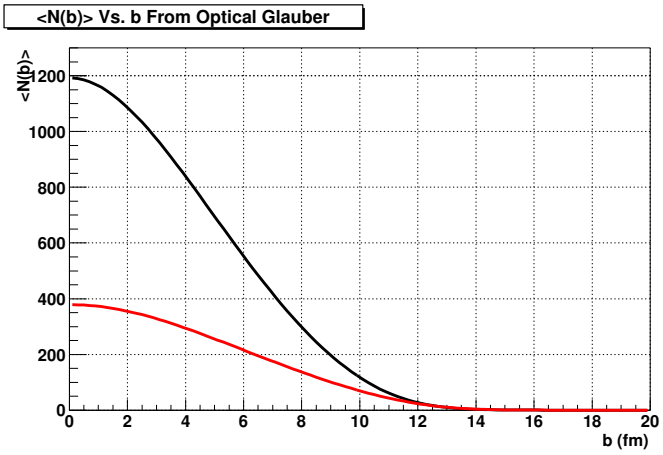

Figure E.5: $\langle N_{coll} \rangle$ and $\langle N_{part} \rangle$ in Au+Au as a function of of impact parameter from the optical Glauber model. The upper (lower) curve shows $\langle N_{coll} \rangle (\langle N_{part} \rangle)$ as a function of impact parameter b.

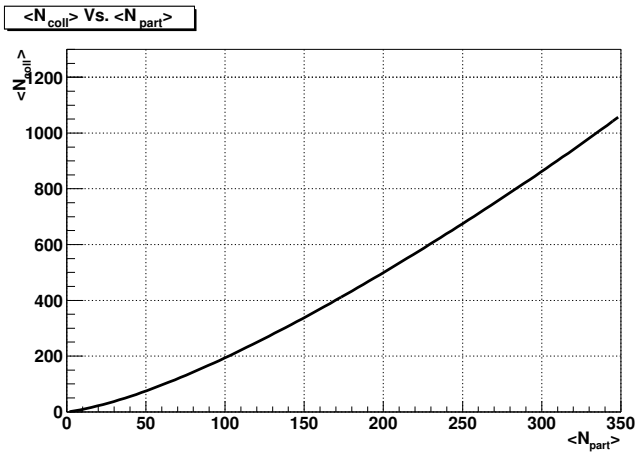

Figure E.6: The correlation between $\langle N_{coll} \rangle$ and $\langle N_{part} \rangle$ for Au+Au collisions from the optical Glauber model. The curve is well described by a power law $\langle N_{coll} \rangle \sim \langle N_{part} \rangle^{4/3}$

$d\sigma/dN_{part}$. Each distribution was divided vertically into bins corresponding to common fractions of the total cross-section, and mean values were then correlated with the independently measured mean values of, e.g., dN/dN_{ch}. Potential biases due to this bin-by-bin evaluation of mean values were investigated and found to be negligible in comparison to the other sources of systematic uncertainties. This method was chosen instead of the example given in [86], which relies upon a specific model of

particle production.

E.5 Monte Carlo Calculations

The Monte Carlo method consists of constructing a set of independently simulated Au+Au interactions. For each interaction, 'A' target nucleons are distributed about the point $(0, 0, 0)$ and 'B' projectile nucleons are distributed about the point $(b, 0, 0)$, where b is the impact parameter of the event. Each of the nucleons is randomly distributed using the Woods-Saxon probability distribution given by equation E.1. We further require that all nucleons in either nucleus be separated by a distance $d \geq d_{min}$, where $d_{min} = 0.4\ fm$ is characteristic of the length of the repulsive nucleon-nucleon force. However, it was found that the total Au+Au cross section, N_{part} and N_{coll} predicted by the Monte Carlo approach did not depend on d_{min} in the range $0 < d_{min} < 0.6$ fm. Thus, d_{min} was set to zero, greatly increasing the speed of the calculations. Next, all possible nucleon-nucleon pairs (with one nucleon each from the target and projectile) are constructed. Each pair is determined to 'interact' if they are separated by the transverse distance

$$r \leq \sqrt{\frac{\sigma_{in}}{\pi}} \tag{E.14}$$

which is derived from the characteristic radius of the nn inelastic cross section, σ_{in}. N_{part} is defined as the total number of nucleons that underwent at least one interaction. N_{coll} is defined as the total number of interactions in the event. This process is iterated for an arbitrary number of events, with the impact parameter b for each event randomly chosen from a flat distribution. Thus, the distributions $d\sigma/dN_{coll}$, $d\sigma/dN_{part}$, and $d\sigma/db$ are determined. Each distribution was divided vertically into bins corresponding to common fractions of the total cross section, and mean values were extracted on a bin-by-bin basis. These mean values were then correlated with the independently measured mean values of, e.g., $d\sigma/dN_{ch}$.

E.6 Systematic Uncertainty Estimates

As already stated, potential biases due to this bin-by-bin evaluation of mean values were investigated and found to be negligible in comparison to the other sources of systematic uncertainties. For both the Optical and Monte Carlo approaches, the systematic uncertainties on $\langle N_{coll} \rangle$ and $\langle N_{part} \rangle$ were determined by varying the Woods-Saxon parameters, by varying the value of σ_{in}, and by including a 5% uncertainty in the determination of the total measured Au+Au cross section. Thus, the contributions from these three sources were determined separately and were treated as fully correlated in the final systematic uncertainties reported. The Woods-Saxon parameters were varied within the uncertainties to yield both the largest and smallest possible density distributions. For the $\sqrt{s}$= 200 (130) GeV calculation, σ_{in} was varied between 41 and 43 (40 and 42) mb. The values of $\langle N_{coll} \rangle$ and $\langle N_{part} \rangle$ were found to depend strongly (30% in the most peripheral bin) on the 5% uncertainty in the total measured Au+Au cross section. This effect was shown to decrease to 1% in the most central bin. The value of $\langle N_{coll} \rangle$ was found to depend (3% in the most central bin) on σ_{in}. This dependence decreased to less than 1% in the most peripheral bin. The uncertainties due to uncertainties in the Woods-Saxon parameters were found to introduce at most a 5% uncertainty on the mapping to $\langle N_{coll} \rangle$ and $\langle N_{part} \rangle$, independent of centrality. Uncertainties due to difference in the mass-density distribution (neutrons) with respect to the measured charge-density distribution (protons) are beyond the scope of this study.

E.7 Application to d+Au Collisions

Glauber model calculations played a critical role in the interpretation of the d+Au data from RHIC RunIII. In principle the formalism for the d+Au system is the same as that for Au+Au. However, the representation of the deuteron wave function is significantly different than the Woods-Saxon density distribution used for Au+Au. We specify the wave function of the dueteron as:

$$\psi_{J_z}(\mathbf{r}) = \frac{u(r)}{r}\Phi_{1J_z0}(\Omega) + \frac{w(r)}{r}\Phi_{1J_z2}(\Omega), \tag{E.15}$$

which contains $S-$ and $D-$wave components. It is important to note that $\mathbf{r}$ represents the relative separation between the proton and neutron. For the radial functions u and w, we use the Hulthen form [97]

$$u(r) = N\sqrt{1-\epsilon^2}[1 - e^{-\beta(\alpha r - x_c)}]e^{-\alpha r}\Theta(\alpha r - x_c) \tag{E.16}$$

$$w(r) = N\epsilon[1 - e^{-\gamma(\alpha r - x_c)}]^2 e^{-\alpha r}\left[1 + \frac{3(1-e^{-\gamma\alpha r})}{\alpha r} + \frac{3(1-e^{-\gamma\alpha r})^2}{(\alpha r)^2}\right]\Theta(\alpha r - x_c) \tag{E.17}$$

$$N^2 \equiv \frac{2\alpha}{1-\alpha\rho} \tag{E.18}$$

where α is derived from the experimental binding energy E_D:

$$\alpha = \sqrt{\frac{ME_D}{h^2}} = [4.316 \text{ fm}]^{-1}, \tag{E.19}$$

the parameters β, γ, ϵ, x_c are fit to experimental data, and ρ is determined by the normalization condition. We used $\beta = 4.680$, $\gamma = 2.494$, $\epsilon = 0.03232$, $x_c = 0$ [97]. For the calculations presented below, only the S wave component of the deuteron (Eq. E.16) was used.

The d+Au calculations were performed only in the Monte Carlo method because (i) implementation of Eq. E.15 in the optical formalism is straight forward but tedious, and (ii) the STAR collaboration has adopted a policy to report all measurements in terms of Monte Carlo Glauber calculations. The distribution of the nucleons in the Au nucleus was performed as previously discussed. For the deuteron, the square of the radial wave function

$$P(r) = |\psi_{J_z}(\mathbf{r})|^2 = \left|\frac{u(r)}{r}\Phi_{1J_z0}(\Omega)\right|^2 \tag{E.20}$$

(weighted by a phase space factor of r^2) was randomly sampled to obtain the value of $\mathbf{r}$. One nucleon was then placed at a radial position $\mathbf{r/2}$, and the other was placed at $-\mathbf{r/2}$. The calculation of N_{coll} and N_{part} then proceeded as usual. Additionally, it was determined that fluctuations in both the Glauber quantities and the charged particle multiplicity significantly biased the mapping between experimental observable (dN/dN_{ch}) and, e.g., $\langle N_{coll}\rangle$. Several solutions were investigated. Ultimately the

best solution was to simulate dN/dN_{ch}. For the d+Au data, multiplicity classes were based on uncorrected dN/dN_{ch} in the region $-2.8 < \eta < -3.8$ (the Au fragmentation region), as measured in the FTPC East. This value was simulated by assuming N_{part} scaling of particle production. Specifically, the dN/dN_{ch} spectra for $p + \bar{p}$ was measured in the region $-2.5 < \eta < -3.5$ by the UA5 collaboration at CERN to be distributed via a negative binomial distribution. The probability to create n charged particles is given by

$$P(n; \overline{n}, k) = \left(\begin{array}{c} n+k-1 \\ k-1 \end{array} \right) \left(\frac{\overline{n}/k}{1+\overline{n}/k} \right)^n \frac{1}{(1+\overline{n}/k)^n} \tag{E.21}$$

where $\overline{n} = 2.14$ and $k = 2.2$. For a d+Au collision with a given value of N_{part}, Eq. E.21 was randomly sampled $0.87 \cdot N_{part}$ times. The prefactor of 0.87 comes from trigger bias considerations. Specifically, the STAR d+Au trigger was sensitive to all inelastic events while the UA5 trigger was sensitive to only non-singly diffractive (NSD) events. The relavant cross sections are given as, $\sigma_{NSD} = 31$ mb, $\sigma_{inelastic} = \sigma_{SD} + \sigma_{NSD} = 42$ mb, and $\sigma_{SD} = 11$ mb. Thus, the scaling pre-factor is given by

$$x_{scale} = \frac{\sigma_{NSD} + \sigma_{SD}/2}{\sigma_{inelastic}} = \frac{31 \ + \ 11/2}{42} = 0.87 \tag{E.22}$$

Additionally, the 83% tracking efficiency of FTPC East was accounted for. Fig. E.7 shows the comparison of the simulated FTPCE multiplicity with that measured in FTPCE. The excellent agreement over three orders of magnitude motivates the choice of the particle production model. The mean values of, e.g., N_{coll}, were derived by cutting on the simulated FTPCE multiplicity. In the Monte Carlo calculation, two additional classes of events were also selected, those where either a single nucleon or both nucleons in the deuteron interacted. These were directly comparable to measured d+Au events where a single spectator neutron was tagged in the ZDC. This agreement is shown by the lower (blue) curve of Fig. E.7. The systematic uncertainty estimates were derived identically to the Au+Au method, except the deuteron wave function was held constant.

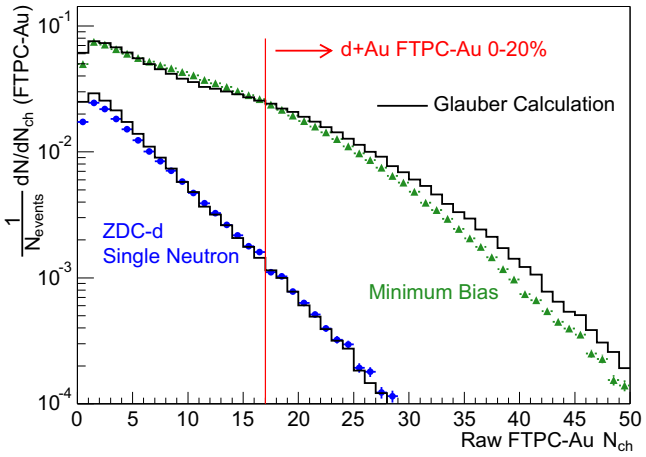

Figure E.7: Uncorrected charged particle multiplicity distributions measured in $-3.8 < \eta < -2.8$ (Au-direction) for d+Au collisions. Points are for minimum bias (triangles) and peripheral (circles, ZDC-d single neutron) collisions. Both are normalized to the total number of d+Au collisions. Histograms are Glauber model calculations.

Centrality(%)	$\langle N_{part} \rangle$	$\langle N_{coll} \rangle$	$\langle b \rangle$
0-5	$345.3^{+3.4}_{-3.5}$	$1024.6^{+72.5}_{-70.3}$	$2.3^{+-0.0}_{-0.1}$
5-10	$288.0^{+5.7}_{-5.9}$	$801.0^{+66.9}_{-62.9}$	$4.2^{+0.1}_{-0.2}$
10-20	$220.9^{+7.8}_{-8.0}$	$562.7^{+58.2}_{-57.5}$	$5.9^{+0.3}_{-0.3}$
20-30	$152.5^{+8.9}_{-9.4}$	$341.5^{+46.1}_{-46.1}$	$7.6^{+0.4}_{-0.4}$
30-40	$101.9^{+9.2}_{-9.7}$	$197.2^{+34.4}_{-34.9}$	$9.0^{+0.4}_{-0.4}$
40-50	$64.5^{+8.6}_{-8.9}$	$105.5^{+23.9}_{-24.7}$	$10.2^{+0.4}_{-0.5}$
50-60	$37.9^{+6.7}_{-7.3}$	$51.0^{+14.6}_{-15.9}$	$11.3^{+0.5}_{-0.7}$
60-70	$20.0^{+4.8}_{-5.6}$	$22.1^{+7.3}_{-9.1}$	$12.3^{+0.6}_{-0.7}$
70-80	$9.3^{+2.9}_{-3.5}$	$8.5^{+3.2}_{-4.2}$	$13.2^{+0.6}_{-0.7}$

Table E.2: Centrality, $\langle N_{part} \rangle$, $\langle N_{coll} \rangle$, and , $\langle b \rangle$ for Au+Au collisions at $\sqrt{s}$= 130 GeV from Optical Glauber. The systematic error estimates are described in detail in the text.

E.8 Summary of Glauber Calculation Results

We provide here a summary of results calculated in both the optical and Monte Carlo Glauber formalisms. The calculations were performed using a c++ software implementation written by the author that is now stored in the STAR offline computing repository.

Centrality(%)	$\langle N_{part} \rangle$	$\langle N_{coll} \rangle$	$\langle b \rangle$
0-5	$345.8^{+3.3}_{-3.4}$	$1049.3^{+73.7}_{-71.2}$	$2.3^{+0.1}_{-0.1}$
5-10	$288.7^{+5.7}_{-5.9}$	$819.7^{+68.2}_{-63.6}$	$4.2^{+0.2}_{-0.2}$
10-20	$221.6^{+8.1}_{-8.3}$	$575.3^{+59.4}_{-58.2}$	$5.9^{+0.3}_{-0.2}$
20-30	$153.0^{+9.2}_{-9.4}$	$348.8^{+47.1}_{-47.1}$	$7.6^{+0.4}_{-0.3}$
30-40	$102.3^{+9.3}_{-9.6}$	$201.2^{+35.3}_{-35.9}$	$9.0^{+0.4}_{-0.4}$
40-50	$64.8^{+8.6}_{-8.9}$	$107.6^{+24.1}_{-25.4}$	$10.2^{+0.4}_{-0.5}$
50-60	$37.9^{+6.9}_{-7.3}$	$52.0^{+14.5}_{-16.2}$	$11.3^{+0.4}_{-0.6}$
60-70	$20.0^{+4.9}_{-5.6}$	$22.4^{+7.5}_{-8.9}$	$12.3^{+0.5}_{-0.6}$
70-80	$9.3^{+2.9}_{-3.5}$	$8.5^{+3.4}_{-4.4}$	$13.2^{+0.6}_{-0.6}$

Table E.3: Centrality, $\langle N_{part} \rangle$, $\langle N_{coll} \rangle$, and , $\langle b \rangle$ for Au+Au collisions at $\sqrt{s}$= 200 GeV from Optical Glauber. The systematic error estimates are described in detail in the text.

Centrality(%)	$\langle N_{part} \rangle$	$\langle N_{coll} \rangle$	$\langle b \rangle$
0-100	$101.6^{+1.1}_{-1.7}$	$230.8^{+13.3}_{-15.7}$	$9.9^{+0.2}_{-0.5}$
0-10	$325.0^{+5.0}_{-4.9}$	$918.4^{+66.9}_{-68.4}$	$3.1^{+0.1}_{-0.1}$
0-5	$351.6^{+3.5}_{-3.4}$	$1027.2^{+69.0}_{-69.8}$	$2.2^{+0.2}_{-0.1}$
5-10	$298.3^{+6.3}_{-5.8}$	$809.2^{+65.4}_{-66.3}$	$4.1^{+0.2}_{-0.2}$
10-20	$233.5^{+7.7}_{-8.9}$	$578.1^{+52.7}_{-58.8}$	$5.8^{+0.2}_{-0.3}$
20-30	$166.2^{+9.2}_{-10.8}$	$360.5^{+41.3}_{-48.5}$	$7.5^{+0.3}_{-0.3}$
30-40	$114.9^{+8.6}_{-10.2}$	$215.9^{+31.0}_{-37.7}$	$8.8^{+0.4}_{-0.4}$
40-50	$76.2^{+8.1}_{-9.6}$	$121.0^{+22.3}_{-26.9}$	$10.0^{+0.4}_{-0.5}$
50-60	$47.3^{+7.0}_{-8.6}$	$62.5^{+13.2}_{-18.3}$	$11.1^{+0.5}_{-0.5}$
60-70	$26.9^{+5.1}_{-6.7}$	$29.1^{+8.2}_{-10.7}$	$12.0^{+0.6}_{-0.5}$
70-80	$14.1^{+3.6}_{-5.0}$	$12.3^{+4.4}_{-5.2}$	$12.9^{+0.6}_{-0.5}$
80-100	$4.5^{+1.1}_{-1.4}$	$3.1^{+0.9}_{-0.9}$	$14.3^{+0.6}_{-0.8}$
20-40	$140.3^{+8.5}_{-10.1}$	$288.1^{+36.7}_{-42.7}$	$8.1^{+0.3}_{-0.4}$
40-60	$61.4^{+7.3}_{-8.4}$	$91.8^{+17.7}_{-22.3}$	$10.5^{+0.5}_{-0.5}$
60-80	$20.5^{+4.6}_{-5.7}$	$20.9^{+6.2}_{-7.4}$	$12.4^{+0.7}_{-0.5}$
5-20	$255.0^{+7.1}_{-7.8}$	$654.8^{+57.6}_{-60.6}$	$5.2^{+0.2}_{-0.3}$
30-50	$95.8^{+8.8}_{-10.6}$	$168.2^{+26.6}_{-32.8}$	$9.4^{+0.4}_{-0.4}$
50-80	$29.7^{+5.8}_{-7.3}$	$34.7^{+8.7}_{-10.7}$	$12.0^{+0.6}_{-0.5}$

Table E.4: Centrality, $\langle N_{part} \rangle$, $\langle N_{coll} \rangle$, and , $\langle b \rangle$ for Au+Au collisions at $\sqrt{s}$= 130 GeV from Monte Carlo Glauber. The systematic error estimates are described in detail in the text.

Centrality(%)	$\langle N_{part} \rangle$	$\langle N_{coll} \rangle$	$\langle b \rangle$
0-100	$102.0^{+0.9}_{-1.7}$	$235.8^{+13.0}_{-16.0}$	$9.9^{+0.2}_{-0.5}$
0-10	$325.8^{+5.4}_{-5.3}$	$940.0^{+66.9}_{-69.5}$	$3.1^{+0.1}_{-0.1}$
0-5	$352.4^{+3.4}_{-4.0}$	$1051.3^{+71.5}_{-71.1}$	$2.2^{+0.2}_{-0.1}$
5-10	$299.3^{+6.6}_{-6.7}$	$827.9^{+63.8}_{-66.7}$	$4.1^{+0.2}_{-0.2}$
10-20	$234.6^{+8.3}_{-9.3}$	$591.3^{+51.9}_{-59.9}$	$5.8^{+0.2}_{-0.3}$
20-30	$166.7^{+9.0}_{-10.6}$	$368.6^{+41.1}_{-50.6}$	$7.5^{+0.3}_{-0.3}$
30-40	$115.5^{+8.7}_{-11.2}$	$220.2^{+30.0}_{-38.3}$	$8.8^{+0.4}_{-0.4}$
40-50	$76.6^{+8.5}_{-10.4}$	$123.4^{+22.7}_{-27.3}$	$10.0^{+0.4}_{-0.5}$
50-60	$47.8^{+7.6}_{-9.5}$	$63.9^{+14.1}_{-18.9}$	$11.1^{+0.6}_{-0.6}$
60-70	$27.4^{+5.4}_{-7.5}$	$29.5^{+8.2}_{-11.3}$	$12.0^{+0.7}_{-0.6}$
70-80	$14.1^{+3.6}_{-5.0}$	$12.3^{+4.4}_{-5.2}$	$12.9^{+0.7}_{-0.6}$
80-100	$4.5^{+1.1}_{-1.3}$	$3.1^{+1.0}_{-0.9}$	$14.3^{+0.6}_{-0.8}$
20-40	$141.4^{+9.1}_{-11.3}$	$294.2^{+34.8}_{-45.2}$	$8.1^{+0.3}_{-0.4}$
40-60	$62.4^{+8.3}_{-10.4}$	$93.6^{+17.5}_{-23.4}$	$10.5^{+0.6}_{-0.5}$
60-80	$20.9^{+5.1}_{-6.5}$	$21.2^{+6.6}_{-7.9}$	$12.4^{+0.8}_{-0.6}$
5-20	$256.1^{+7.1}_{-8.0}$	$669.8^{+56.5}_{-61.8}$	$5.2^{+0.2}_{-0.3}$
30-50	$95.8^{+8.6}_{-10.2}$	$171.9^{+26.7}_{-32.3}$	$9.4^{+0.4}_{-0.4}$
50-80	$29.7^{+5.8}_{-7.3}$	$35.3^{+9.2}_{-10.9}$	$12.0^{+0.6}_{-0.6}$

Table E.5: Centrality, $\langle N_{part} \rangle$, $\langle N_{coll} \rangle$, and , $\langle b \rangle$ for Au+Au collisions at $\sqrt{s}$= 200 GeV from Monte Carlo Glauber. The systematic error estimates are described in detail in the text.

Centrality(%)	$\langle N_{part} \rangle$	$\langle N_{coll} \rangle$	$\langle b \rangle$
0-20 Cut on N_{coll}	$16.3^{+1.1}_{-0.4}$	$16.5^{+0.4}_{-1.0}$	$2.5^{+0.2}_{-0.1}$
20-40 Cut on N_{coll}	$10.4^{+0.5}_{-0.0}$	$9.9^{+0.0}_{-1.0}$	$4.6^{+0.2}_{-0.2}$
40-100 Cut on N_{coll}	$4.3^{+0.0}_{-0.1}$	$3.2^{+0.0}_{-0.5}$	$7.3^{+0.2}_{-0.4}$
0-100 Cut on N_{coll}	$8.3^{+0.3}_{-0.4}$	$7.5^{+0.4}_{-0.4}$	$5.8^{+0.1}_{-0.3}$
$N^{deuteron}_{part} == 2$	$11.0^{+0.4}_{-0.5}$	$10.3^{+0.5}_{-0.5}$	$4.6^{+0.1}_{-0.1}$
$N^{deuteron}_{npart} == 1$	$3.9^{+0.1}_{-0.2}$	$2.9^{+0.1}_{-0.2}$	$7.6^{+0.2}_{-0.2}$
0-20 Cut on FTPCE	NA	$15.0^{+1.1}_{-1.1}$	NA
20-40 Cut on FTPCE	NA	$10.2^{+1.0}_{-0.8}$	NA
40-100 Cut on FTPCE	NA	$4.0^{+0.3}_{-0.3}$	NA
0-100 Cut on FTPCE	NA	$7.5^{+0.4}_{-0.4}$	NA

Table E.6: Centrality, $\langle N_{part} \rangle$, $\langle N_{coll} \rangle$, and , $\langle b \rangle$ for d+Au collisions at $\sqrt{s}$= 200 GeV from Monte Carlo Glauber. The systematic error estimates are described in detail in the text.

Appendix F

Acronyms

ADC Analog to Digital Conversion. ADC values represent the relative size of a TPC pixel.

AGS Alternating Gradient Synchrotron.

ALEPH ALEPH experiment at CERN. ALEPH was one of the large detectors at the LEP.

BBC Beam Beam Counter. The BBCs are scinitillating tiles used to trigger on charged particle multiplicity in the forward rapidity region.

BDMPS Baier, Dokshitzer, Mueller, Peigné, and Schiff. Responsible for a significant class of calculations of energy loss and $p_\perp$ broadening of partons traversing dense QCD matter.

BEMC Barrel Electromagnetic Calorimeter. The BEMC provides electromagnetic calorimetry in the mid-rapidity region.

BKK Binnewies, Kniehl, and Kramer. Publish a standard set of fragmentation functions extracted from e^+e^- data.

BNL Brookhaven National Laboratory.

BRAHMS Broad Range Hadron Magnetic Spectrometers Experiment at RHIC.

CDF Collider Detector at Fermilab.

CERN l'Organisation Européenne pour la Recherche Nucléaire.

CGC Color Glass Condensate. The CGC, also known as the saturation model, is a semi-classical application of QCD.

CIS Collinear and Infrared Safe.

CPU Central Processing Unit.

CTB Central Trigger Barrel. The CTB is made of scintillating tiles and is used to trigger on charged particle multiplicity.

CTEQ Coordinated Theoretical-Experimental Project on QCD.

DAQ Data Aquisition System.

DCA Distance of closest approach. DCA is most commonly calculated between two helices, a helix and the beam line, or a helix and a point.

DGLAP Dokshitzer, Gribov, Landau, Alterelli, and Parisi. Primarily responsible for initial development of the QCD evolution equations.

DIS Deep Inelastic Scattering.

EEMC Endcap Electromagnetic Calorimeter. The EEMC provides electromagnetic calorimetry in the forward-rapidity region.

EOS Equation Of State.

EVR Default STAR Vertex Finder. EVR is used for heavy ion collisions with charged particle multiplicities greater than $\sim$20.

FF Fragmentation Function.

FPD Forward Pion Detector. The FPD is a prototype for the endcap electromagnetic calorimeter.

FTPC Forward Time Projection Chamber. The FTPC provides charged particle tracking in the forward and backward rapidity regions.

GEANT GEometry ANd Tracking.

GLV Gyulassy, Vitev, and Levai.

HERA Hadron Electron Ring Accelerator.

HERMES HERa MEasurement of Spin.

IFC STAR TPC Inner Field Cage.

IR Infrared.

LCP Leading Charged Particle. The highest $p_\perp$ charged particle in a jet.

LEP Large Electron Positron Collider. LEP ran for over twenty years and was home to many major discoveries, including the W and Z bosons.

LMV Low Multiplicity Vertex Finder. LMV is used for primary vertex finding in extremely low multiplicity collisions.

LO Leading Order.

LPM Landau, Pomeranchuk, and Migdal. Initially responsible for inclusion of Quantum Mechanical effects in the consideration of electrically charged particles traversing dense matter.

MWPC Multi Wire Proportional Counter. The MWPC is part of the TPC readout system.

NA49 North Area 49^{th} Heavy Ion Experiment at CERN.

NLO Next to Leading Order.

NNLO Next to Next to Leading Order.

OFC STAR TPC Outer Field Cage.

PDF Parton Distribution Function.

PHENIX Pioneering High Energy Nuclear Experiment.

PHOBOS The original experiment MARS (Modular Array for RHIC Spectroscopy) was not approved. A similar setup under the name of one of the moons of Mars was later approved.

PMT Photo Multiplier Tube.

ppLMV Proton-Proton Low Multiplicity Vertex Finder. ppLMV is used for vertex finding in p+p collisions.

pQCD Perturbative Quantum Chromodynamics. pQCD is a perturbative field theory solution to QCD.

QCD Quantum Chromodynamics. QCD is the theory of strongly interacting particles.

QED Quantum Electrodynamics.

QGP Quark Gluon Plasma. The minimal definition of a QGP is a deconfined medium where color charges flow freely.

RGE Renormalization Group Equations.

RHIC Relativistic Heavy Ion Collider.

RHI Relativistic Heavy Ion.

RMS Root Mean Square.

SLAC Stanford Linear Accelerator Complex.

SM Standard Model.

SSD Silicon Strip Detector.

STAR Solenoidal Tracker at RHIC.

SVT Silicon Vertex Tracker. The SVT provides high precision tracking information close to the interaction point.

TCL Time Projection Chamber Cluster Finder. TCL is the software package used for cluster finding in the TPC.

TPC Time Projection Chamber. The TPC is STAR's main tracking detector.

TPT Time Projection Chamber Tracker. TPT is the current track finding software package for the STAR TPC.

TRS Time Projection Chamber Response Simulator. TRS is the software package that simulates the full detector response to charged particles.

WLSF Wavelength Shifting Optical Fibers.

ZDC Zero Degree Calorimeter. A ZDC primarily detects neutrons that are remnants of the beam break up.

Bibliography

[1] Robert L. Jaffe and Frank Wilczek. Diquarks and exotic spectroscopy. 2003. hep-ph/0307341.

[2] E. V. Shuryak and G. E. Brown. Matter-induced modification of resonances at RHIC freezeout. *Nucl. Phys.*, A717:322–335, 2003.

[3] Dmitri E. Kharzeev, Robert D. Pisarski, and Michel H. G. Tytgat. Aspects of parity, CP, and time reversal violation in hot QCD. 2000. hep-ph/0012012.

[4] Raymond Brock et al. Handbook of perturbative QCD: Version 1.0. *Rev. Mod. Phys.*, 67:157–248, 1995.

[5] F. Abe et al. *Phys. Rev. Lett.*, 61:1819, 1988.

[6] Frithjof Karsch. Lattice results on QCD thermodynamics. *Nucl. Phys.*, A698:199–208, 2002.

[7] Yuri L. Dokshitzer. QCD phenomenology. 2003. hep-ph/0306287.

[8] Daniel Magestro. Evidence for chemical equilibration at RHIC. *J. Phys.*, G28:1745–1752, 2002.

[9] Siegfried Bethke. Alpha(s) 2002. 2002. hep-ex/0211012.

[10] J. Pumplin et al. New generation of parton distributions with uncertainties from global QCD analysis. *JHEP*, 07:012, 2002.

[11] Vogt Gluck, Reya. *Z. Phys.*, C67:433, 1995.

[12] S. Kretzer. Fragmentation functions from flavour-inclusive and flavour- tagged e^+ e^- annihilations. *Phys. Rev.*, D62:054001, 2000.

[13] George Sterman. Mass divergences in annihilation processes. Origin and nature of divergences in cut vacuum polarization diagrams. *Phys. Rev.*, D17:2773, 1978.

[14] J. D. Bjorken. Energy loss of energetic partons in quark - gluon plasma: Possible extinction of high $p_\perp$ jets in hadron - hadron collisions. FERMILAB-PUB-82-059-THY.

[15] Miklos Gyulassy, Ivan Vitev, Xin-Nian Wang, and Ben-Wei Zhang. Jet quenching and radiative energy loss in dense nuclear matter. 2003. nucl-th/0302077.

[16] David d'Enterria. Hard scattering at RHIC: Experimental review. 2003. nucl-ex/0309015.

[17] R. Baier, Yuri L. Dokshitzer, Alfred H. Mueller, S. Peigne, and D. Schiff. Radiative energy loss of high energy quarks and gluons in a finite-volume quark-gluon plasma. *Nucl. Phys.*, B483:291–320, 1997.

[18] R. Baier, Yuri L. Dokshitzer, Alfred H. Mueller, and D. Schiff. Quenching of hadron spectra in media. *JHEP*, 09:033, 2001.

[19] Ivan Vitev. Multiparton tomography of hot and cold nuclear matter. 2003. nucl-th/0308028.

[20] Xin-Nian Wang. Why the observed jet quenching at RHIC is due to parton energy loss. 2003. nucl-th/0307036.

[21] Tetsufumi Hirano and Yasushi Nara. Back-to-back correlations of high $p_\perp$ hadrons in relativistic heavy ion collisions. *Phys. Rev. Lett.*, 91:082301, 2003.

[22] Miklos Gyulassy, Ivan Vitev, Xin-Nian Wang, and Pasi Huovinen. Transverse expansion and high $p_\perp$ azimuthal asymmetry at RHIC. *Phys. Lett.*, B526:301–308, 2002.

[23] S. S. Adler et al. Suppressed π^0 production at large transverse momentum in central Au + Au collisions at $\sqrt{s_{NN}}$= 200-Gev. *Phys. Rev. Lett.*, 91:072301, 2003.

[24] C. Adler et al. Elliptic flow from two- and four-particle correlations in Au + Au collisions at $\sqrt{s_{NN}}$ =130-GeV. *Phys. Rev.*, C66:034904, 2002.

[25] J. Adams et al. Evidence from d+Au measurements for final-state suppression of high $p_\perp$ hadrons in Au+Au collisions at RHIC. *Phys. Rev. Lett.*, 91:072304, 2003.

[26] Dmitri Kharzeev, Eugene Levin, and Larry McLerran. Parton saturation and N_{part} scaling of semi-hard processes in QCD. *Phys. Lett.*, B561:93–101, 2003.

[27] Alberto Accardi. Cronin effect in proton nucleus collisions: A survey of theoretical models. 2002. hep-ph/0212148.

[28] T. Ludlam. Overview of experiments and detectors at RHIC. *Nucl. Inst. Meth.*, A(499):428–432, 2003.

[29] F.S. Bieser et al. The STAR trigger. *Nucl. Inst. Meth.*, A(499):766–777, 2003.

[30] F. Bergsma et al. The STAR detector magnet subsystem. *Nucl. Inst. Meth.*, A(499):633–639, 2003.

[31] W. Blum and L. Rolandi. *Particle Detection with Drift Chambers*. Springer-Verlag, Germany, 1993.

[32] M. Anderson et al. The STAR time projection chamber: a unique tool for studying high multiplicity events at RHIC. *Nucl. Inst. Meth.*, A(499):659–678, 2003.

[33] M. Anderson et al. A readout system for the STAR time projection chamber. *Nucl. Inst. Meth.*, A(499):679–691, 2003.

[34] S. F. Biagai. MAGBOLTZ, a computer program. *Nucl. Inst. Meth.*, A(421):234, 1999.

[35] M.A. Lisa. Technical report, STAR Note 0238, 1996.

[36] R. Bossingham et al. Technical report, STAR Note 281, STAR Offline Simulations and Analysis Software Design, 1997.

[37] Brian Lasiuk and Thomas Ullrich. Star c++ class library: User guide and reference manual. Technical report, 1999.

[38] R. Brun, R. Hagelberg, M. Hansroul, and J. C. Lassalle. Technical Report CERN-DD-78-2-REV, CERN.

[39] J.E. Seger. PhD thesis, University of Wisconsin, Madison, 1991.

[40] Manuel Calderon de la Barca Sanchez. *Charged hadron spectra in* $\mathrm{A}u$ + $\mathrm{A}u$ *collisions at* $\sqrt{s}$*=130-*$\mathrm{G}e\mathrm{V}$. PhD thesis, Yale University, New Haven, CT, 2001.

[41] Gerald C. Blazey et al. Run II jet physics. 2000. hep-ex/0005012.

[42] Stephen D. Ellis and Davison E. Soper. Successive combination jet algorithm for hadron collisions. *Phys. Rev.*, D48:3160–3166, 1993.

[43] S. D. Ellis, J. Huston, and M. Tonnesmann. On building better cone jet algorithms. *eConf*, C010630:P513, 2001.

[44] George Sterman and Steven Weinberg. Jets from quantum chromodynamics. *Phys. Rev. Lett.*, 39:1436, 1977.

[45] Jonathan Gans. *Charged hadron spectra in p+p and d +* $\mathrm{A}u$ *collisions at* $\sqrt{s}$*=200-*$\mathrm{G}e\mathrm{V}$. PhD thesis, Yale University, New Haven, CT, 2004.

[46] T. Affolder et al. Charged jet evolution and the underlying event in proton anti-proton collisions at 1.8-Tev. *Phys. Rev.*, D65:092002, 2002.

[47] K. Hagiwara et al. Review of particle physics. *Phys. Rev.*, D66:010001, 2002.

[48] G. Boca et al. Average fraction of jet momentum carried by high-$p_\perp$ leading hadrons. *Z. Phys.*, C49:543–554, 1991.

[49] G. Arnison et al. First observation of correlations between high transverse momentum charged particles in events from the CERN proton anti-proton collider. *Phys. Lett.*, B118:173–177, 1982.

[50] P. Abreu et al. Observation of charge-ordering in particle production in hadronic Z^0 decay. *Phys. Lett.*, B407:174–184, 1997.

[51] C. Adler et al. Azimuthal anisotropy and correlations in the hard scattering regime at RHIC. *Phys. Rev. Lett.*, 90:032301, 2003.

[52] C. Friberg L. Lönnblad G. Miu S. Mrenna T. Sjöstrand, P. Edén and E. Norrbin. The Lund string fragmentation model. *Comp. Phys. Commun.*, 135:238, 2001.

[53] Francois Arleo. Constraints on quark energy loss from Drell-Yan data. *Phys. Lett.*, B532:231–239, 2002.

[54] Enke Wang and Xin-Nian Wang. Jet tomography of dense nuclear matter. *Phys. Rev. Lett.*, 89:162301, 2002.

[55] Ivan Vitev. Initial state parton broadening and energy loss probed in d + Au at RHIC. *Phys. Lett.*, B562:36–44, 2003.

[56] S. S. Adler et al. Absence of suppression in particle production at large transverse momentum in $\sqrt{s_{NN}}$ = 200-GeV d + Au collisions. *Phys. Rev. Lett.*, 91:072303, 2003.

[57] B. B. Back et al. Centrality dependence of charged hadron transverse momentum spectra in d + Au collisions at $\sqrt{s_{NN}}$ = 200-GeV. *Phys. Rev. Lett.*, 91:072302, 2003.

[58] I. Arsene et al. Transverse momentum spectra in Au + Au and d + Au collisions at $\sqrt{s_{NN}}$ = 200-GeV and the pseudorapidity dependence of high $p_\perp$ suppression. *Phys. Rev. Lett.*, 91:072305, 2003.

[59] K. Gallmeister, C. Greiner, and Z. Xu. Quenching of high $p_\perp$ hadron spectra by hadronic interactions in heavy ion collisions at RHIC. *Phys. Rev.*, C67:044905, 2003.

[60] Yuri L. Dokshitzer, Valery A. Khoze, Alfred H. Mueller, and S. I. Troian. Basics of perturbative QCD. Gif-sur-Yvette, France: Ed. Frontieres (1991) 274 p. (Basics of).

[61] Miklos Gyulassy, Peter Levai, and Ivan Vitev. Jet quenching in thin quark-gluon plasmas. I: Formalism. *Nucl. Phys.*, B571:197–233, 2000.

[62] M. Gyulassy, P. Levai, and I. Vitev. Non-abelian energy loss at finite opacity. *Phys. Rev. Lett.*, 85:5535–5538, 2000.

[63] M. Gyulassy, P. Levai, and I. Vitev. Reaction operator approach to non-abelian energy loss. *Nucl. Phys.*, B594:371–419, 2001.

[64] R. Baier, Yuri L. Dokshitzer, Alfred H. Mueller, and D. Schiff. Radiative energy loss of high energy partons traversing an expanding QCD plasma. *Phys. Rev.*, C58:1706–1713, 1998.

[65] R. Baier, D. Schiff, and B. G. Zakharov. Energy loss in perturbative QCD. *Ann. Rev. Nucl. Part. Sci.*, 50:37–69, 2000.

[66] Xin-Nian Wang. Probing initial parton density and formation time via jet quenching. *Nucl. Phys.*, A715:775–778, 2003.

[67] J D Bjorken. Highly relativistic nucleus-nucleus collisions: The central rapidity region. 27:140, 1983.

[68] Jian-wei Qiu and Ivan Vitev. Transverse momentum diffusion and broadening of the back- to-back di-hadron correlation function. *Phys. Lett.*, B570:161–170, 2003.

[69] G. Agakichiev et al. Semi-hard scattering unraveled from collective dynamics by two-pion correlations in 158-A-GeV/c Pb + Au collisions. 2003. nucl-ex/0303014.

[70] Xin-Nian Wang. High $p_\perp$ hadron spectra, azimuthal anisotropy and back-to-back correlations in high-energy heavy-ion collisions. 2003. nucl-th/0305010.

[71] Alan D. Martin, R. G. Roberts, W. James Stirling, and R. S. Thorne. Parton distributions: A new global analysis. *Eur. Phys. J.*, C4:463–496, 1998.

[72] K. J. Eskola, V. J. Kolhinen, and C. A. Salgado. The scale dependent nuclear effects in parton distributions for practical applications. *Eur. Phys. J.*, C9:61–68, 1999.

[73] Shi-yuan Li and Xin-Nian Wang. Gluon shadowing and hadron production at RHIC. *Phys. Lett.*, B527:85–91, 2002.

[74] J. Binnewies, Bernd A. Kniehl, and G. Kramer. *Z. Phys.*, C65:471, 1995.

[75] K. Adcox et al. Suppression of hadrons with large transverse momentum in central Au + Au collisions at $\sqrt{s_{NN}}$ =130-GeV. *Phys. Rev. Lett.*, 88:022301, 2002.

[76] C. Adler et al. Centrality dependence of high $p_\perp$ hadron suppression in Au + Au collisions at $\sqrt{s_{NN}}$ = 130- GeV. *Phys. Rev. Lett.*, 89:202301, 2002.

[77] J. Adams et al. Transverse momentum and collision energy dependence of high $p_\perp$ hadron suppression in Au + Au collisions at ultrarelativistic energies. *Phys. Rev. Lett.*, 91:172302, 2003.

[78] A. Airapetian et al. Hadron formation in deep-inelastic positron scattering in a nuclear environment. *Eur. Phys. J.*, C20:479–486, 2001.

[79] Valeria Muccifora. Hadron formation in DIS in a nuclear environment. *Nucl. Phys.*, A715:506–509, 2003.

[80] T. Falter, W. Cassing, K. Gallmeister, and U. Mosel. Hadron formation and attenuation in deep inelastic lepton scattering off nuclei. 2003. nucl-th/0303011.

[81] C. Adler et al. Disappearance of back-to-back high $p_\perp$ hadron correlations in central Au + Au collisions at $\sqrt{s_{NN}}$ = 200-GeV. *Phys. Rev. Lett.*, 90:082302, 2003.

[82] L. D. Landau and I. Ya. Pomeranchuk. *Dokl.. Akad. Nauk SSSR*, 92:535, 735, 1953.

[83] A. B. Midgal. *Phys. Rev.*, 103:1811, 1956.

[84] P. L. Anthony et al. An accurate measurement of the Landau-Pomeranchuk-Migdal effect. *Phys. Rev. Lett.*, 345:1949, 1995.

[85] P. L. Anthony et al. Bremsstrahlung suppression due to the LPM and dielectric effects in a variety of materials. *Phys. Rev.*, D56:1373–1390, 1997.

[86] Dmitri Kharzeev and Marzia Nardi. Hadron production in nuclear collisions at RHIC and high density QCD. *Phys. Lett.*, B507:121–128, 2001.

[87] Nick Dorey, Timothy J. Hollowood, S. Prem Kumar, and Annamaria Sinkovics. Exact superpotentials from matrix models. *JHEP*, 11:039, 2002.

[88] Jurgen Schaffner-Bielich, Dmitri Kharzeev, Larry D. McLerran, and Raju Venugopalan. Generalized scaling of the transverse mass spectrum at the Relativistic Heavy-Ion Collider. *Nucl. Phys.*, A705:494–507, 2002.

[89] Cheuk-Yin Wong. *Introduction to High-Energy Heavy-Ion Collisions*. World Scientific, Singapore, 1994.

[90] A J Baltz, C. Chasman, and S N White. Correlated forward-backward dissociation and neutron spectra as a luminosity monitor in heavy ion colliders. *Nucl. Instr. Meth. A*, 417:1, 1998.

[91] K. Adcox et al. Centrality dependence of the high $p_\perp$ charged hadron suppression in Au + Au collisions at $\sqrt{s_{NN}}$ = 130- GeV. *Phys. Lett.*, B561:82–92, 2003.

[92] I. G. Bearden et al. Charged particle densities from Au + Au collisions at $\sqrt{s_{NN}}$ = 130- GeV. *Phys. Lett.*, B523:227–233, 2001.

[93] B. B. Back et al. Charged hadron transverse momentum distributions in Au + Au collisions at $\sqrt{s_{NN}}$ = 200- GeV. 2003. nucl-ex/0302015.

[94] B. B. Back et al. Comparison of the total charged-particle multiplicity in high-energy heavy ion collisions with e^++e^- and p+p / p+$\bar{p}$ data. 2003. nucl-ex/0301017.

[95] B. B. Back et al. Centrality dependence of charged particle multiplicity at mid-rapidity in Au + Au collisions at $\sqrt{s_{NN}}$ = 130- GeV. *Phys. Rev.*, C65:031901, 2002.

[96] X N Wang and M. Gyulassy. Hijing: A Monte Carlo model for multiple jet production in p+p, p+A and A+A collisions. 44:3501, 1991.

[97] Dmitri Kharzeev, Eugene Levin, and Marzia Nardi. QCD saturation and deuteron nucleus collisions. 2002. hep-ph/0212316.